
# DEVELOPMENT OF FLEXIBLE GAS SENSORS BASED ON ADDITIVE FABRICATION PROCESSES

**Miriam Alvarado Pérez**

DOCTORAL THESIS

# "Development of Flexible Gas Sensors Based on Additive Fabrication Processes"

**Miriam Alvarado Pérez**

Supervised by:

**Prof. José Luis Ramírez Falo**

**Prof. Alfonso José Romero Nevado**

UNIVERSITAT ROVIRA i VIRGILI

Tarragona

2020

UNIVERSITAT ROVIRA I VIRGILI
DEVELOPMENT OF FLEXIBLE GAS SENSORS BASED ON ADDITIVE FABRICATION PROCESSES
Miriam Alvarado Pérez

UNIVERSITAT ROVIRA i VIRGILI

FEM CONSTAR que aquest treball, titulat "Development of Flexible Gas Sensors Based on Additive Fabrication Processes", que presenta Miriam Alvarado Pérez per a l'obtenció del títol de Doctor, ha estat realitzat sota la nostra direcció al Departament d'Enginyeria Electrònica Elèctrica i Automàtica d'aquesta universitat.

---

HACEMOS CONSTAR que el presente trabajo, titulado "Development of Flexible Gas Sensors Based on Additive Fabrication Processes", que presenta Miriam Alvarado Pérez para la obtención del título de Doctor, ha sido realizado bajo nuestra dirección en el Departamento de Ingeniería Electrónica Eléctrica y Automática de esta universidad.

---

WE STATE that the present study, entitled "Development of Flexible Gas Sensors Based on Additive Fabrication Processes", presented by Miriam Alvarado Pérez. for the award of the degree of Doctor, has been carried out under our supervision at the Department of Electronic, Electrical and Automation Control Engineering of this university.

---

Tarragona, 24 de Gener de 2020

El/s director/s de la tesi doctoral
El/los director/es de la tesis doctoral
Doctoral Thesis Supervisor/s

José Luis Ramírez Falo

Alfonso José Romero Nevado

UNIVERSITAT ROVIRA I VIRGILI
DEVELOPMENT OF FLEXIBLE GAS SENSORS BASED ON ADDITIVE FABRICATION PROCESSES
Miriam Alvarado Pérez

# Acknowledgments

I would like to express my sincere gratitude and appreciation to my supervisors Prof. José Luis Ramírez and Prof. Alfonso Romero for giving me the opportunity to make my doctoral thesis under their guidance. I am deeply grateful for their immeasurable patience and support during the realization of this doctoral thesis. Thank you for your enormous efforts to strengthen my scientific skills.

I would also like to thank to the Universitat Rovira i Virgili for the financial backing to develop my PhD work.

Furthermore, I am grateful for the company, help, support, and teachings of the different research group members, especially to my friends and colleagues. I want to thank Juan, Eric, Ernesto, Tesfalem, Aanchal and without forgetting to Xavi, Pineda, and Raúl, thank you for your extensive collaboration in the technical issues. Be sure that I have more than one teaching from each of you. I would like to thank for the technical support to the Servei de Recursos Científics i Tècnics from Universitat Rovira i Virgili (Marianna, Mercé and Rita).

To my family, thank you for being a source of support, love, care, and motivation.

To Roberto for his support and infinite patience during these years. I could not have done it without you.

*"The road is digital, but loving is still analogic"*

*Hugo Shmale*

UNIVERSITAT ROVIRA I VIRGILI
DEVELOPMENT OF FLEXIBLE GAS SENSORS BASED ON ADDITIVE FABRICATION PROCESSES
Miriam Alvarado Pérez

UNIVERSITAT ROVIRA I VIRGILI
DEVELOPMENT OF FLEXIBLE GAS SENSORS BASED ON ADDITIVE FABRICATION PROCESSES
Miriam Alvarado Pérez

UNIVERSITAT ROVIRA I VIRGILI
DEVELOPMENT OF FLEXIBLE GAS SENSORS BASED ON ADDITIVE FABRICATION PROCESSES
Miriam Alvarado Pérez

# Table of Contents

# List of Figures

# List of Tables

UNIVERSITAT ROVIRA I VIRGILI
DEVELOPMENT OF FLEXIBLE GAS SENSORS BASED ON ADDITIVE FABRICATION PROCESSES
Miriam Alvarado Pérez

UNIVERSITAT ROVIRA I VIRGILI
DEVELOPMENT OF FLEXIBLE GAS SENSORS BASED ON ADDITIVE FABRICATION PROCESSES
Miriam Alvarado Pérez

# General Introduction

# General Introduction

The history of gas sensors begins in 1962, in Japan, when a propane gas explosion motivated Naoyoshi Taguchi to conduct research into gas leak detectors. Consequently in 1968, and invented by Taguchi, the first commercial gas sensor appeared in the market. The sensor could measure extremely low concentrations of inflammable and reducing gases. The sensor was used to detect gas leakage in homes and industries. The electrical resistance of the sensor changed in the presence of gases. It consisted of a ceramic substrate heated by a wire and coated by a metal oxide semiconducting film. The metal oxide semiconductor chosen by Taguchi was a tin oxide ($SnO_2$).

Taguchi's sensor triggered the research and development of gas sensors based on different metal oxides, such as zinc oxide (ZnO), titanium dioxide ($TiO_2$), iron (III) oxide ($Fe_2O_3$), indium oxide ($In_2O_3$), etc. The introduction of new sensitive materials broadened the type of gases to detect, and thus, the field of application of the gas sensors began to expand.

Since that time, gas sensors have been evolving according to the emergence of innovative technologies, from Taguchi's device to the use of microfabrication techniques (silicon-based devices), from the bulk metal oxide powder to modulating the size and shape of the metal oxide particles.

Nowadays, gas sensors help to monitor indoor and outdoor air quality in homes, schools, hospitals, the exhausts of industrial processes or vehicles, the level of harmful gases in the streets, etc. For example, in the chemical industry gas sensors can detect the leakage of flammable or toxic gases. In the food industry, gas sensors can help to detect spoilage and the quality of food. Also, scientists are investigating to diagnose diseases such as diabetes, asthma, cancer, and halitosis by analyzing the volatiles in the breath, sweat, saliva, and urine. The main objective of the development of gas sensors is to contribute to human well-being, as Taguchi envisaged.

To adapt the gas sensors to our daily-life activities, they should work in real-world conditions and be adaptable to organic contours. Then, mechanically flexible and resistant materials are needed. Paper or plastic foils are replacing

conventional sensor platforms. But the use of these flexible materials entails new developmental challenges, since flexible materials cannot withstand the elevated temperatures to obtain and modulate the morphology of metal oxides. Furthermore, mature fabrication techniques are conceived for rigid substrates, so it is needed to adapt them to flexible materials.

Among the mature fabrication techniques, Printed Electronics has been adapted to flexible supports. Printed Electronics deposits patterns using printing equipment and encompasses techniques such as screen printing, offset lithography, gravure, flexography, and inkjet printing [1].

The first attempts to fabricate electronic devices on flexible supports were focused on displays, solar cells, transistors, and LEDs. The successful fabrication of these devices garnered the attention of the researchers to broaden the scope of the flexible devices. The attractiveness of Printed Electronics for the development of flexible devices relies on their known low cost and fast production for large area devices. Furthermore, the futuristic concept of flexible electronics goes beyond to wearable electronics. Printed Electronics is a field that is making rapid strides, for instance, IDTechEx predicted that the market of printed, organic and flexible electronics will reach a value of 41.2 billion-dollars in 2020 and the market for fully printed sensors will reach a 7.6 billion-dollar revenue by 2027 [2,3].

Bearing in mind this trend, and the expertise of the investigation group to modify the morphology of metal oxides and characterize gas sensors, the present project conceives the design, fabrication, and characterization of flexible gas sensors based on metal oxides.

The goals of the current work were:

- To fabricate flexible gas sensors by printing techniques.
- To employ metal oxides as sensitive material.
- To reduce the number of fabrication steps, the material waste, and fabrication cost.
- To prove the flexibility and durability of the fabricated sensors.

The organization of this thesis is as follows:

- Chapter 1 introduces the basic concepts of gas sensors and their fabrication techniques. Additionally, it presents a summary of the current state of flexible gas sensors based on metal oxides.
- Chapter 2 presents the fabrication of sensors using a flexible substrate by combining printing techniques and drop coating.
- Chapter 3 details the fabrication of flexible sensors combining printing techniques and a direct growth method for the metal oxide.
- Chapter 4 shows the combination of inkjet printing and a direct growth method for the metal oxide.
- Chapter 5 details the fabrication of a fully screen-printed sensor.
- Chapter 6 presents the general conclusions and points future approaches for flexible gas sensor development.

# CHAPTER 1
# Introduction

# Introduction

## Basic Concepts of Chemoresistive Gas Sensors

Conductometric sensors (resistive or chemoresistive) are a type of gas sensor in which the output signal is expressed as a conductivity change. Metal oxides among other materials (conductive polymers, carbon materials, etc.) are used as gas-sensitive materials. Conductometric gas sensors include a substrate with electrodes over it, on which a sensitive layer is deposited. Additionally, they may have a heater.

### Gas Sensor Elements

- Substrate

The substrate is a piece of material, the base of the sensor, in which all the sensor elements are deposited.

- Electrodes

Electrodes are conductive lines that allow to measure the active layer conductance. Electrodes can be found either above or under the active layer.

- Active layer

The active layer is a layer of sensitive material which changes its conductivity according to the presence or absence of gas.

- Heater

The purpose of the heater is to increase the sensitive layer temperature. The sensor working temperatures are usually over room temperature.

Fig. 1.1 illustrates the construction of a sensor with all its elements.

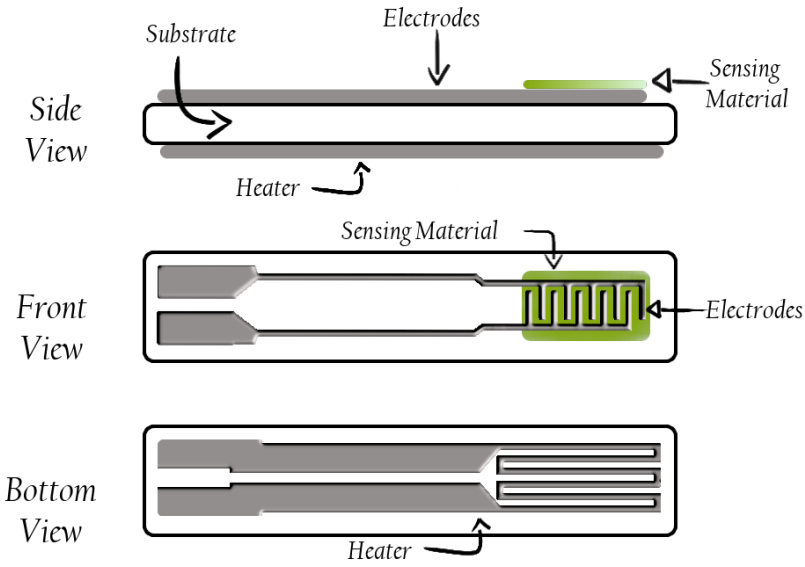


Fig. 1.1 Elements of conductometric gas sensors.

The output signal can be expressed using the conductance (G), electrical resistance (R), current intensity (I) or voltage (V). Also, the output signal can be expressed as a change of capacitance, work function, mass, optical characteristics, or reaction energy released by the gas-solid interaction [4].

## Materials for Gas Sensors

**Semiconductor Materials**

According to band theory, solid materials are classified in three main groups: conductors, insulators, and semiconductors. Compared to insulators, semiconductor materials have a narrower bandgap. With light energy increases, electrons reach the conduction band creating a hole in their place. This phenomenon is called carrier generation. Electrons are carriers with negative charge while holes have a positive charge.

Semiconductors' energy gap lies between zero and about 4 electron volts (eV) and can be classified in: elemental, binary, oxides, layered, and organic,

among others [5]. Depending on the carrier generation process, semiconductor behavior is classified into n-type or p-type.

- **n-type semiconductor**

In an n-type material, the majority carriers are free electrons. The material has more free electrons than holes. These materials are called n-type since electrons have a negative charge.

- **p-type semiconductor**

In a p-type material, the majority carriers are holes. It is called p-type since holes have a positive charge.

**Metal Oxide Semiconductors**

Metal oxide (MOX) semiconductors are the most common materials for gas sensors. MOX are being employed as active layers, substrates, structure modifiers and so on [6]. Metal oxides such as $SnO_2$, $TiO_2$, ZnO, CuO, $WO_3$, $In_2O_3$, $TeO_2$, CdO, $Fe_2O_3$ and $MoO_3$ have been used as active layer to fabricate chemoresistive gas sensors [7].

Gas sensors employing oxide semiconductors can work as both a recognition system and a transducer. The transducers are available in the form of resistors, diodes, capacitors, transistors, etc. [8].

***Conductive Materials***

To obtain the conductive lines that form the electrodes or heater, the conductive materials deposited over the substrate must be mechanically and chemically inert [9].

Most suitable materials are noble metals. Although platinum and gold are the most used materials for electrode fabrication also metals such as silver and palladium have been employed [10].

The heaters are obtained by the deposition of metal or metal/alloy. The materials used must have long term stability. Platinum-based materials are the most widespread materials employed for heater fabrication thanks to its stability and corrosion resistance [11].

***Substrates***

Non-rigid materials such as polymer films, metal foil, thin glass, paper, and fabric can be used as flexible substrates [12–15].

The brittleness of thin glass and the excessive cost of metal foils are some of the obstacles to use these materials for flexible applications [12]. Characteristics like light weight, low-cost, high flexibility, mechanical strength and the possibility of large-scale production, have made polymers the most used materials for flexible electronics development.

Thermoplastic polymers are polymers that can be deformed many times on heating and maintain the new shape when cooling [16]. Thermoplastics are classified by the order of their molecular structures in amorphous and semi-crystalline. In amorphous thermoplastics the polymer chains exist in random positions and orientations. A thermoplastic is crystalline when the chains presents a repeated and ordered structure. Semi-crystalline thermoplastics are partly crystalline and partly amorphous [17]. Thermoplastics can be deformed, become flow-able or moldable when they are heated above either their glass transition temperature ($T_g$) for amorphous or above their melt temperatures ($T_m$) for semi-crystalline [16]. These temperatures serve as a guide to define the maximum temperature to which process the material. Moreover, it is good to note that the deformation of the thermoplastics implies a shrinkage and expansion. The shrinkage occurs when the material is heated and then cooled to the starting temperature. The expansion occurs when the material is subjected to cyclic temperature treatments [18]. The shrinkage is expressed in % of change of dimension, while the expansion by the coefficient of thermal expansion (CLTE). Because the extent of expansion of the thermoplastics is small, the CLTE is expressed as the fractional increase in length per unit rise in temperature, for instance $ppm \cdot °C^{-1}$. Therefore, the glass transition temperature or melting temperature, shrinkage, and CLTE are the basic properties to evaluate when choosing a material.

Polymers used in flexible electronics can be classified in [19,20]:

- Thermoplastic semi-crystalline:

  PET (polyethylene terephthalate), PEN (polyethylene naphthalate), and their respective heat-stabilized counterparts (HS-PET, HS-PEN).

- Thermoplastic and amorphous (non-crystalline):

  PC (polycarbonate) and PES (polyethersulphone).

- Amorphous, solvent cast and high $T_g$:

  PAR (polyarylates), PCO (polycyclic olefin), and PI (polyimide).

Table 1-1 presents the glass transition temperature and the coefficient of thermal expansion of materials commonly used to fabricate flexible electronic devices. It is worth to note that nowadays, it is possible to find a wide variety of polyester films with improved characteristics.

| | Thermoplastic Semi-crystalline | | Thermoplastic Amorphous | | Amorphous, solvent cast | |
|---|---|---|---|---|---|---|
| | PET | PEN | PC | PES | PCO | PI |
| Glass transition temperature (°C) | 80 | 150 | 145 | 223 | 164 | 300< |
| Coefficient of thermal expansion (ppm·°C$^{-1}$) | 33 | 20 | 75 | 54 | 70 | 8-20 |

Table 1-1 Properties of plastics substrates [21].

## Working Principle

The conductivity changes of the metal oxide due to interaction with gas molecules are the base of the operating principle of chemoresistive metal oxide gas sensors. Through the electrodes, it is possible to measure these conductivity changes.

In the air, oxygen adsorption on the surface of the n-type metal oxide creates a depletion layer. The oxygen adsorption produces an increase of the sensor resistance. If another gas is present, the gas will react with the pre-adsorbed oxygen or with the metal oxide, changing the depletion layer

thickness. The depletion layer thickness is known as Debye length $\lambda_D$ and its changes affect sensor conductivity.

At temperatures below 200 °C, oxygen adsorbed in the surface forms molecular species by trapping an electron from the conduction band of the active layer (Eq. 1-1)

$$\boldsymbol{O_2(gas) + e^- \Leftrightarrow O_2^-(adsorb)} \qquad \textit{Eq. 1-1}$$

At temperatures above 200 °C, the molecular species are dissociated into atomic species with single or double negative electric charges by trapping an electron from the conduction band of the active layer (Eq. 1-2 and 1-3).

$$\boldsymbol{\frac{1}{2}O_2 + e^- \overset{k_{Oxy}}{\Longleftrightarrow} O_{ads}^-} \qquad \textit{Eq. 1-2}$$

$$\boldsymbol{\frac{1}{2}O_2 + 2e^- \overset{k_{Oxy}}{\Longleftrightarrow} O_{ads}^{2-}} \qquad \textit{Eq. 1-3}$$

where $e^-$ are the electrons and $k_{Oxy}$ is the reaction rate constant [22].

In the presence of a reducing gas (R), such as $H_2$, CO or $CH_4$, the adsorbed oxygen reacts with the gases, reducing the thickness of the depletion layer by the injection of electrons to the active layer. Thus, the resistance decreases. The reaction is summarized as follows [23]:

$$\boldsymbol{R + MO - O^- \rightarrow MO + RO + e^-} \qquad \textit{Eq. 1-4}$$

In the presence of an oxidizing gas (O), electrons are extracted from the bulk region, the depletion layer becomes thicker and resistance increases.

$$\boldsymbol{MO - O^- + O + e^- \rightarrow MO - O_2^-} \qquad \textit{Eq. 1-5}$$

Sensor operation can be expressed using the energy band model: considering a granular material, when oxygen is absorbed and traps electrons from the active layer, the depletion layer appears, energy band is upward bending which means electrons need more energy to reach the surface. Two back-to-back Schottky barriers appear between the grains increasing the contact resistance among them. Fig. 1.2 represents the physical interaction of the oxygen with the surface material and the corresponding band model.

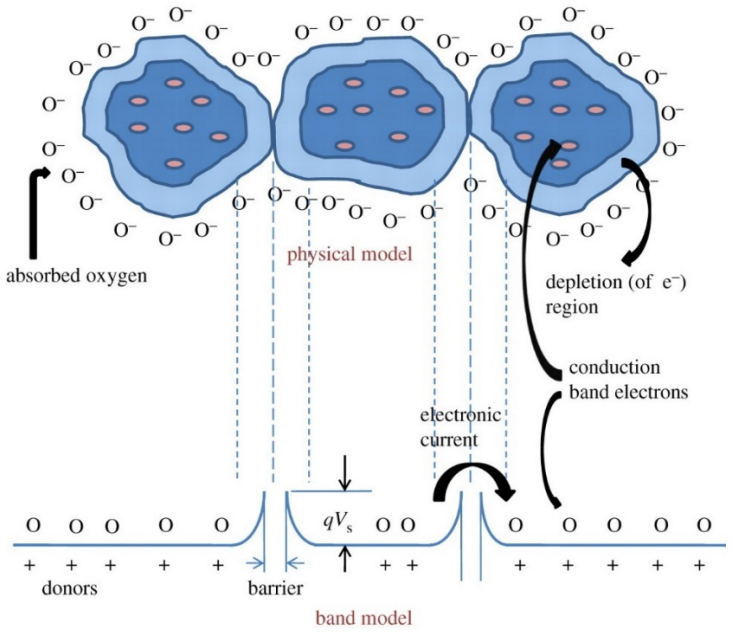


Fig. 1.2 Model of a back-to-back Schottky barrier in an intergranular metal oxide due to oxygen adsorption. Down: the energy band diagram [23].

Gas adsorption depends on the sensing layer morphology from which we can differentiate between compact and porous layers (Fig. 1.3). For an n-type material, in compact layers two zones appear, the bulk zone and the geometric surface (depletion layer). In the bulk zone there is no gas interaction however in the geometric surface there is. Therefore, the bulk zone has higher conductivity (lower resistivity) and dominates the conduction process. Most of compact layers are obtained using thin-film deposition. In porous layers, the surface area accessible to the gasses is higher than the geometric one. Conduction process is directly influenced by the depletion layer between the grains. Sensor resistivity increases because electrons need more energy to overpass the intergranular barriers. Most of these layers are obtained using thick-film deposition [24].

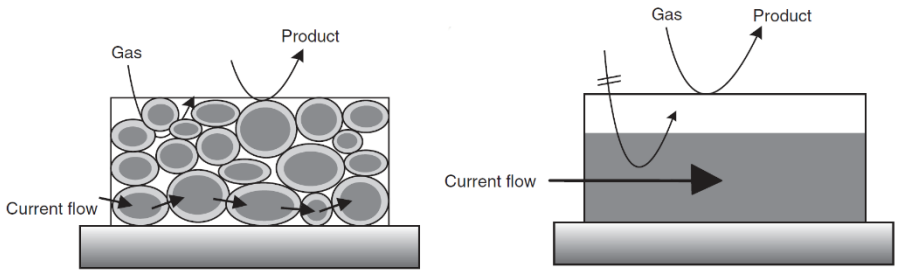


a) Porous layer b) Compact layer

Fig. 1.3 Morphology of a sensing layer [24].

In the case of porous layers, the extent of sintering of the active layer produces the formation of necks between the grains. Neck formation comes to change the conduction model previously explained. A model where the transducer function depends on the grain size (D) and the Debye length (L) was proposed in [25]. Assuming an active layer as a chain of crystallites, which are connected mostly by necks and sometimes by grain-boundary contacts. If the neck size (X) is 0.8 times the crystallite size and:

- D>>2L, grain boundary contacts govern the electric resistance and the gas sensitivity of the chain. This mechanism is called grain-boundary control.
- D ≥ 2L, necks become most resistance and control the gas sensitivity. This mechanism is called neck control.
- D < 2L, grains govern the electric resistance, control gas sensitivity and a larger sensor response is obtained. This mechanism is called grain control.

Figure 1.4 illustrates the effects of the grain size in the conduction of the porous layers.

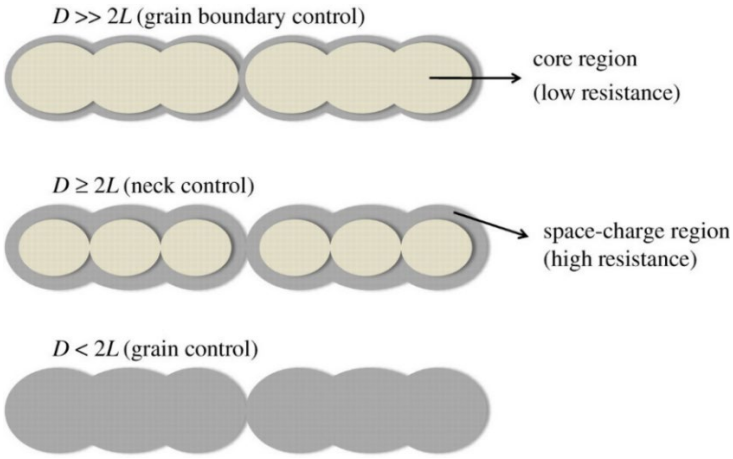


Fig. 1.4 Models for grain-size effects [23].

## Sensor Requirements and Characteristics

Although the conductivity changes of the chemoresistive sensors are the base of their operating principle, there are other important parameters when evaluating the behavior of a sensor.

The application requirements of the sensors rule the sensor characteristics to be considered for its design and manufacturing. Namely, the target gas, response and recovery time, signal noise, power consumption, size, cost, environmental conditions, among others. All these factors are described as the four S: suitability, sensitivity, selectivity, and stability [26].

Some of the parameters mentioned above are defined below.

**Sensor response**

Sensor response (S) is defined as the ratio in change of the sensor conductance. For clarity, all formula definitions will be expressed in function of the sensor resistance. For an n-type material sensing an oxidizing gas, the sensor response is defined as:

$$\boldsymbol{S = \frac{R_g}{R_a}}$$

where $R_a$ is the resistance of the gas sensor in air exposure and $R_g$ is the resistance in target gas exposure. Also, it is possible to express the percentage response as:

$$\boldsymbol{S(\%) = \frac{\Delta R}{R_a} \times 100\ \% = \frac{R_g - R_a}{R_a} \times 100\%}$$

**Sensitivity**

The sensitivity is the slope of the sensor response curve.

**Selectivity**

It is the ability of the sensor to discriminate one gas upon the presence of interfering gases.

**Stability**

It is the ability of the sensor to keep its performance constant throughout its lifetime.

**Response/recovery time**

For a sensor in steady-state and having a step change on the input: the response time, $\tau_{res}$, is the time the sensor resistance takes to reach 90% of its maximum change. The recovery time, $\tau_{rec}$, is the time the sensor resistance takes to recover 90% of its maximum change. The total change is the difference between the maximum change of the resistance and the resistance in steady state.

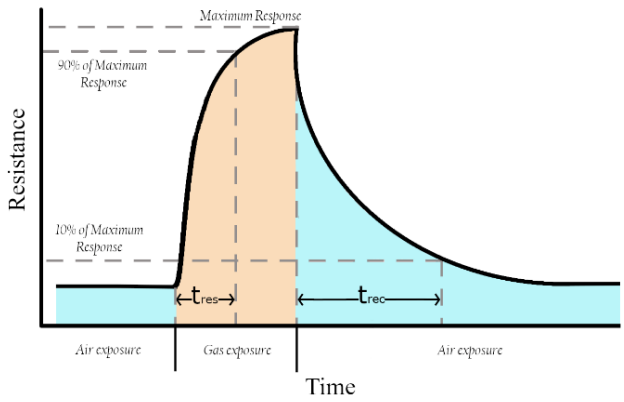


Fig. 1.5 Response and recovery time.

**Operating temperature**

The oxygen adsorption rate constant ($k_{Oxy}$) depends on the temperature, so the sensor response also depends on the temperature. The operating temperature is at which the sensor operation is effective, according to the application requirements.

## Gases to Detect

The wide range of potential applications for gas sensors is largely due to the different gases that can be detected and their detection volume. The selectivity and sensitivity requirements are different for each application. The most common gases to detect and their detection ranges according to their detection applications are described below.

Nitrogen dioxide ($NO_2$) is a reddish-brown toxic gas with a characteristic sharp, biting odor. Furthermore, the $NO_2$ is soluble in water and is a strong oxidant. The $NO_2$ is the product of the combustion of fossil fuels. The emission sources of $NO_2$ are vehicle exhausts, thermal power stations, pulp mills, butane heaters, gas stoves, among others. High environment concentrations of $NO_2$ have adverse effects on human health and could contribute in the global climate change. Also, $NO_2$ plays a role in determining the ozone ($O_3$) concentrations in the troposphere. The Environmental Directorate General of the European Commission establishes health-based standards for human exposure to $NO_2$: around 100 ppb for a one-hour exposure period and around 21 ppb over one year [27]. While the U.S. Environmental Protection Agency (EPA) establishes 100 ppb and 53 ppb for one hour exposure and one year exposure, respectively [28]. Therefore, the request is that the gas sensors be able to measure concentrations in the range of 0.01-3 ppm [29].

Hydrogen ($H_2$) is a colorless, odorless, and tasteless flammable gas. The main uses of hydrogen are in the chemical industry as a process supply or product and as a gaseous fuel to replace carbon-based fuels in aircraft, submarines, and vehicles. In its liquid form is used as power source for space-shuttles. The lower explosive limit for hydrogen in air is 40000 ppm (4%). The EPA fixed the 10% of the lower explosive limit, that is 4000 ppm, as safety factor [30]. When the gas concentration reaches the safety factor the EPA recommends the evacuation of the personnel. Therefore, in the case of gas

sensors needed to detect hydrogen leakage and concentration is necessary the sensors can indicate the concentration of hydrogen in the range of 100-100000 ppm (0.01-10%) for safety sensors or 10000-1000000 ppm (1-10%) for fuel cells [31].

Hydrogen sulfide ($H_2S$) is a flammable, colorless gas, soluble in various liquids including water, that smells like rotten eggs. The natural sources of $H_2S$ are volcanoes, sulfur springs, undersea vents, swamps, stagnant bodies of water, among others. The human activities that are source of $H_2S$ are sewage treatment plants, swine containment, manure-handling operations, pulp and paper operations, petroleum refineries, natural gas plants, food processing plants and tanneries. People can smell $H_2S$ at low concentrations, ranging from 0.005 to 0.3 ppm [32]. At higher concentrations, the smell can no longer be recognized, this can increase the risk to high concentration exposure bringing serious health effects. $H_2S$ air concentrations from natural sources are less than 0.00011-0.00033 ppm while in surface and waste waters the concentration is ranging around 1-5 ppm. The Occupational Safety and Health Administration (OSHA) of the U.S. set a ceiling limit of 20 ppm of exposure to $H_2S$ for a period of 15-minute during the working day. While the National Institute for Occupational Safety and Health (NIOSH) determined that 100 ppm of $H_2S$ exposure is immediately dangerous to life or health [32]. While the European Agency for Safety and Heath at Work establishes the occupational $H_2S$ exposure limit values of 5 ppm to 8-hours weighted average and 10 ppm for a 15-minute period [33].

Ammonia ($NH_3$) is a colorless, highly irritant gas with a characteristic pungent and suffocating odor. Ammonia is essential for many biological processes. It is part of the nitrogen cycle and is produced in the soil from bacterial processes. It is also produced from the decomposition of organic matter, including plants, animals, and animal wastes. Artificially, the ammonia emission is related with the agriculture, refrigeration systems, automotive, and chemical industries. Furthermore, ammonia is related to medical diagnosis. The human body also produces small quantities of ammonia, an unbalance of the ammonia production could indicate peptic ulcers and renal/liver diseases. The exposure at high concentrations of ammonia has toxic effects for human health. Because ammonia is present in a large variety of fields, it takes relevance to detect and measure the concentration of ammonia present in each field. Below the detection range of ammonia for some areas of application is described [34].

- To monitor environmental conditions is desirable a detection range of 0.1 ppb to 200 ppm.
- In cars, to measure ammonia emissions in a range of around 4-2000 g/min, to control the air quality of the passenger cabinet, detection of 50 ppm is necessary, and in the exhaust of diesel vehicles, it is necessary a range of detection of 1-100 ppm.
- In the chemical industry, it is needed a detection range of 20-1000 ppm.
- And in medical diagnosis, it is needed the sensor can measure concentrations in the range of 50-2000 ppb.

Ethanol ($C_2H_6O$) is a clear, colorless liquid with wine-like odor. It is the principal part of the alcoholic drinks and is considered as a psychoactive drug. It has medical applications as antiseptic and disinfectant. Also, the ethanol is used as a solvent and in making other chemicals. Monitoring the concentration of ethanol is important for safety. Drunk drivers can be detected by an alcohol breath test, because the concentration of ethanol present in the human breath is related to blood alcohol concentration. In the workplace, the exposure to high airborne concentrations can lead to nose, throat or lungs irritations. While repeated exposure may affect the liver and the nervous system. For instance, the U.S. government (OSHA and NIOSH) established a permissible exposure limit of 1000 ppm over a 10-hour work shift [35].

Acetylene ($C_2H_2$) is a colorless gas that is used for welding and cutting metals. Its combustion in oxygen produces a higher combustion temperature than that of any other hydrocarbon gas and at concentrations between 2.3-82% produces an explosive mixture in the air [36]. Easily ignites and burns. Under prolonged exposure to fire or heat the containers may rupture violently and rocket.

## Fabrication Methods

The elemental fabrication of MOX gas sensors consists of the integration of the MOX on the substrate. As mentioned above, the substrate could have electrodes and heater, and they can be deposited before or after the integration of the MOX on the substrate.

Two approaches are followed to integrate the MOX over the flexible substrate, either direct growth on the substrate or the transfer to the substrate after growth.

For instance, the techniques used as a direct growth method are Vapor-Liquid-Solid (VLS), Physical Vapor Deposition (PVD), Hydrothermal, Sol-Gel, among others. Instead, the techniques used for transferring the MOX are drop coating, spin coating, inkjet printing, screen printing, and transfer printing, among others.

## Direct Growth

### *Chemical Vapor Deposition (CVD)*

Using CVD, a heated substrate is exposed to a gaseous precursor or a mixture of gaseous precursors. The gases react or dissociate on or near the heated substrate depositing a film of the desired material. The main CVD parameters are deposition temperature, pressure, input gas ratio, and flow rate. The Fig. 1.6 illustrates the CVD process [37].

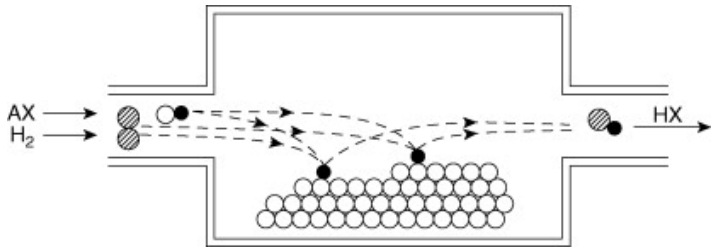


Fig. 1.6 The principle of chemical vapor deposition (CVD) [38]

There are different CVD routes based on different heating methods to cause the reaction, and the type of precursor used. Some variants of CVD techniques are atmospheric pressure CVD (APCVD), aerosol assisted CVD (AACVD), plasma-enhanced CVD (PECVD), thermally activated CVD, photo-assisted CVD, metalorganic CVD, among others.

***Physical Vapor Deposition***

PVD processes consist of a solid-vapor-solid transformation of the material to be deposited.

The target material in a solid-state is transformed into a gaseous state and then is condensed on the substrate in the form of a thin film. According to the process used to evaporate the solid, these techniques can be subdivided into evaporation, sputtering and ion plating processes.

***Sol-Gel***

In the sol-gel process, the solid particles are suspended in a colloidal solution. This solution can be deposited through spin-coating, dip-coating and by spray-coating. Then the solution can be converted into a gel. Then the film is dried and sintered obtaining a solid layer.

## Transfer

***Drop Coating***

Drop coating is a technique used for active layer deposition. As its name says, the material is deposited in drop form over the electrodes employing a micropipette. Then, the material is dried or annealed.

**Transfer Printing**

Transfer printing is the set of techniques used to deposit materials in 2D or 3D arrangements. This technique is based on using a molded stamp to deposit the materials over a substrate. The stamp is usually made of an elastomeric material. This technique is classified into additive, subtractive, and deterministic. In the additive approach, the ink is deposited on the stamp and then stamped on the receiver substrate. In the subtractive approach, the stamp removes parts of the substrate. The deterministic approach combines the additive and subtractive approaches. For example, structures can be prepared by additive transfer in substrate 1. Some structures are removed from substrate 1 and transferred to substrate 2.

### *Screen Printing*

In screen printing deposition the pattern to deposit is determined by the screen. The ink has the materials to obtain the electrodes or the active layer. To make the pattern, the screen is coated with an ultraviolet-sensitive emulsion upon which the pattern can be formed photographically. The screen is held in horizontal position, and the substrate is located under the screen (in horizontal position). The screen and the substrate are separated by a snap-off distance during the printing process. An amount of ink is placed in the screen surface near the pattern. Then ink is squeegeed and passes through the screen openings being transferred to the substrate. Finally, the pattern obtained is dried [13,39]. The quality of the obtained pattern is affected by ink viscosity, printing speed, snap-off distance, material and size of the mesh, hardness and geometry of the squeegee, and by the substrate. In Figure 1.7 screen printing process is depicted and the process variables that influence it are summarized [40].

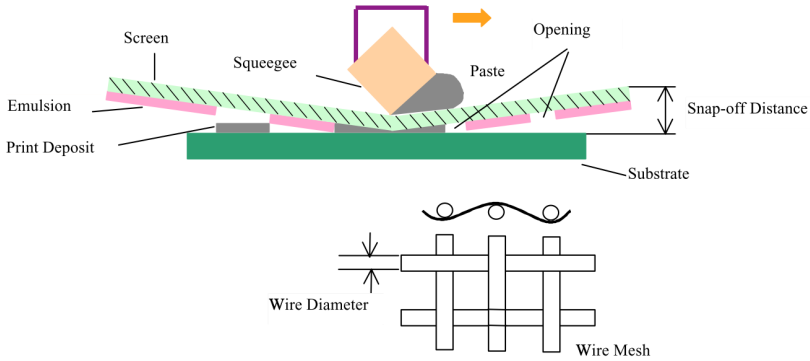


Fig. 1.7 Elements of the screen printing process [40].

### *Inkjet Printing*

Inkjet printing of materials resembles the home/office inkjet printers. In comparison with the drop coating technique, the inkjet printing allows accurate positioning of the drops and diminishes their volume. The equipment controls the jetting. At present, there are two different inkjet printing techniques for functional material deposition: continuous inkjet (CIJ) and drop on demand (DOD).

In Continuous inkjet systems (CIJ) the ink is in a pressurized reservoir under vibration. The reservoir pressure is increased to break up the fluid stream and generate a continuous and consistent stream of drops. The drops are deflected by electrostatic plates to the substrate or to a recirculation gutter [1,41].

In the Drop on Demand (DOD) inkjet, the head nozzles are placed vertically, above and close to the substrate. They eject a drop of ink when are activated. Through a pulse sent to the head nozzle, the pressure within the reservoir is increased and a drop is ejected. The pulse can be generated thermally or piezoelectrically [1]. Figure 1.8 illustrates the differences between each inkjet printing system.

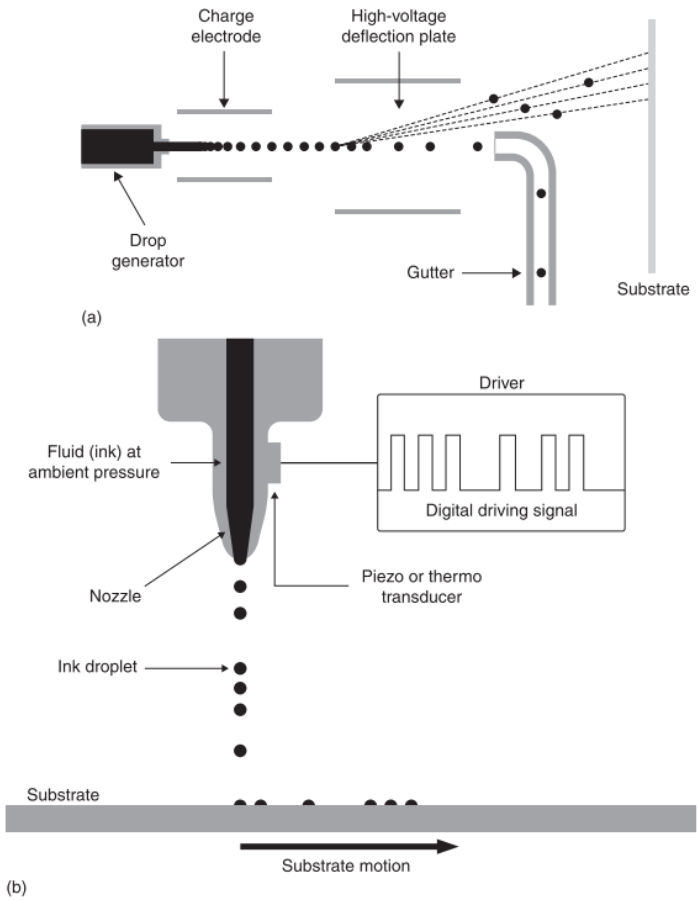


Fig. 1.8 Schematic representation of (a) a continuous inkjet printing (CIJ) and (b) Drop-on-Demand system [1].

# State of the Art

After briefly explaining the most commonly used manufacturing techniques for metal oxide gas sensors, this section summarizes the flexible gas sensors based on metal oxides developed up to date. Amid the fabricated devices are sensors of $NO_2$, $H_2$, $H_2S$, $NH_3$, ethanol ($C_2H_6O$), and acetylene ($C_2H_2$), among others. The works were organized according to the method employed to deposit the active layer. Annex I presents the details about their fabrication in a more condensed way.

## Drop Coating.

Using the drop coating technique to deposit the active layer allows employing transducers fabricated through a variety of techniques.

Shinde et al. [42] fabricated a $NO_2$ gas sensor based on PEDOT:PSS (poly(3,4-ethylenedioxythiophene) polystyrene sulfonate) and $WO_3$ nanoparticles using a coating technique. Over a PET substrate a ZnO layer was sputtered followed by a silver layer to obtain silver electrodes. A solution of PEDOT:PSS-$WO_3$ was coated on silver electrodes. The sensor had a response ($\Delta R/R_0 x100$) of 1.22% to 4 ppm of $NO_2$ at room-temperature.

Choi et al.[43] fabricated an embedded colorless polyimide (cPI) heater over which were drop-coated PdO-$Co_3O_4$ hollows nanocubes functionalized by SWCNTs. The Ni(core)/Au(shell) mesh heater was fabricated by using transfer printing, UV/$O_3$ treatment, reactive ion etching, electrodeposition, and electroless deposition. Once fabricated the mesh of the heater, cPI was coated over it using a doctor blade. Finger electrodes of Cr/Au were formed by e-beam evaporator using a shadow mask. Finally, the nanoparticles were drop-coated over the electrodes. The sensor had a response of 3.09% to 1 ppm of $NO_2$ at 100 °C.

Yaqoob et al. [44] fabricated a $NO_2$ gas sensor based on hybrid $WO_3$ NPs loaded MWCNT-RGO. The substrate used was a commercial PI tape that was attached to a Si substrate during all fabrication steps. The gold electrodes were deposited using photolithography and RF magnetron sputtering. The $WO_3$ NPs loaded MWCNT-RGO solution was deposited by drop coating between the electrodes. Finally, the commercial PI tape was peeled off and attached to a PET

substrate. The sensor had a response of 8.5% to 1 ppm of $NO_2$ at room-temperature.

Similarly, $NO_2$ sensors based on MWCNTs-$WO_3$ nanoparticles were fabricated [45]. Gold electrodes were sputtered over a PET substrate and the MWCNTs-$WO_3$ NPs were gel casted using a doctor blade. The sensors had a response of 8.5% to 1 ppm of $NO_2$ at room-temperature.

Zheng et al. [46] fabricated an ethanol sensor based on ZnO nanoparticles deposited by drop casting. PET coated with ITO was used as a substrate, and the ITO layer was etched by laser ablation to obtain the electrodes. Then, the ZnO nanoparticles dispersed in water were drop-coated. The sensor had a response of 0.15% to 1 ppm of ethanol at room-temperature.

Kim et al. [47] fabricated an alcohol gas sensor by combining spin coating processes and photolithography. Over a Si substrate PI was spin-coated to obtain the flexible substrate. Then, the Si/PI substrate was treated with oxygen plasma to later spun $In_2O_3$ solution and dried it. The $In_2O_3$ layers was patterned by photolithography by using etch-back process. After that PtNPs were spray-coated on them. To fabricate the electrode, a photo resin was patterned to preserve the sensitive layer. AgNWs were spun, dried, dry etched and wet etched. Finally, the PI was peeled off from Si substrate. The sensor had a response of 9502.25% to 1 ppm of ethanol at room-temperature.

Kuru et al. [48] fabricated hydrogen sensors based on $WS_2$ nanosheets. The fabrication implied the dispersion in deionized water of $WS_2$ nanosheets and palladium precursor. A polyimide substrate was coated with the dispersion and then dried. The last step was to deposit Ti/Au contacts by sputtering. The sensor had a response of 10% to 10 ppm of $H_2$ at room-temperature.

Bai et al. [49] obtained a polyaniline-$SnO_2$ heterojunction through combining coating the substrate with $SnO_2$ nanoparticles and in situ oxidative polymerization. The $SnO_2$ nanoparticles were coated and dried over a PET substrate. Then the substrate was immersed in an aqueous solution having the aniline. The polymerization reaction occurred in an ice bath for 30 min. After that, the sample was rinsed with ethanol and dried. The sensor had a response of 212.8% to 1.8 ppm of $NH_3$ at room-temperature.

Jang et al. [50] fabricated a dimethyl sulfide (DMS) gas sensor using $SnO_2$ nanosheets functionalized with Pt. First, a heater embedded substrate was prepared. Silver nanowires AgNWs were transferred to glass-fabric then a polymerization was performed to obtain the hybrid composite film (AgNW-GRFVPH). Over the composite film, gold electrodes were patterned by using a shadow mask and e-beam evaporation. The Pt-$SnO_2$ NSs were coated over the electrodes. The sensor had a response of 348% to 1 ppm of DMS, at 160 °C.

Perillo and Rodriguez [51] used a completely different approach to deposit the sensitive material. Using a polyimide substrate with gold sputtered electrodes, titania nanotube membrane was transferred to the substrate by immersing the substrate in isopropyl alcohol solution having the membrane. The membrane slid over the substrate, then the substrate was removed from the solution. Then a titanium solution was applied over the membrane to facilitate the adhesion between the membrane and substrate. The sensor had a response of 3649.44% to 1 ppm of trimethylamine at 60 °C.

### Direct Growth

It has been proved that metal oxides nanoparticles can be deposited over a plastic substrate by means of chemical polymerization. By this method, it is possible to form heterojunctions of polyaniline and metal oxide nanoparticles. Another method to directly grow nanostructures over a substrate is the hydrothermal method. This method is used to growth nanoparticles in shape of rods or nanowires and has been widely developed to ZnO growth.

Kwon et al. [52] used the hydrothermal process to obtain ZnO NRs over polyimide. The seed layer was deposited by e-beam evaporation. The hydrothermal process was performed in an oven for 30 min at 85 °C. Nickel electrodes were deposited over the ZnO NRs by RF magnetron sputtering. The performance of the sensors was tested through $NO_2$ exposition. The sensor had a response of 6100% to 1 ppm of $NO_2$ at 270 °C.

Using chemical polymerization Li et al. developed flexible $NH_3$ sensors [53,54] based in polyaniline@flower like $WO_3$ or $In_2O_3$ nanospheres@polyaniline. The principal process includes preparing a solution that has metal oxide NPs, aniline, and oxidant. The solution was kept under ice bath and the substrate was

immersed into the solution. After 2 h, the substrate is removed, rinsed, and dried. The sensor based on polyaniline@flower like $WO_3$ had a response of 150% at room-temperature. Instead, the sensor based on Au-$In_2O_3$ nanospheres with polyaniline had a response of 300% at room-temperature.

Yang et al. [55] fabricated a ZnO/ZnS Core-Shell nanowires by localized hydrothermal synthesis. To obtain the flexible substrate, liquid PI was spin-coated over a Si-substrate and cured. To obtain the heater, a photoresist was patterned on the substrate by photolithography, Ti/Pt electrodes were obtained by e-beam evaporation and lift-off processes. After that, another layer of PI was spin-coated over the heater, as insulation between the heater and the electrodes. Again, a photoresist was patterned to deposit Cr/Au electrodes. Photoresist was spin-coated and patterned to open contact pad. Finally, the PI film with the fabricated device was detached form the Si substrate. To grow the ZnO nanowires, the substrate was coated with a ZnO seed solution and heated at 350 °C. Then, using a PDMS mask placed over the electrodes, a ZnO precursor solution was dropped over the electrodes. Voltage was applied to the heater to grow the nanowires. Then, the PDMS mask was replaced and Pd nanoparticle solution was applied same as the ZnO precursor. After the devices were rinsed and dried, a sulfurization process was carried out to form a ZnS layer. The sensing properties of the fabricated devices were tested through $H_2S$ exposure. The sensor had a response of 103% to 1 ppm at 200 °C.

Also, by performing the hydrothermal method without autoclave and outside of the oven it is possible to grow ZnO nanorods. Mohammad et al [56] fabricated a ZnO nanorod using this approach. To fabricate the sensor thermonylon was used as a substrate and was fixed to a microscope slide glass during all the fabrication steps. The seed layer of ZnO was deposited using RF magnetron sputtering with a ZnO target. The hydrothermal reaction was carried out in a hot plate at 90 °C for 3 h. The ZnO NRs were loaded with Platinum and Palladium particles using RF magnetron sputtering. Platinum electrodes were deposited over the ZnO NRs layer using a metal mask by RF magnetron sputtering. The sensor had a response of 10% to 1 ppm of $H_2$ at 180 °C.

Hassan et al. [57] fabricated a sensor based on ZnO nanorods using hydrothermal process. A commercial PI was attached to Si substrate to perform all the fabrication processes. By sol-gel method a ZnO film was deposited over

the substrate as the nanorods seeds. For the ZnO NRs growth, the substrate was immersed in a ZnO precursor solution in a Teflon-lined autoclave. The solution was kept at 90 °C for 4 h, to later be rinsed and dried. A Pt/Pd film was deposited over the ZnO NRs via Pulsed Laser Deposition. Gold electrodes were deposited over the ZnO NRs using a metal mask and RF magnetron sputtering. The sensor was tested at different concentrations of $H_2$. The sensor had a response of 28% to 1 ppm of $H_2$ at 100 °C.

Among the variety of methods to direct growth of metal oxides is the chemical vapor deposition. Ramirez et al. [58] fabricated a flexible gas sensor by depositing $WO_3$ nanowires via Aerosol Assisted Chemical Vapor Deposition (AA-CVD). Ramirez et al deposited $WO_3$ nanowires over a polyimide substrate with inkjet-printed gold electrodes. For the nanowire deposition, the sensor was placed in a hot-wall reactor at 350 °C, and then a precursor solution was vaporized and forced to flow inside the reactor to growth the nanowires. After the precursor solution ran-out and the reactor cooled down, the sensor was removed from the reactor and annealed. The gas sensing properties of the sensor were tested upon $H_2$ exposure. The sensor had a response of 500% to 40 ppm of $H_2$ at 220 °C.

Following the same approach that Hassan et al, Uddin et al fabricated Ag-ZnO nanorods sensors using PET as substrate [59,60]. The seed layer was deposited through a metal mask using RF magnetron sputtering. The ZnO NRs were grown by hydrothermal method. And the ZnO NRs were coated with Ag nanoparticles via RF magnetron sputtering deposition. Acetylene ($C_2H_2$) gas was measured. In the first work, the sensors were exposed to the target gas and light illumination. The sensors had a response of 150% to 1 ppm of $C_2H_2$ at 120 °C. In the second work, the sensors were tested without illumination. The sensors had a response of 100% to 1 ppm of $C_2H_2$ at 200 °C.

Another method to deposit metal oxides particles over the substrate is sol-gel. Subbiah et al. [61] fabricated a ZnO sensor by sol-gel grown over a cotton fabric. For the fabrication, the cotton fabric was activated by argon plasma and the ZnO seed layer was deposited by RF magnetron sputtering. Then, the cotton fabric was dipped in the sol-gel solution at 80 °C for 2 h. The sensor showed high sensitivity to acetaldehyde gas. The sensor had a response of 3200% to 100 ppm of acetaldehyde gas at room-temperature.

## Direct Deposition

The deposition methods grouped in this section correspond to methods in which the metal oxide nanoparticles were synthesized in an earlier step and are not classified as printing methods.

Hassan et al. fabricated [62] a sensor by direct deposit of Mg and Pd nanowires over anodisc membrane. The nanowires were deposited using RF magnetron sputtering. Gold electrodes also were deposited using RF magnetron sputtering using a shadow mask. The fabricated sensor was tested to $H_2$ exposure. The sensor had a response of 0.7% to 1 ppm of $H_2$ at room-temperature.

Kumaresan et al. [63] fabricated a hydrogen sensor based on Indium-Gallium-Zinc Oxide (IGZO). As a substrate, PMMA was spin-coated over a rigid glass slide. Then a negative resist was spin-coated. A layer of $SiO_2$ was deposited through a shadow mask by e-beam evaporation. Then a layer of IGZO was sputtered followed of a layer of Pd deposited by e-beam. Au/Ti electrodes were deposited by e-beam. The sensors had a response of $2.3 \times 10^6$% to 50 000 ppm of $H_2$, at room-temperature.

Hao et al [64] followed the same approaches explained above to grow and deposit $WS_2$ thin films. As substrate they used thin Si substrates. To obtain the substrate Si wafers were etched to ~10 µm. $WS_2$ thin films were grown over the substrates by using DC sputtering. Then a Pd layer was deposited after Al electrodes. The devices fabricated were tested upon $H_2$ exposure. The sensors had a response of 70% to 1 ppm of $H_2$, at room-temperature.

Krsko et al. [65] fabricated a hydrogen sensor over polyimide substrate. The sensor consisted of a $TiO_2$ layer with top electrodes. The $TiO_2$ layer was deposited by DC magnetron sputtering. The electrodes were deposited by magnetron sputtering and patterned by photolithography and Ar ion beam etching. The sensor had a response of 9900% to 1 ppm of $H_2$ at room-temperature.

Kim et al. [66] used an similar approach to transfer printing to obtain arrays of ZnO Nanoflowers. By PDMS rubbing technique patterned polystyrene MPs that were used to obtain ZnO shell arrays. A glass substrate was covered

with photoresist and circular patterns which were obtained by photolithography. Polystyrene MPs were placed on the patterns by PDMS rubbing technique. Then a ZnO film was deposited over the MPs using RF magnetron sputtering. A polyimide substrate was covered with PVP to obtain a receiver substrate. The ZnO shell arrays were transferred to the PVP-PI substrate by applying pressure. Subsequently, the ZnO nanoflowers were obtained by hydrothermal process. SWCNTs top electrodes were deposited using spray coater. The sensor was tested upon $NO_2$ exposure. The sensor had a response of 740% to 1 ppm of $NO_2$, at 270 °C.

Annapureddy et al.[67] sprayed $WO_3$ hollow spheres onto polyimide substrates to fabricate a $NO_2$ gas sensor. The $WO_3$ particles were mixed with a carrier gas and ejected through a nozzle onto a substrate. Once the $WO_3$ layer was deposited, Au/Cr electrodes were deposited via RF magnetron sputtering using a shadow mask. The sensor had a response of 4005% to 2.25 ppm of $NO_2$ at room temperature.

Geng et al [68] deposited ZnO hierarchical structures using a flame torch. A suspension having the as-synthesized ZnO powder was prepared. The suspension was ejected into the flame by a nozzle. To make this deposition technique reproducible, a six-axis robot arm held the flame torch. As a substrate a polypropylene paper, with screen-printed gold electrodes, was used. The sensing properties of the fabricated sensor were tested under light exposure. The sensor had a response of 260% to 1 ppm of $NO_2$ at room-temperature.

Following the direct transfer concept, Seo et al [69] proposed a method for transferring nanowires to flexible substrates. Furthermore, Seo et al fabricated a sensor using their transfer method. The transfer method consists on using a Si nanograting cover with a layer of amorphous carbon. This last is used as sacrificial layer. Then nanowires can be grown over the sacrificial layer by physical vapor deposition (PVD). Later, the sacrificial layer is etched using $O_2$ plasma to facilitate the future peel-off step. To obtain a flexible substrate a liquid phase polymer is poured over the nanowires. Finally, the flexible substrate is peeled off from the Si nanograting. As a demonstration of the method, Seo et al fabricated a $Cu_2O$ sensors that detected $NO_2$, the sensor responses were not clearly stated in the work.

## Printing Deposition

Sakthivel et al. [70] fabricated a flexible CuO sensor using printing techniques. They used a PET substrate, over it, silver electrodes were deposited by screen printing. The electrodes were dried at 120 °C for 20 min. A paste with previously synthesized CuO was prepared. The paste was deposited by screen printing over the electrode area. The CuO layer was dried at 120 °C for 2 hours. The sensor was tested upon different concentrations of $NH_3$. The sensor had a response of 18% to 5 ppm of $NH_3$ at 27 °C.

Also using printing techniques, but with a different treatment after drying the active layer, Dubourg and Radovic [71] fabricated $TiO_2$ sensors. As flexible substrate they used PET. First, silver electrodes were screen-printed over PET. The electrodes were dried in an oven at 110 °C for 15 min. $TiO_2$ particles were dispersed to form a paste which was screen-printed later. The samples were dried at ambient temperature for 2 days. Finally, the sample was laser treated. The sensor was tested upon ethanol exposure. The sensor had a response of 4700% to 100 ppm of ethanol at 25 °C.

In most of the works listed, non-printing techniques were used to deposit the active layer. In contrast, just few works have been developed using printing electronics.

Rieu et al. [72] developed a flexible gas sensor using only inkjet printing technique to deposit electrodes and active layer. The substrate used was polyimide and the electrodes were made of gold ink. After printing the gold ink, the samples were placed in an oven at 250 °C for 3 h to dry and sinter the ink. Electrodes were printed in one side of the substrate; on the reverse a heater was printed. The $SnO_2$ particles were synthesized by sol-gel and properties of the liquid were adjusted to be able to print it. The sensor was tested under exposure to CO and $NO_2$. The sensor had a response of 4200% to 1 ppm of $NO_2$ at 200 °C.

The sputtering is not a large area deposition technique and its use needs of previous and subsequent processes, such as photolithography, etching, plasma treatment, etc. placing the fabrication of flexible sensors at the same level than Si-based sensors regarding to materials, dimensions and costs. The successfully growth of metal oxides over a plastic substrate is demonstrated via hydrothermal synthesis but this technique is not suitable for large area

depositions. Moreover, drop coating is considered a simple deposition method, but it requires to be performed by specialized equipment to deposit material in a reproducible way.

It should be clarified that there are more published works on flexible gas sensors, but these use other types of sensitive materials for detection [73–81]

UNIVERSITAT ROVIRA I VIRGILI
DEVELOPMENT OF FLEXIBLE GAS SENSORS BASED ON ADDITIVE FABRICATION PROCESSES
Miriam Alvarado Pérez

# CHAPTER 2
# $In_2O_3$ Sensors Fabricated by Drop Coating

# $In_2O_3$ Sensors Fabricated by Drop Coating.

## Introduction

This chapter details the fabrication of metal oxide gas sensors using additive deposition techniques and a polymeric substrate. The techniques used were stencil for the fabrication of the electrodes and drop coating for the deposition of the active layer. The sensor responses are contrasted with their rigid sensor counterparts to evaluate the integration of polymeric foil as a substrate for metal oxide gas sensors. The rigid substrates consist of an alumina substrate (25.4 mm x 3.8 mm) with platinum interdigitated electrodes (IDE) and heater. Rigid sensors were obtained by depositing an active layer over the IDE. The flexible sensors fabricated include:

- A flexible substrate, Kapton tape 25.4 µm thick.
- An electrode made of conductive silver ink
- An active layer of indium oxide.

The conditions followed to perform a comparison between the sensors were: the use of the same fabrication technique for the active layer of both types of sensors, the use of the same IDE geometry, and the use of the same type of platinum heater. The use of the same IDE geometry for both types of sensors had the aim to equate the effect that the geometry IDE has on the resistance measurements of the active layer. By using the same type of heater, the flexible sensors can be on a par with the rigid ones, regarding heating conditions. Furthermore, the use of the same type of heater implies that the sensor with the polymeric substrate must be attached to an alumina substrate.

## Sensors Fabrication

The gas sensors were fabricated using a polymeric foil as a substrate. The polymeric foil chosen was Kapton® tape, made from Kapton HN (25.4 µm thickness), with silicone adhesive. The polymeric foil with adhesive can withstand temperatures as high as 260 °C [82]. As the first step, interdigitated electrodes (IDE) were deposited over the substrate. Subsequently, the active layer was

deposited over the electrodes. Furthermore, temperature calibration of the heater was performed to determine the required power to heat the active layer.

## Electrode Fabrication

A stencil technique was used to obtain the electrodes. Given the flexible and adhesive characteristics of the polymeric substrate, it was attached to an alumina substrate. The alumina substrate acted as a holder to facilitate the handling of the sensor in subsequent steps of the experiment.

The stencil technique consisted of depositing ink through a mask. To obtain the masks, a second layer of Kapton tape was attached to the alumina substrate and was cut using a $CO_2$ laser (*Fenix Flayer Laser Marker FEFL-U*). The patterns of the mask were designed using open-source computer graphics software (*InkScape 0.92*). The designs were imported and cut using the proprietary software of the laser. The electrodes were made of silver ink (*DuPont 5064H silver conductor*). Fig. 2.1 shows the outline of the interdigitated electrodes. The fingers of the IDE and the gap are 300 µm wide.

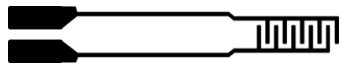

Fig. 2.1 Sketch of the interdigitated electrodes.

The Kapton® tape was cleaned with ethanol (*Ethanol 96%, Sigma Aldrich*) and was used to cover a piece of alumina with two layers of the tape. The covered face corresponded to the IDE; in this way, the heater side was available for power connections, facilitating subsequent steps of the experiment. The outward layer of Kapton® tape was used for the obtention of the mask, over it, the pattern was cut out using the $CO_2$ laser. Then, the layer was cleaned with a cloth moistened with ethanol to remove carbon residues from the laser cut. The areas corresponding to the pattern were removed, creating a negative mask. Then, the silver ink was distributed over the mask with a spatula. The ink was dried in an oven (*Memmet UNE 300*) at 130°C for 20 minutes. After cooling down, the mask was removed, being still over the alumina one layer of the polymeric tape with silver IDE.

It was surmised that the heat dissipation would be higher in the heater side than the electrode side due to the difference in thermal conductivity between alumina and the polymeric substrate. Hence, three layers of Kapton® tape were stuck on the heater side of the alumina substrate to reduce the heat losses, keeping the heater contacts bare. At this point, the substrate with the silver IDE was ready for the active layer to be deposited.

## Active Layer

The indium oxide active layer was deposited by drop coating. In the drop coating technique, a metal oxide powder is mixed with a solvent; the mixture obtained is deposited by controlled injection. A commercially available indium chloride (*$InCl_3$, Sigma Aldrich, St. Louis, Mo, USA, 99.8% purity*) was oxidized to obtain a metal oxide powder. The precursor was heated inside a muffle (*Carbolite Type RWF 12/5*) at 500 °C for 120 minutes. The obtained material was milled until it turned into a fine dust. By this process, a powder of indium oxide was obtained. Then, 20 mg of the powder were mixed with 0.5 ml of 1,2-propanediol (*99.5%, Sigma Aldrich*) and agitated until obtaining a homogeneous suspension.

Afterward, using a micropipette, a droplet of 1 µl of the mixture was deposited on top of the IDE. The sensor was placed inside an oven (*Memmet UNE 300*) at 70 °C to evaporate the solvent. The drop coating process was repeated until the resistance of the active layer reached values below 10 MΩ.

After depositing the metal oxide active layer, sensors were tested through gas exposition. In the case of metal oxide gas sensors, better sensors responses could be obtained by increasing the temperature of the active layer. For the sensors over the polymeric substrate, there was no heater fabricated; the heater of the alumina substrate was used to heat the active layer.

## Heater Calibration

The temperature coefficient of resistivity (TCR) of the platinum heater was obtained experimentally. The heater was placed inside an oven and was heated at temperatures ranging from 50 to 250 °C. The electrical resistance for each temperature was measured.

Afterward, the heaters were characterized by heating with a constant current source and measuring the voltage across the heater. The change in the resistance and the obtained TCR were used to calculate the temperature during calibration.

Because the Kapton is a good thermal insulator, it was important to estimate the temperature that the active layer could reach using the platinum heater. So, by depositing a resistor element instead of the active layer and measuring its resistance changes due to temperature would allow estimating the temperature that the active layer can reach. The outline of the fabricated resistors is illustrated in Fig 2.2, the meander had the same area as the IDE, and the same dimensions (height and width).

Fig. 2.2 Outline of the silver resistor.

Then, resistors were fabricated using the same procedure employed for IDE fabrication and the same ink. The resistors were placed inside the chamber for gas sensing. A constant current was applied to the platinum heaters while the resistance of the resistor was measured continuously. The values of the constant current applied were between 200 to 300 mA. The resistance was measured using a 34970A Agilent Data Acquisition/Switch Unit (*Agilent Technologies, Inc.*). For a better temperature approximation, the test was carried out under synthetic air-dry flow. The temperature reached by the heater, and the resistor, for different constant current values, is shown in Fig. 2.3. The results obtained show a mean difference of 6 °C between the temperatures of both heaters, having the silver heater the lower temperatures.

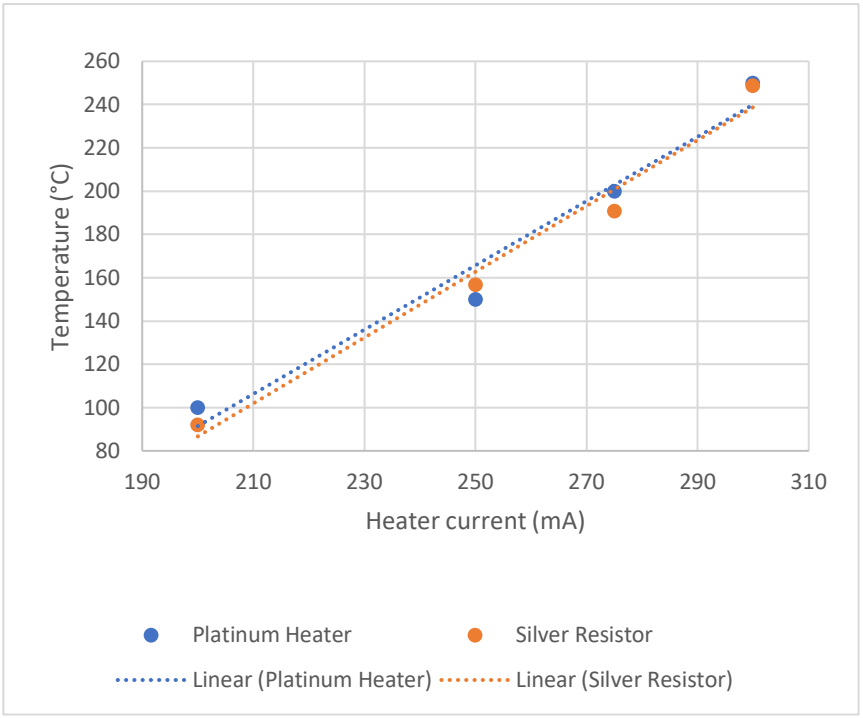


Fig. 2.3 Temperature characterization of the platinum heater and the silver resistor.

## Gas Sensing Setup

The gas detection function of the sensors was examined by placing the sensors inside a Teflon chamber through which a continuous gas flow of 100 ml $min^{-1}$ was forced to pass. During gas measurements, the sensors were 1 h under a flow of synthetic dry air (*Air Premier Purity: 99.995%*) to clean the surface of the active layer. Also, this period allowed the stabilization of the resistance of the sensor. Subsequently, sensors were continuously exposed to one gas concentration for 30 min, and synthetic air for 30 min. The target gases were $NO_2$, $NH_3$, and $H_2$. The concentrations tested were obtained by diluting the gases on synthetic air.

The gas detection was measured as changes in the electrical resistance of the active layer. The resistance was measured using a Keithley Electrometer 6517A (*Keithley Instruments, Inc., Cleveland, Ohio, U.S.A.*) and data was acquired through a custom-made application. A generic power supply was used to apply power to the heaters.

# Results

The drop coating technique used for the deposition of the active layer allowed a complete coating of the area corresponding to the electrodes over the polymeric substrate. This was seen when sensors were examined by E-SEM as shown in Fig 2.4.

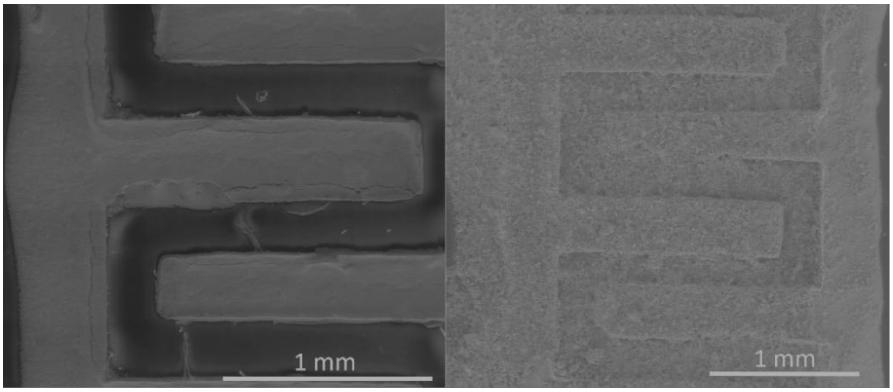


Fig. 2.4 Low magnification E-SEM images of the electrode area of a sensor using a polymeric substrate. Left: Electrode before drop coating deposition. Right: Electrode after drop coating deposition.

Additionally, the E-SEM images clearly showed a difference in the substrates. The images revealed the rough surface of the alumina due to the grain composition of this material. On the other hand, a flat surface was revealed for the polymeric substrate, Fig. 2.5 depicts this difference.

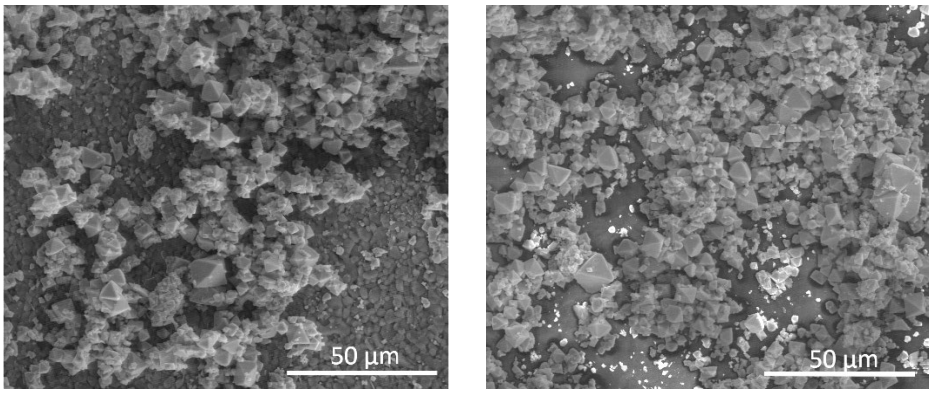


Fig. 2.5 Detail of the active layer deposited over both substrates.
Left: active layer over alumina. Right: active layer over Kapton.

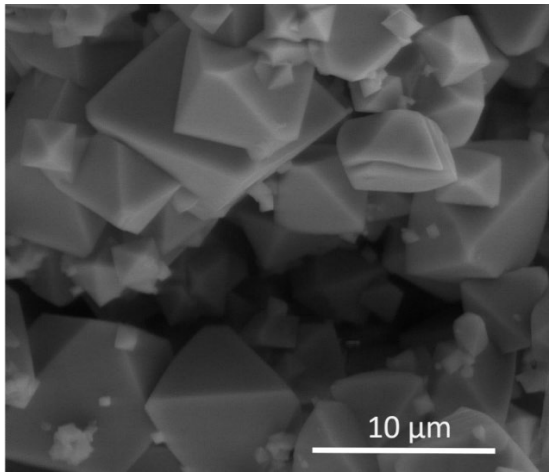


Fig. 2.6 Morphology of the deposited indium oxide layer over Kapton tape.

Furthermore, E-SEM images revealed a layer of indium oxide particles having an octahedral shape (Fig. 2.6). The particle size includes values from 1.25 µm up to 9 µm.

The crystalline structure of the as-synthesized $In_2O_3$ was studied through XRD analysis. The XRD analysis revealed that the diffraction patterns of the grown $In_2O_3$ correlated with the cubic bixbyite $In_2O_3$ structure (*JCPDS card no. 01-071-2194*) corresponding to space group Ia3 with lattice constants of a= 10.12 Å in accordance to previous studies of $In_2O_3$ crystallinity [83–86]. Figure 2.7 shows the XRD pattern of the grown $In_2O_3$ with the most representative peaks labeled.

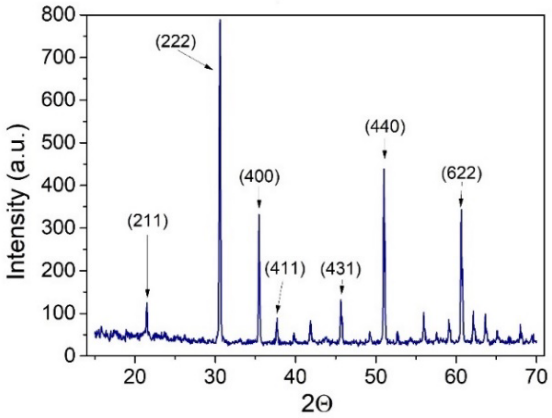


Fig. 2. 7 XRD pattern of the as-synthesized $In_2O_3$.

The sensors were tested using $NO_2$, $NH_3$ and $H_2$ gases, and under different operating temperatures (100, 150, 200, and 250 °C). The as-synthesized indium oxide showed an n-type semiconductor behavior. This was confirmed with the increase of the resistance in the presence of oxidizing gases ($NO_2$) and the decrease in the presence of reducing gases ($NH_3$ or $H_2$).

## Sensors Comparison

Since indium oxide has been shown to be more sensitive to $NO_2$ [87,88], both types of sensors, either using alumina or polymeric tape, were tested through $NO_2$ exposure. The $NO_2$ concentrations measured were 3, 5, 5.5, and 6 ppm. The interaction between the $NO_2$, an oxidizing gas, and $In_2O_3$, a n-type material, caused an increase of the sensor resistance. Several studies reported an ideal operating temperature for $NO_2$ detection in the range of 100 and 150 °C [88–92], for this reason the sensors were tested at these temperatures. The response and recovery for sensors over rigid and polymeric substrate to different concentrations of $NO_2$ at 150 °C is presented in Fig. 2.8, where the sensor resistance was normalized ($R/R_0$).

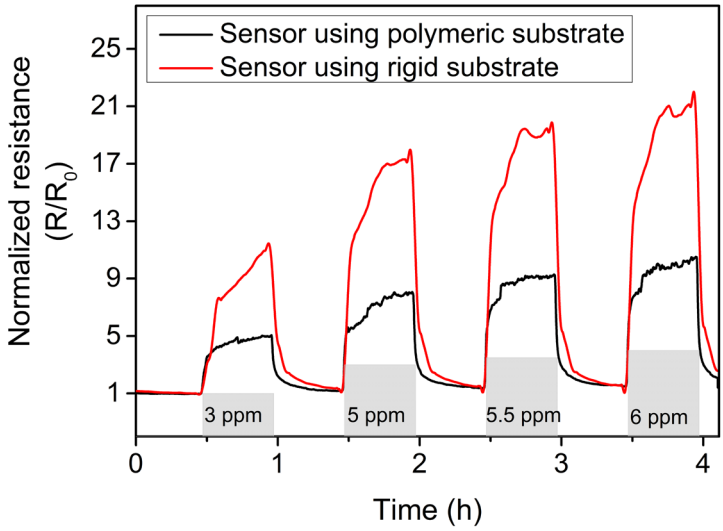


Fig. 2.8 Normalized dynamic responses during one cycle of $NO_2$ measurements at 150 °C.

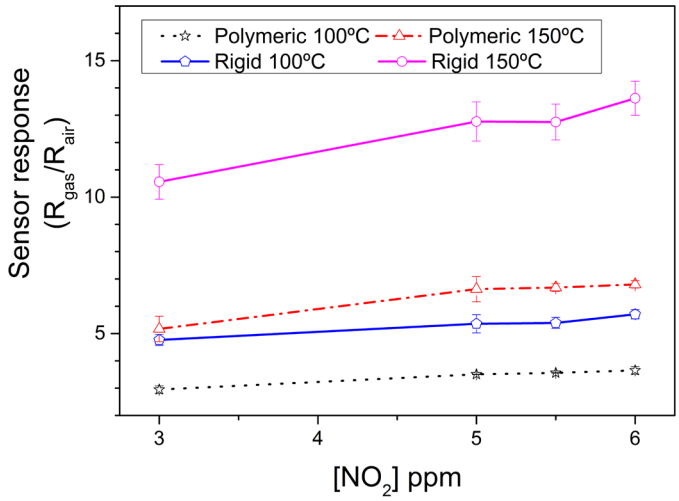


Fig. 2.9 Sensors responses as a function of the temperature.

The sensors responses as a function of temperature revealed that higher responses are obtained at 150 °C for both types of sensors, as shown in the Fig. 2.9. Furthermore, Fig. 2.9 shows that all the sensors have the same behavior towards $NO_2$ exposure. Also, sensors fabricated using a polymeric substrate had lower responses than sensors on the alumina substrate.

Since the sensors were fabricated using the same sensitive material and the same geometry, they were also measured under the same conditions (temperature, gas flow, etc.), it was concluded that the difference between their responses was due to the different electrode materials.

In the literature, we can find a lot of studies where it was proven that the electrode material has interference in the sensor response [93–100]. From all these studies, it is possible to summarize four aspects of the metal-MOX junction that influence the sensor performance:

- Potential barrier (Schottky) between the metal-MOX interface.
- Diffusion (auto-doping) of the metal into the MOX.
- Deposition method of the electrode.
- Catalytic activity of the metal electrode.

**Potential Barrier**

When a metal is in contact with a semiconductor, the Fermi level of the semiconductor adjusts to and aligns to with the Fermi level of the metal by an amount equal to the difference between the two work functions of the two materials [101]. This difference is the Schottky barrier height. Theoretically, the Schottky barrier is the difference between the work function of the metal and the electron affinity of the semiconductor. The electron affinity is the energy difference of an electron between the vacuum level and the lower edge of the conduction band. The work function is the amount of energy needed to remove an electron from the Fermi level to just outside of the metal with zero kinetic energy.

$$\Phi_B = (\Phi_m - \chi)$$

For metal-semiconductor junctions which have low Schottky barrier, the current flows in both directions, these are non-rectifying junctions ($\Phi_m < \Phi_s$) it is said that the junction has an ohmic contact. When ($\Phi_m > \Phi_s$), the junction forms a rectifying Schottky barrier and the current only flows in one direction.

When a metal-semiconductor junction is in thermal equilibrium there is a contact potential difference that is given by the difference between the work functions of both materials:

$$eV_{bi} = (\Phi_m - \Phi_s)$$

Where $V_{bi}$ is known as 'contact potential difference' or the built-in potential of the junction and is expressed in volts, $eV_{bi}$ is the potential barrier which an electron moving from the semiconductor into the metal must surmount [101].

These barriers contribute to the overall sensor resistance. For this reason, it is desirable to have a metal-semiconductor junction with an ohmic contact. In this way, the contact resistance is reduced, and the resistance changes due to intergranular contact can dominate the sensor resistance changes. Moreover, when the junction barriers are larger (Schottky barrier) they can react with the gas altering the sensor performance [39].

**Diffusion (auto-doping)**

Among the metals used for electrodes, silver and gold electrodes have tendency to diffuse into the semiconductor layer. For instance, the mobility of silver occurs at temperatures between 300-400 °C. When the mobility occurs, atoms of the electrode migrate to the semiconductor layer occurring a doping effect. For instance, it was found that silver electrode $SnO_2$ sensors had the same response than gold electrode Ag-doped $SnO_2$ sensors [100]. Also, it was found that Au atoms diffused into $SnO_2$ layer, lowering the operating temperature of the sensor [93].

**Deposition Method**

The purity percentage of the metal deposited to fabricate the electrodes varies according to the technique used. While for an electrode deposition by sputtering, the target deposited is a metal with elevated levels of purity, the inks used for printing processes contains around 60% of metal and binders that can interfere in the contact of the metal-semiconductor junction or can react with the semiconductor. The lower content of metal and the presence of binders could contribute to the reduction of the sensor responses [99].

**Catalytic Activity**

The materials used for electrode fabrication – Pt, Pd, Au, and Ag – have catalytic properties. The improvements in the sensor response can be explained by the spillover effect. The electrode material facilitates the activation of the gas particles. Gas particles reach the semiconductor surface, and the reaction occurs. On the other hand, the catalytic reaction could occur on the electrode material with direct desorption which will lead to a reduction of the analyte concentration, diminishing the sensor signal.

From the aspects described above, the factor that could explain the difference between the responses of the sensors fabricated over Kapton and the sensors fabricated over alumina substrates is the potential barrier of the metal-MOX junctions. The work function of the indium oxide has been calculated between 5-6 eV [102,103]. Instead, the work function of the pure silver and platinum are 4.26 eV and 5.65 eV, respectively. It is clear that the Ag-$In_2O_3$

junction has the bigger contact potential difference having a bigger contribution to the sensor impedance.

From here, more gas sensing measurements were performed exclusively using the sensors fabricated using the polymeric foil. The gases tested were reducing gases, $H_2$ and $NH_3$.

## $H_2$ sensing

The sensor response to different concentrations of $H_2$ was examined. The Fig. 2.10 shows the normalized resistance of the sensor ($R/R_0$) for one cycle of $H_2$ measurements at 250 °C. Where $R_0$ is the initial resistance before exposure to $H_2$ gas, and R is the measured resistance during the test.

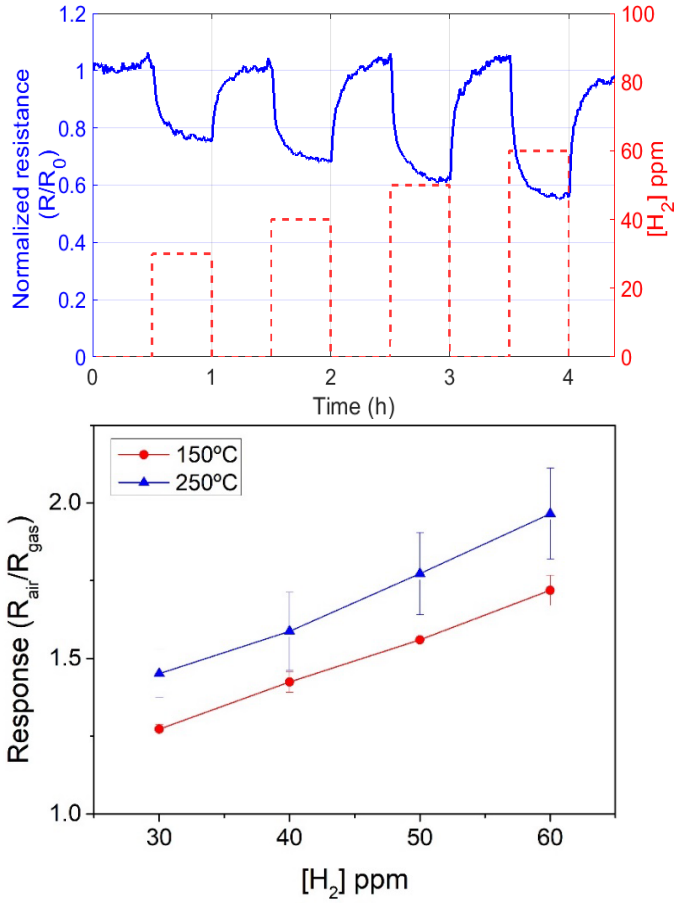


Fig. 2.10 Normalized dynamic response of one sensor during one cycle of $H_2$ measurements (upper). Effect of the temperature on the sensors response (lower).

After stabilizing the resistance of the sensor, the applied gas pulses caused a decrease of the resistance. Then, synthetic air was applied again to return to the resistance baseline. The resistance showed a drift when retrieving the baseline. The analysis of the gas measurements at different temperatures revealed that $In_2O_3$ sensors had the higher responses at 250 °C. Fig. 2.11 shows the sensor calibration curve towards different concentrations of $H_2$ at 250 °C.

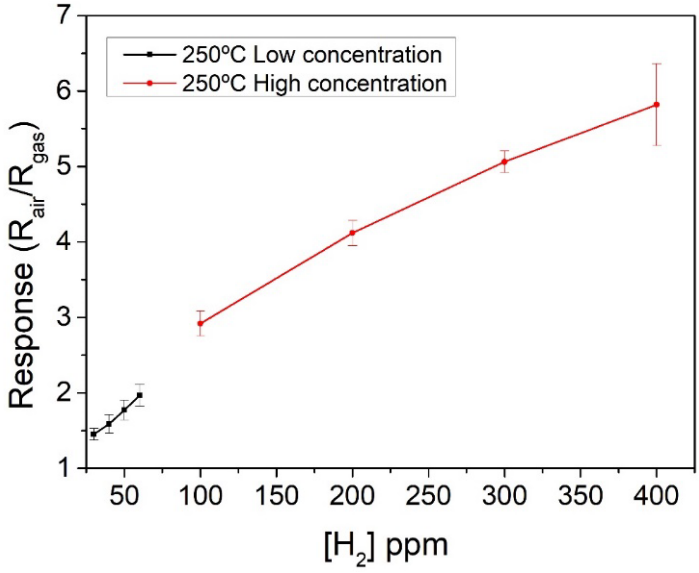


Fig. 2.11 Calibration curve for $H_2$ exposure at optimal working temperature (250 °C).

## $NH_3$ Sensing

The sensors response to different concentrations of $NH_3$ was examined. Fig. 2.12 shows the normalized resistance ($R/R_0$) for one cycle of $NH_3$ measurements at 150 °C. Gas pulses of $NH_3$ caused a decrease in the resistance of the sensors, according to the n-type behavior of the $In_2O_3$.

The sensors response as a function of the temperature was investigated. Fig. 2.13 shows the sensors response for different operating temperatures. It was found out that sensor responses were higher when the sensor was working at 150 °C.

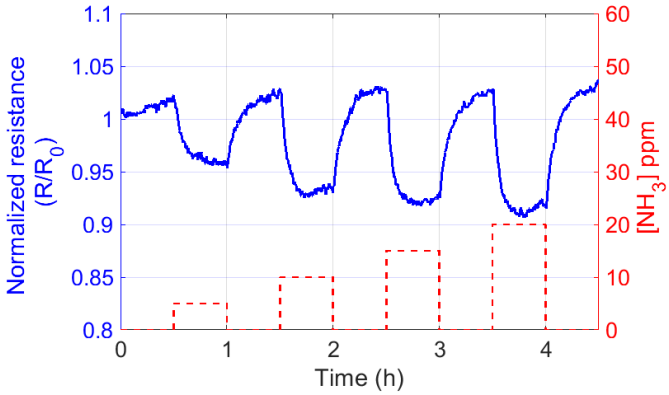


Fig. 2.12 Normalized dynamic response of one sensor during one cycle of ammonia measurements at 150 °C.

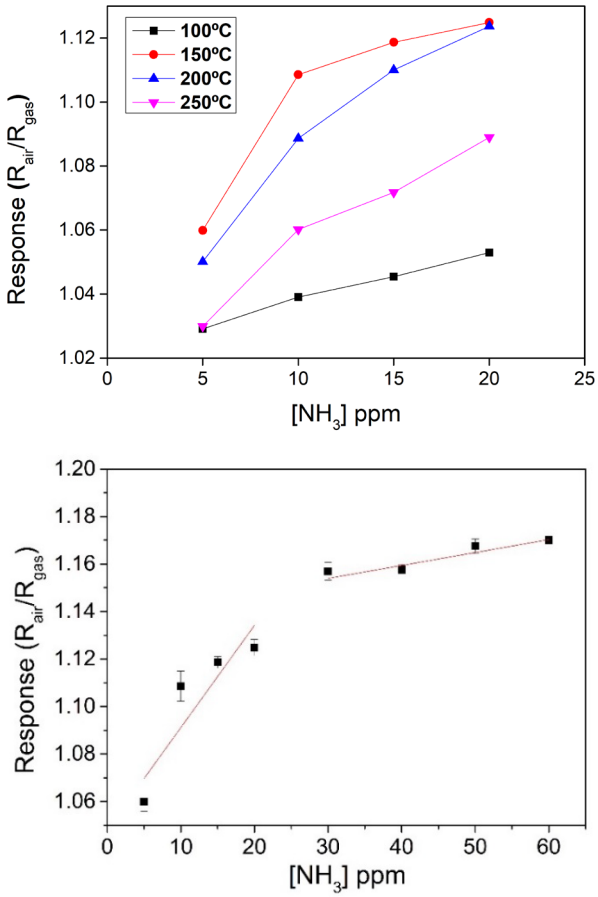


Fig. 2.13 Sensors response as a function of the temperature (upper). Calibration curve for $NH_3$ exposure at optimal working temperature (150 °C) (lower).

# Discussion

The elementary drop coating technique employed for the fabrication of the sensors allows depositing the active layer at low temperatures, below 150 °C. A good covering of the electrode area was achieved using this technique. Therefore, it is suitable for the fabrication of flexible gas sensors, even using other flexible substrates, such as PET or paper. Furthermore, the integration of particles synthesized at temperatures beyond the working temperature of the flexible substrates opens a range of possibilities to fabricate flexible gas sensors. Also, there is a point of improvement if specialized equipment is used to perform the drop coating deposition.

The precursor synthetization method presented allowed fast and simple obtention of sensitive material compared with other methods, such as Chemical Vapor Deposition (CVD) or Vapor Phase Transport (VPT). The flexible substrate employed made a significant difference in the fabrication cost comparing with the traditional rigid substrates. The cost of the required polymeric substrate to fabricate one transducer is approximately two thousand times lower than the cost to fabricate one transducer on an alumina substrate. The gas sensing results showed satisfactory performance of the fabricated sensors. The maximum operating temperature of the sensor was limited to around 250 °C because the conductive tracks presented damages when the sensor was heated at that temperature. Furthermore, the adhesive Kapton® tape can withstand temperatures around 280 °C.

# CHAPTER 3
# Flexible Gas Sensor Fabricated by AA-CVD using Silver Electrodes

# Flexible Gas Sensors Fabricated by AA-CVD using Silver Stenciled Electrodes.

## Introduction

Among the different metal oxide nanoparticle structures, nanowires present excellent properties for gas sensing: exceptionally large surface to volume ratio, superior stability thanks to their high degree of crystallinity, possibility of reaching high integration densities, simple and low-cost preparation methods and their easy integration into devices [104,105]. The deposition of nanowires as an active layer of flexible gas sensors represents a challenge, because nanowires require high deposition temperatures, and there are few flexible substrates available in the market that can withstand these temperatures.

It has been proved that tungsten trioxide ($WO_3$) nanowires can be deposited through AA-CVD at temperatures under 400 °C [106,107]. Deposition temperatures below 400 °C are compatible with the properties of Kapton. Thereby, in this work AA-CVD has been chosen as direct grown metal oxide technique and $WO_3$ nanowires were selected as sensitive layer. The sensors fabricated comprise:

- A flexible substrate, Kapton, with 50 µm thickness.
- Electrode and heater made of conductive silver ink.
- Active layer of tungsten trioxide nanowires or tungsten trioxide nanowires decorated with palladium.

This chapter describes how the AA-CVD deposition process for rigid substrates was adjusted for flexible substrates. Sensing properties of the flexible sensors before and after a bending process were studied. The bending process was carried out under controlled conditions to induce a reproducible and reliable bending of the sensor, through the use of a specialized testing machine. Additionally, it allowed the cyclic bending of the sensor. The study included three stages:

1. Gas sensing test.
2. Bending test.
3. Gas sensing test.

# Sensors Fabrication

## Conductive Tracks

In literature, it is possible to find MOX gas sensors fabricated using a variety of configurations for the electrodes [108]. The most spread configuration is interdigitated electrodes. In an interdigitated geometry, the electrodes can be at the top or at the bottom of the active layer. The heater is at the backside or surrounding the electrodes. If the heater is at the backside, the fabrication steps can increase and become more complex. If the heater is under the sensitive layer, a dielectric layer will be necessary. The deposition of a dielectric layer increases the fabrication steps. Finally, if the heater is surrounding the electrodes, the size of the sensor increases, and temperature homogeneity decreases.

Bearing in mind the aim of reducing the number of steps and simplifying the fabrication, a geometry of one heater and one coplanar electrode was used. The active layer is deposited over both elements. Since there is only one electrode, the heater acts simultaneously as second electrode.

For the design of the heater some aspects must be considered such as its geometry, the electrical properties of the material, and the fabrication limits. The relationship between these variables is described by Pouillet's Law. It relates the resistance of a conductor with its resistivity and geometry as follows:

$$\boldsymbol{R = \rho \frac{l}{A}} \qquad \textit{Eq. 3-1}$$

where:

A= Cross-sectional area of the conductor

*l*= length of the conductor

ρ= resistivity of the material

Pouillet's Law is valid for three-dimensional geometries. In the case of two-dimensional geometries, such as thin films, the relation can be rewritten as:

$$\boldsymbol{R = \rho \frac{l}{A} = \rho \frac{l}{Wt}}$$

where the cross-sectional area is replaced for the width (*W*) and the sheet thickness (*t*). For thin films is assumed a constant thickness, then the relation can be written as:

$$\boldsymbol{R = R_s \frac{l}{W}} \qquad \textit{Eq. 3-2}$$

where $R_s$ is the sheet resistance. According to Eq 3-2, if the aspect ratio is maximized, higher values of resistance will be obtained.

Although our stencil technique has a resolution of up to 150 µm, the dimensions selected for the heater design were higher, because it is of paramount importance to prevent electrical interactions between the heater and electrode. The chosen track width and gap between electrodes were 400 µm. The design had a size of 19.30 mm x 15.55 mm. Fig. 3.1 shows the stenciled design used for gas sensor electrodes. The design had six contacts, from left to right 1 to 6. The external contacts (1 and 6) were used for the bending test measurements. The second and third contacts were used to apply power to the heater. The fourth and fifth were used to apply voltage to the active layer.

The process to fabricate the conductive tracks that were used as electrode and heater is explained below. First, Kapton was cut in pieces of 75 mm x 25 mm approx. Then, the pieces were cleaned to eliminate impurities. For cleaning, the pieces were immersed in acetone (*Scharlau*, *99.5%*) for 5 minutes, then in ethanol (*Sigma-Aldrich, 96%*) for another 5 minutes. Finally, they were rinsed with deionized water and dried in an oven at 110 °C for 10 min.

Subsequently, the stencil procedure explained in Chapter 2 was followed to obtain conductive tracks over the Kapton pieces. The silver ink used was DuPont® 5064H and was dried at 130 °C for 20 min.

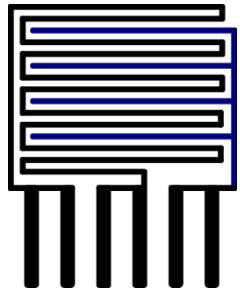

Fig. 3.1 Design of heater and one electrode.

## Metal Oxide Deposition

For the obtention of pristine $WO_3$ nanowires, a precursor solution having 15 ml of acetone (*Scharlau, 99.5%*), 5 ml of methanol (*Scharlau, 99.9%*), and 50 mg of tungsten hexacarbonyl (*$W(CO)_6$, Sigma-Aldrich*) was prepared. A piece of Kapton with conductive tracks was placed in the reactor. The area of the sensitive layer was defined through a Kapton mask to avoid the deposition of nanowires over the contacts. Both substrate and mask were fixed using Kapton Film Tape. Then the reactor was heated to 350 °C at a rate of 1 °C per minute to avoid deformation and damage of the sample due to the difference between the CLTE of both materials. Once the programmed temperature was reached, the precursor solution was nebulized; the vapor was introduced to the reactor with a flow of nitrogen. The deposition process finished when the precursor solution ran out. Then the nitrogen flow was stopped, and the reactor was allowed to cool. When the reactor was at room temperature, both pieces of Kapton were removed and separated. Then annealing was done to remove the solvent residues. The annealing temperature was 350 °C for 4 hours with a heating rate of 1 °C per min.

For the obtention of $WO_3$ nanowires decorated with palladium, the same procedure to obtain pristine nanowires was followed. Just 1.5 mg of palladium (II) acetylacetonate (*$Pd(C_5H_7O_2)_2$, Sigma-Aldrich*) were added to the solution before it was nebulized.

Environmental Scanning Electron Microscope (E-SEM) images showed the nanowires layer obtained. The nanowires covered the areas corresponding to the substrate and electrodes showing uniform growth over all the surfaces and edges.

The images revealed nanowires randomly oriented with diameter ranging between 100 to 150 nm and a length of 10 µm. Fig. 3.2 shows E-SEM images of the deposited $WO_3$ nanowires over an edge of the electrode.

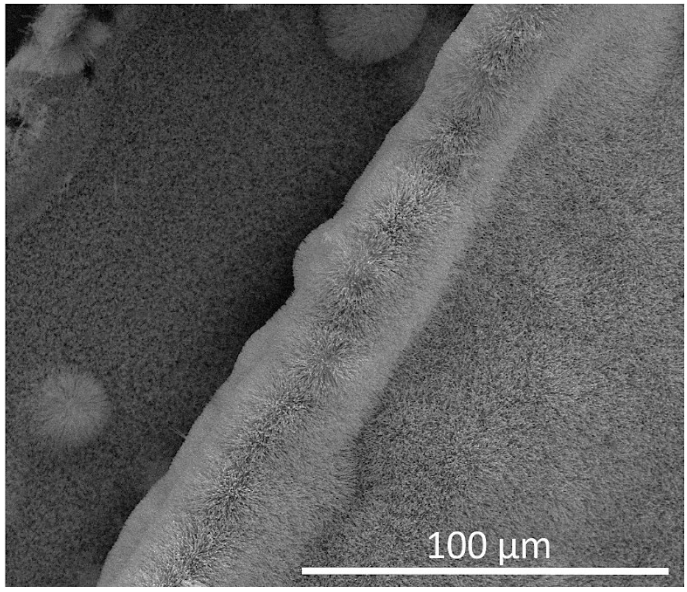


a)

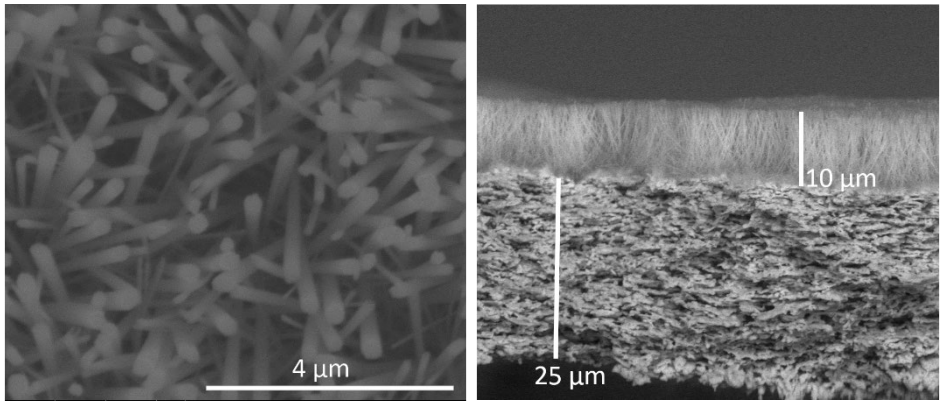


b)

Fig. 3.2 E-SEM images of the $WO_3$ nanowires deposited over the substrate. a) The edge of one silver track covered with $WO_3$ nanowires at low magnification (800x); b) High magnification images of the $WO_3$ nanowire layer obtained and cross-section image of a nanowire layer over a silver track.

## Heater Calibration

In metal oxide gas sensors, the gas sensing properties of metal oxides are temperature dependent. Since the adsorption of the oxygen and reaction rates of the target gas are temperature dependent [109], it is recommended to have operating temperatures higher than room temperature. Hence the heater becomes a necessary part of the sensor architecture. Through temperature modulation, it is possible to find the ideal operating temperature of the sensor [110]. Moreover, the operating temperature influences the reliability and durability of the gas sensor [4]. Therefore, on the sensor design, a heating element is included. The heaters were made of conductive silver ink. The relationship between the electrical resistance of the heater and temperature is given by the following equation:

$$\mathbf{R = R_0\,(1 + \alpha \Delta T)} \qquad \textit{Eq. 3-3}$$

where:

$R_0$ is the electrical resistance at temperature $T_0$

$\Delta T$ is the difference between T and $T_0$

$\alpha$ is the temperature coefficient of resistivity of the material

The temperature coefficient of resistivity of the conductive tracks of silver was obtained empirically. Samples were placed inside an oven to measure the electrical resistance of the tracks for a temperature range between 25 and 200 °C. The electrical resistance was measured using the 4-wire mode of a digital multimeter (*HP34401A, Keysight Technologies*). Fig. 3.3 shows the resistance changes of the silver tracks due to temperature. Once the temperature coefficient was calculated, it was possible to estimate the temperature changes of the heater upon an applied voltage using Eq. 3-3.

Furthermore, the heat propagation over the sensor was analyzed through infrared images (IR). The IR images were taken using a FLIR T420 Thermal Imaging Camera with a resolution of 320 x 240 pixels. The measurements were carried out in ambient laboratory conditions. The estimated voltage to raise the temperature of the sensor to 150 °C was applied to the heater. The IR images (Fig. 3.4) showed the areas corresponding to the heater as the zones with higher

temperatures. Instead, the temperature of the electrode decreases as the distance between the heater and the electrode increases. The IR images revealed a temperature gradient of the active layer of 19 °C. Furthermore, it is possible to observe cooler areas that correspond to the electrode and heater gaps.

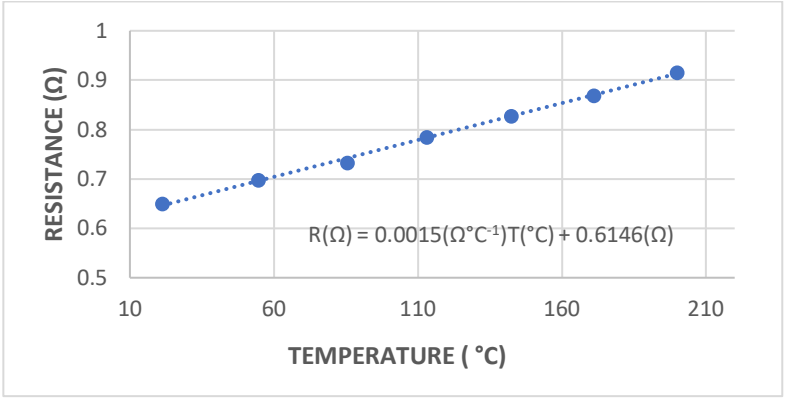


Fig. 3.3 Linear behavior of the resistance vs temperature relationship for the silver conductive tracks.

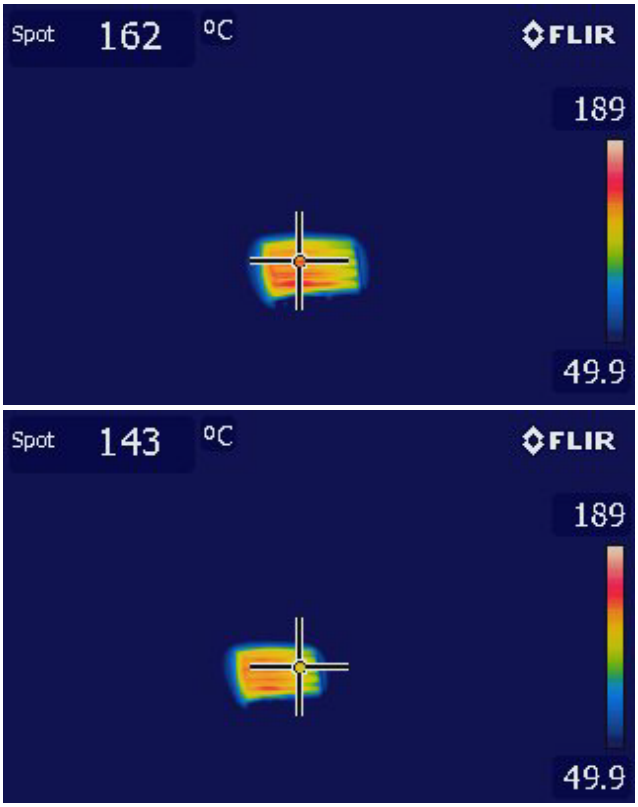


Fig. 3.4 Infrared images of the sensor while applying power to the heater to reach 150 °C.

During gas sensing measurements, the temperature was calculated based on the values of the heater resistance because the resistance value of the fabricated heaters is not standard. Then a single calibration would not be enough to know the exact values of power needed to reach the desired temperature on each sample.

## Setup for Gas Sensing

The setup for gas sensing comprises:

- Two calibrated gas bottles, one for the target gas and another for synthetic dry air.
- Two mass flows controllers connected to the gas bottles.
- 1 computer used to drive the mass flows controllers, and to control the electrical measurements.
- Data acquisition equipment
- Power supply
- A chamber, in which the sensor to be tested is placed.

The mass flows controllers are two Bronkhost Hitech 7.03.241. FlowPlot 3.35 software allows to configure the flow and gas concentrations. For gas sensing measurements, a gas flow of 100 ml $min^{-1}$ is passed through the chamber. The FlowPlot software allows to program gas pulses, create cycles and repeat them as many times as needed.

For gas sensing tests, first the sensors are exposed to synthetic dry air (*Air Premier Purity: 99.995%*) until it reaches the steady state and then exposed to pulses of different gas concentrations. This cycle is repeated 3 times. The gas measured was hydrogen. Sensor response (R) was defined as R = Ra/Rg, where Rg and Ra are the sensor resistances while the target gas is present and at stationary state in synthetic air, respectively.

A Keithley 2410 Source Meter Unit (*SMU*) controlled by PC is used as data acquisition equipment. An Agilent N5752A is used as a power supply. A custom-made software application was developed to control the data

acquisition equipment and the power supply. This application allows monitoring in real time variables such as voltage, current intensity, sensor resistance, heater resistance, and heater temperature. The program bases all the calculations on Eq. 3-3.

The program needs the following initial values:

- Heater resistance at room temperature ($R_0$),
- temperature coefficient of resistivity ($\alpha$) of the heater's material,
- setpoint temperature ($\Delta T_s$),
- range of the setpoint temperature, and
- voltage and limit of current for each channel ($V_h$, $V_e$, $I_{Lh}$, $I_{LE}$).

At the beginning of the program execution, the SMU applies the initial voltage ($V_h$) to the heater and measures the current intensity ($I_h$) that passes through it. Then, the program calculates $\Delta T_c$. During the first 5 minutes of program execution, the initial voltage applied to the heater ($V_h$) remains constant. It is kept constant to stabilize the heater resistance value and avoid peaks of current. Afterwards, the program calculates the voltage ($V_h$) to keep the temperature within the range of the setpoint temperature. The SMU then applies the calculated voltage to the heater.

At the end of each iteration, the program stores the voltage, current intensity, and resistance of each channel, as well as the heater temperature in a CSV file.

The chamber consists of two pieces that are joined horizontally by screws forming a square prism horizontally oriented. The chamber has one inlet for the gas mixture and one outlet that works as exhaust. The inlet and outlet are in the lateral faces of the upper piece /part. The inner hollow shape of the upper part holds the gases allowing the interaction between gas particles and the active layer of the sensor. The chamber is made of Teflon. The chamber allows measuring one sensor at a time. The bottom part has a connector at the center of its inner face. The sensor is plugged to the connector, holding a vertical position, and the active layer is parallel to the flow. This allows measuring the

sensor from the exterior of the chamber. The connector is an FFC/FPC connector, of the series FDZ, of type Zero Insertion Force (ZIP). The connector has a pitch of 2.54 mm, current rating of 1.0 A, voltage rating of 250 V and is top entry type. Fig. 3.5 shows a photograph of the chamber, opened and containing a sensor.

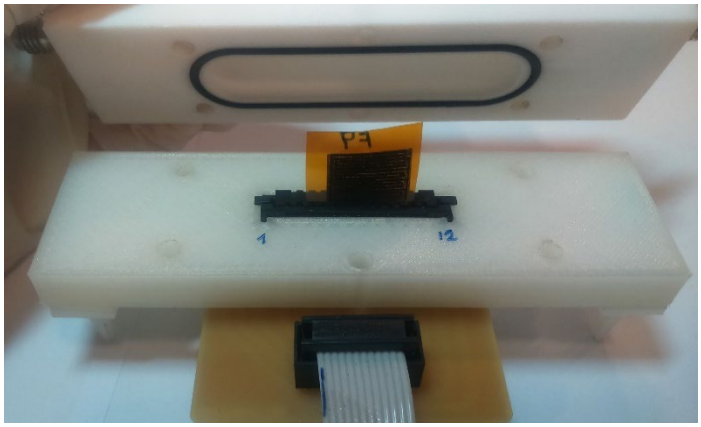


Fig. 3.5 Digital image of the sensing chamber containing a sensor.

## Bending Test Setup

The concept of flexible gas sensors envisages that these can be molded to their final application. This implies that their operation should not be altered when they are subjected to bending. Thereby, the sensors were subjected to bending tests. The sensors can be bent in two ways: inward and outward. During inward bending, the elements of the sensor are in the concave side of the curve formed by the sensor. Instead, during outward bending, the elements of the sensor are in the convex side. To clarify, in the literature it is possible to find the inward bending as compression bending or compressive strain, and outward bending as tension bending or tensile strain [111,112].

Sensors were bent using a universal testing machine AGS-X 10 kN Shimadzu. The universal testing machine ensured controlled, repeatable and cyclic bending conditions. Trapezium X Materials Testing software was used to acquire stroke and force parameters. Meanwhile, during the entire bending test, an external data acquisition switch unit (*Keysight 34972A*) monitored in situ the electrical resistance of the sensor (the electrical resistance of the active layer measured through the electrodes). The idea of

monitoring in situ the electrical resistance of the sensor was to examine the effects that deformation has over it. The monitoring of the electrical resistance can alert of damage due to the bending test. Also, a significant increase of the electrical resistance would indicate breaking of the conductive tracks or active layer. In the case of non-aligned nanowires, a decrease in the electrical resistance of the sensor means that nanowires are closer, more of their surface is touching other nanowires. While an increase in the electrical resistance means that nanowires are starting to separate, the distance between nanowires is becoming larger. Drastic increases would mean that the breaking either of the tracks or the active layer occurred. These effects are dominated by orientation, distribution, and length of the nanowires as well as tracks surface.

For the bending test, the grips of the universal testing machine held the sensor by its ends. Between the grips, only the area corresponding to the active layer was held. The universal testing machine holding a sensor is illustrated in Annex II. The machine was programmed in compression mode. In compression mode, the upper crosshead moves down a controlled vertical displacement (stroke), ΔL, and returns up to complete a cycle. During this cycle, a compression force is exerted, and the sample is buckled achieving a maximum deflection (f). The deflection was calculated assuming that both ends are fixed, the buckled length of the sample is $(L_0 – \Delta L)/2$ and the buckling deformation has a parabolic shape as Fig. 3.6 represents.

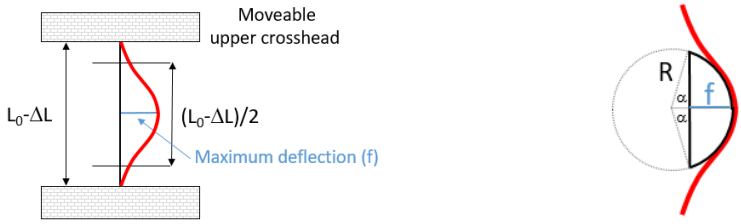


Fig. 3.6 a) Schematic representation of the experimental setup of the sample buckled where the main parameters are highlighted, b) relationship between radius of curvature and deflection.

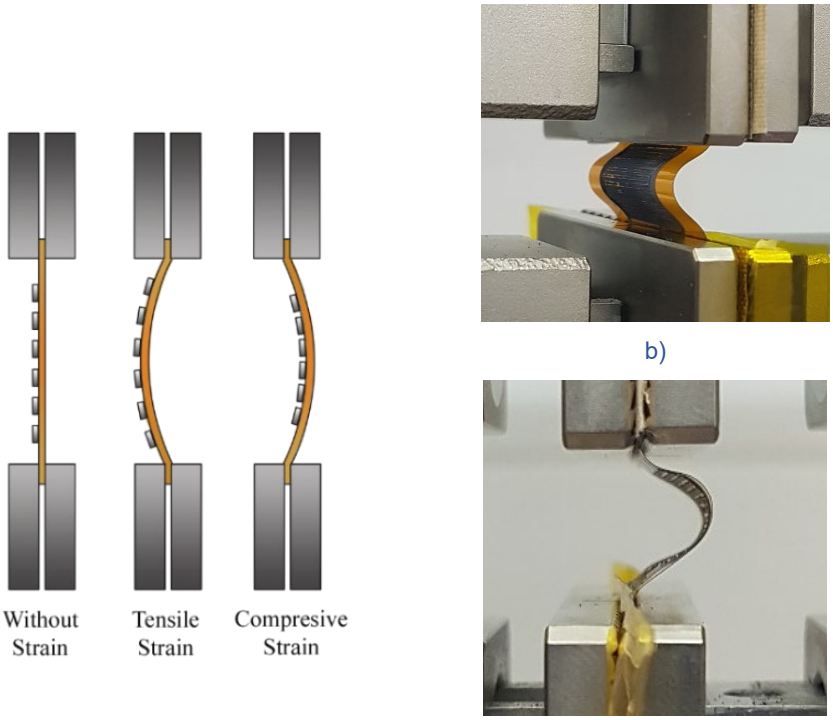


Fig. 3.7 a) Scheme of the sensor in different bending conditions. Digital images of the sensor under b) tensile strain and c) compressive strain.

The shape of the buckling deflection shows if the sensor is subjected to tensile strain or compressive strain. Fig. 3.7 illustrates the sensor subjected to the two types of deformation. During the test, the sensors were bent 50 cycles with a stroke of 2 mm, at a velocity of 20 mm/min and under tensile strain.

## Results

As mentioned earlier, the study comprised three stages: 1) Gas sensing test, 2) Bending test, and 3) Gas sensing test. For comparison purposes, the same sensing conditions were set for stages 1 and 3. The gas sensing test consisted of three repeated test cycles of 3 different $H_2$ concentrations each one, at 150 °C.

Fig. 3.8 shows the evolution of one $WO_3$ sensor resistance during a three-pulses cycle of gas measurements, and the sensor responses ($R_a/R_g$) of the tested sensors. The concentrations tested were 250, 500, and 750 ppm of $H_2$.

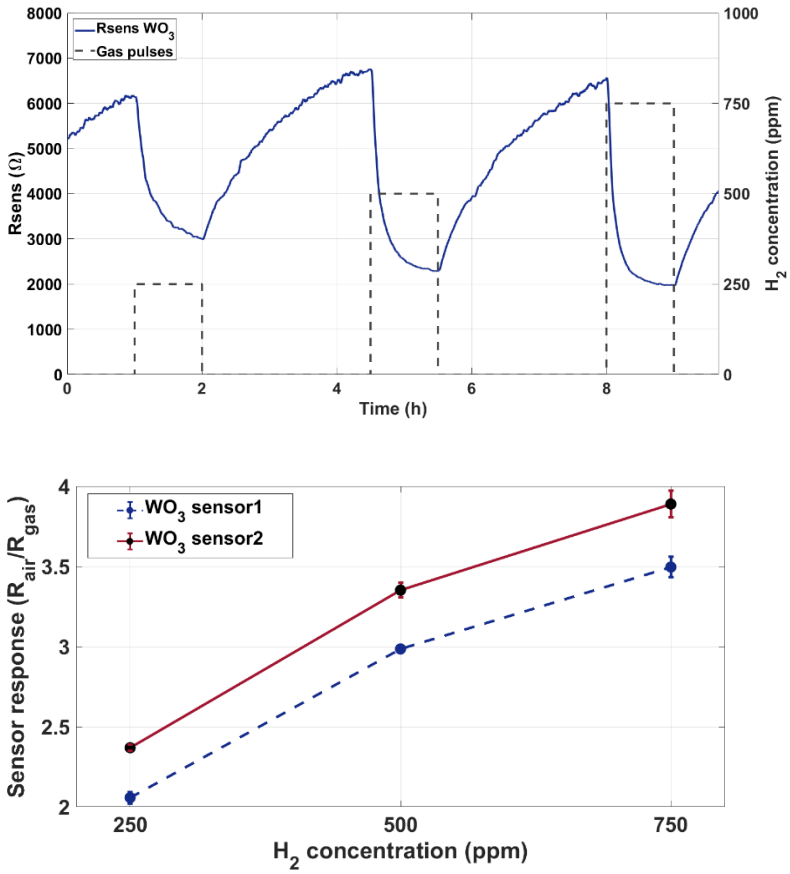


Fig. 3.8 Sensor resistance and responses for a $WO_3$ sensors to three $H_2$ concentrations at 150 °C

The gas sensing measurements were carried out at 150 °C. The $WO_3$ sensors presented the same response behavior with a difference in the values of the response due to each sensor coming from a different fabrication batch.

Fig. 3.9 shows the evolution of the resistance of one $WO_3$ decorated with palladium ($WO_3$-Pd) sensor during a three-pulses cycle of gas measurements, and the sensor responses ($R_a/R_g$) of the tested sensors. The concentrations tested were 250, 500, and 750 ppm of $H_2$. The gas sensing measurements were carried out at 100 °C. The difference between sensor responses is due to the fact sensors were fabricated in batches.

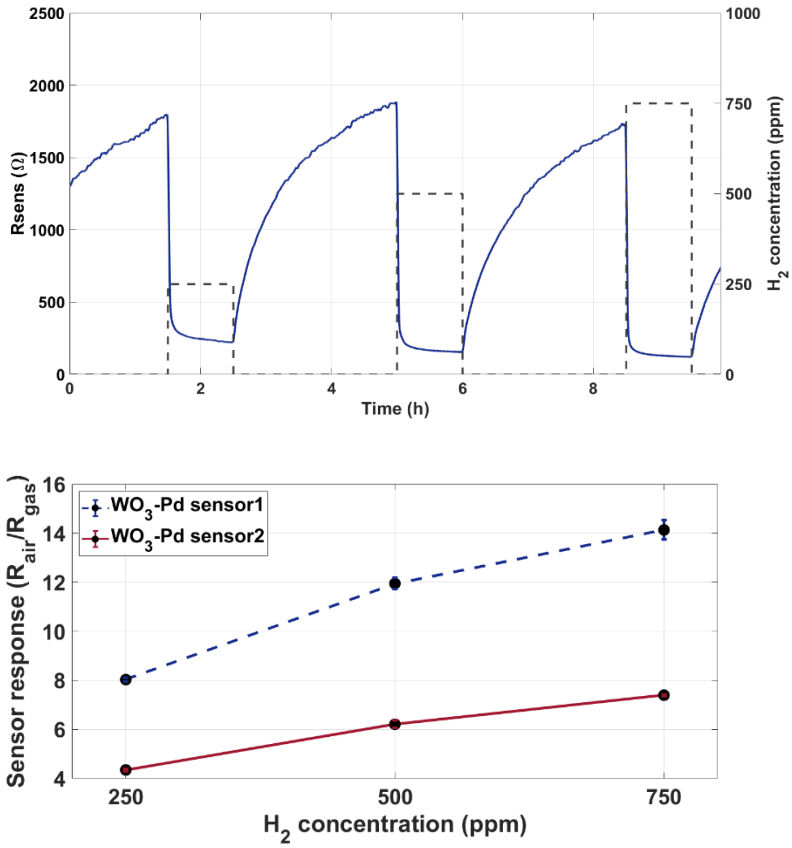


Fig. 3.9 Sensor resistance and responses for a $WO_3$-Pd sensors to three $H_2$ concentrations at 100 °C.

For analysis purposes, we can divide the bending cycle in three stages:

In the first stage, the sensor is in flat position and the electrical resistance of the sensor is $R_0$.

In the second stage, the distance between the grips begins to decrease until the sensor reaches the maximum deformation. The value of the electrical resistance of the sensor is different from $R_0$.

In the third stage, the sensor returns to the flat position. In this point, the electrical resistance of the sensor presents a $\Delta R$.

The maximum deflection (f) due to buckling was between 3.18-3.23 cm, which is equivalent to a curvature radius of 3.35-3.45 mm. This curvature radius is equivalent to an angle of curvature α between 85-90°.

For $WO_3$ sensor 1, first the initial resistance of the sensor $R_0$ was recorded. When the sensor starts to bend, its electrical resistance increased until reaching a maximum value when the sensor was in its maximum deformation. Upon returning to the flat position, the electrical resistance of the sensor decreased until close values to $R_0$ but greater. At the end of the bending test, the electrical resistance of the sensor in flat position ($R_f$) was recorded. It was found a permanent increase (ΔR) of 2.3%.

The same steps of the experiment were followed for the $WO_3$ sensor 2. But the sensor showed a different behavior. After the $10^{th}$ bending cycle upon returning to the flat position, its electrical resistance decreased to values lower than $R_0$. At the end of the bending test, the electrical resistance of the sensor suffered an increase lower than 1%. Fig. 3.10 depicts the values of the electrical resistance of the sensors under maximum deformation and after it returned to the flat position.

The sensing measurements, before and after the bending test, revealed that after the bending test the sensors kept their sensing properties. In both cases, the sensor response after bending decreased. The negative shift between the responses is given by a simple constant and allows a recalibration to the before-bending values as Fig. 3.11 shows.

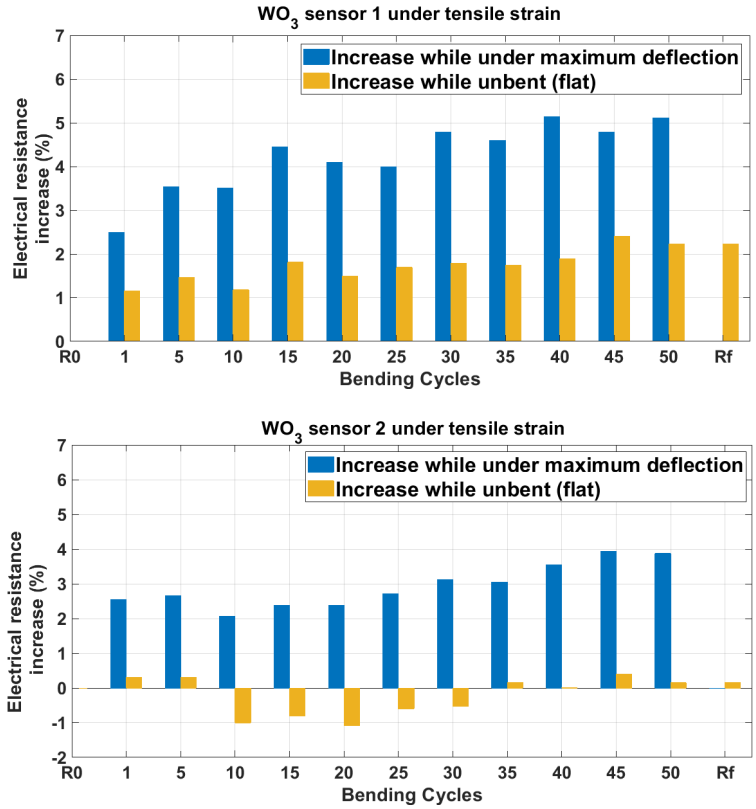


Fig. 3.10 Evolution of $WO_3$ sensors resistance during bending.

The response of sensor 2 after bending showed a bigger shift compared with the response after bending of sensor 1. During the bending test, a noticeable change in the baseline was observed. The sensor was inspected using a magnifying glass as shows Fig. 3.12. The analysis revealed zones in which a detachment of the active layer had occurred. The zones can be found for their silver color. The damage may be due to the presence of adhesive residues from the stencil mask on the tracks, or because the thickness of the conductive tracks was not homogeneous. The lack of homogeneity of the tracks could increase the stress in those areas, causing the detachments.

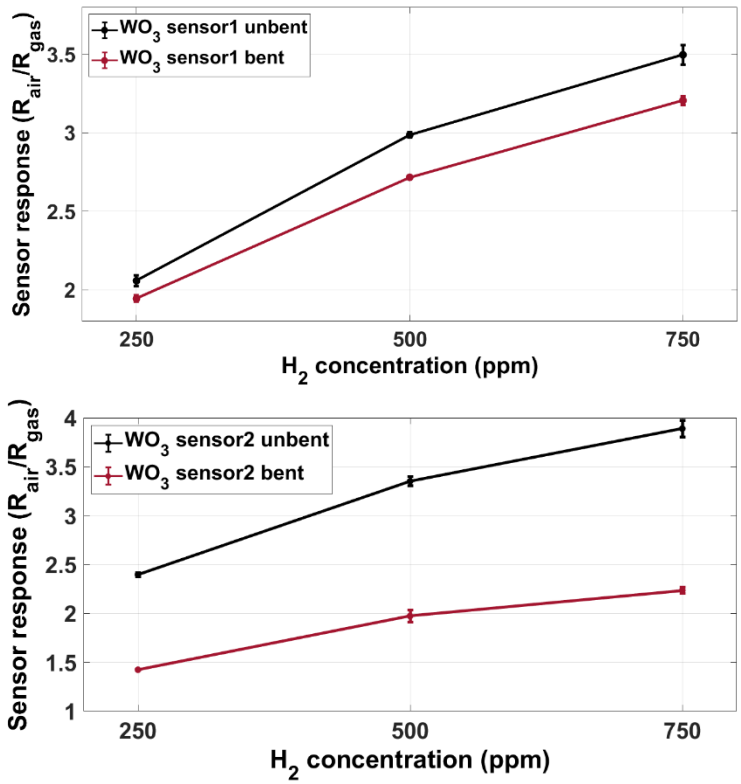


Fig. 3.11 $WO_3$ sensor responses after bending test to three $H_2$ concentrations, at 150 °C.

During the test of $WO_3$-Pd sensors, delamination of some tracks was observed for both samples. The change of the electrical resistance during the test surpassed 1000%. Fig. 3.13 shows the difference between the resistance under maximum deformation and flat position. The observed delamination and the very high increase in electrical resistance were indicative of permanent damage to the sensors. The values of the sensor resistance under maximum deflection indicated that the sensor had track fractures. The gas sensing measurements after bending revealed no changes in the sensor resistance under gas exposure, hence the sensors lost their gas detection capacity.

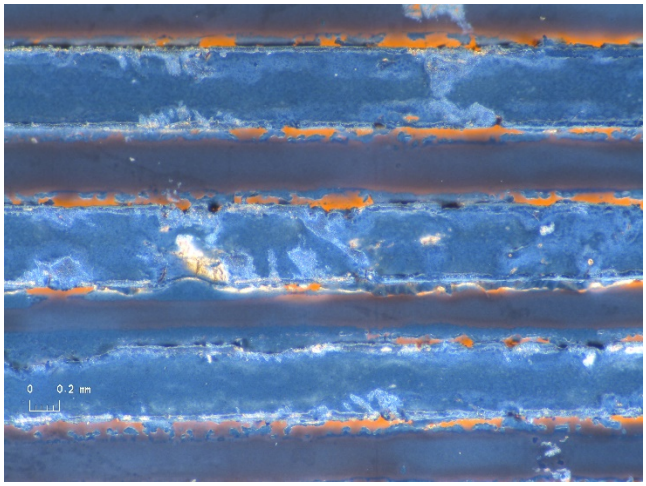


Fig. 3.12 Area of the active layer with detachments.

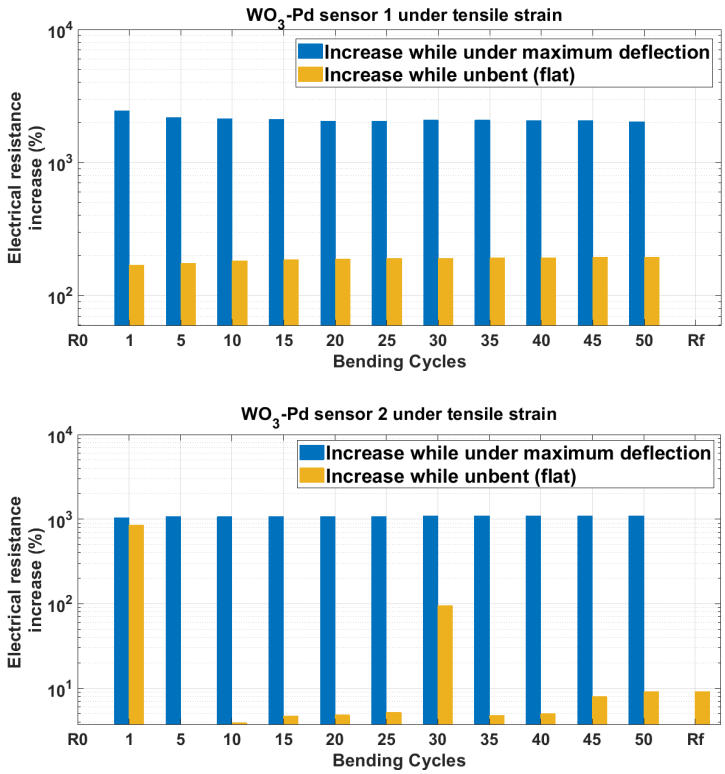


Fig. 3.13 Evolution of $WO_3$-Pd sensors resistance during bending.

# Discussion

This chapter has detailed the fabrication and testing of a flexible gas sensor using a polymeric foil and depositing a $WO_3$ active layer. The conductive tracks were made of silver ink and the active layer was deposited through AA-CVD. Their sensing properties were tested before and after a bending test. To determine the size of the sensor, electrode and heater, the conductive properties of the silver ink were considered. It has been reported that the electrical resistance of conductive tracks diminished after sintering [113,114]. After the AA-CVD deposition, the electrical resistance of the heater decreased by around 50%. Thus, heater dimensions were tailored to endow it with the highest possible room-temperature resistance to overcome the decrease due to the fabrication process. There are two main reasons why a high resistance of the heater is needed. First, to reduce potential errors during the measurements. If the resistance of the heater is measured using the two-wire method, it is possible to add an offset resistance value. Also, if the resistance is too low, more precise equipment is needed. Second, to try to reduce peak currents passing through the connector. That is, not to overpass the current rating of the connector to avoid damaging it and obtaining wrong data. Furthermore, the size of the heater was restricted to the size of the area that can be deposited with the AA-CVD reactor. The final size of the sensor was a tradeoff between the room-temperature resistance of the heater and the covering area of the reactor. Given the area restrictions, and a reliable track gap distance, the heater design had to maximize the aspect ratio ($l/w$) (Eq. 3-2). The reliable gap distance was chosen to avoid short circuits due to the remains of conductive material, thus, reducing the number of samples failed. The electrical resistance of the fabricated heaters at room-temperature was less than 2 Ω.

The gas sensing test for these sensors was performed at only one temperature. It has been reported that the $WO_3$ nanowires can detect gases even at low temperatures [115]. Setting the operating temperature between 100-150 °C had the purpose to obtain sensing responses and to test the reliability of the sensors. Furthermore, these values (100-150 °C) are within the range of temperature tested to obtain the thermal coefficient of resistivity. A higher temperature was not chosen because the relation expressed with Eq. 3-3 stops being linear for a wide range of temperatures, consequently the thermal coefficient of resistivity changes. The operating temperature makes the

conditions of the test harder because the high operating temperature reduces the reliability of the sensors [116]. Furthermore, the silver conductive tracks can suffer swelling, delaminating or cracking [117] that affect their bending resistance. During the bending test, swelling or cracking can give place to early appearing of breakings.

The use of off-the-shelf equipment allows the reproduction of the bending test in other laboratories. The bending tests performed were demanding because when the sensors reached their maximum deflection the angle of curvature was around 85°. The maximum deflection (f) due to buckling was between 3.18-3.23 mm, which is equivalent to a curvature radius of 3.35-3.45 mm.

The sensors showed two distinct behaviors while bent. The case of an increased electrical resistance can be explained for the following conditions:

- Separation between the particles of the silver conductive tracks produce an increase of the resistance.
- Cracks or detachment occurs either on the silver conductive tracks or the active layer.
- A loss of contact between nanowires or between the nanowires and conductive tracks.
- Relocation of the nanowires.

For the case of the decrease of the resistance during bending, the infimum ΔR can be explained for the following conditions:

Considering the non-aligned distribution of the nanowires into the active layer, it is possible that during bending the contact between nanowires was increased. There were more contacts between nanowires. Thus, the electrical resistance of the active layer was decreased.

The phenomenon of the decrease of the electrical resistance during bending has been reported before for carbon fiber reinforced composited [118].

Despite the harsh bending conditions, the permanent change of the electrical resistance was small, and the shape of the sensor response curve

remained without alterations. The permanent increase of the electrical resistance can be explained by loss of the contact between nanowires or nanowires-tracks, detachment of active layer, and relocating of the nanowires. Furthermore the effects of the bending in the conductive tracks can be explained as a relocation of the metal particles, delamination and cracks [119]. After bending test tiny cracks in the conductive tracks were seen, strengthening the latter assumption.

The results of the gas measurements and bending test of this study suggest good reliability of the fabricated flexible gas sensors. Furthermore, the fabrication process only has 3 steps. A decrease in the fabrication steps entails a decrease in the cost of the process.

In the case of the $WO_3$-Pd sensors, the incorporation of palladium to the active layer promote an increase in the sensor responses. The catalytic activity of the palladium contributes to increase the oxidation rate of the active layer. But also, palladium contributes to increase the brittleness of the silver tracks.

# CHAPTER 4
# Flexible Gas Sensor Fabricated by AA-CVD using Inkjet-Printed Au Electrodes

# Flexible Gas Sensors Fabricated by AA-CVD using Inkjet-Printed Au Electrodes.

## Introduction

Printing technologies have made easier the integration of flexible substrates to the electronics because their temperatures of deposition are compatible with the working temperatures of flexible substrates. Printing technologies, as inkjet printing, reduce material waste, simplify the fabrication and the patterning process. Also, employing inkjet printing, very thin layers can be obtained from solution-based materials.

This chapter explains how the inkjet printing technique was used to fabricate electrodes over a flexible substrate. Since the deposition of tungsten trioxide nanowires over Kapton has been already proved, this chapter presents the functionalization of $WO_3$ nanowires with palladium. The deposition technique used was AA-CVD.

The functionalization of nanowires with other metals increases their sensing properties. Palladium, platinum, copper, and silver nanoparticles can act as catalysts of the reaction between the active layer and the target gas. Moreover, the functionalization of the nanowires could lower the sensor operating temperature [120].

The sensors fabricated comprise:

- A flexible substrate, Kapton with 50 µm thickness.
- Electrode and heater made of conductive gold ink.
- Active layer of tungsten trioxide nanowires functionalized with palladium.

The endurance to bending of the fabricated sensors was studied. The study included three stages:

- Gas sensing test.

- Bending test.
- Gas sensing test.

# Sensors Fabrication

## Conductive Tracks

The electrode and heater tracks were fabricated through inkjet printing. The printing process requires three previous steps: design of the pattern, substrate preparation, and adjusting printing parameters.

**Substrate Preparation**

Prior to the inkjet deposition the Kapton substrates were cleaned. The pieces were immersed in acetone (*Scharlau, 99.5%*) for 5 minutes, then in ethanol (*Sigma-Aldrich, 96%*) for another 5 minutes. Finally, they were rinsed with deionized water and dried in an oven at 110 °C for 10 min.

After cleaning, the substrate was subjected to a surface treatment of oxygen plasma. Through controlling the conditions of plasma treatment, the surface properties of the polymers, such as wettability and adhesion, can be altered [121]. The main purpose of oxygen plasma treatment was to improve the hydrophilicity of the substrate. It is well known that droplets deposited over a hydrophobic substrate behave as if supported by a thin layer of air [122]. Hence, an improve of the substrate hydrophilicity means that the fluids will spread over a larger area on the substrate. For printing purposes, this will help to prevent that the droplets slide over the substrate surface and to modulate their size on the substrate. Also, the adhesion can be changed. The physical parameter used to measure hydrophobicity or hydrophilicity of a surface is the contact angle of a water drop deposited on the surface of the substrate. Thus, contact angle measurements were conducted to evaluate the hydrophilicity of the substrate after oxygen plasma treatment. For water, surfaces that allow contact angles between 90-120° are referred to as hydrophobic, while surfaces with contact angles below 90° are referred to as hydrophilic.

For contact angle measurements, clean pieces of Kapton were treated using a low-pressure radiofrequency (RF) plasma chamber (*Nano, Diener Electronic, Germany*) under oxygen flow. Plasma powers from 5 to 20 W were

applied for 30 seconds under a pressure of 0.3 mbar. Afterwards, static contact angle measurements were performed using an optical tensiometer (*Theta Lite TL100, Biolin Scientific*). Deionized water was used as test liquid. The contact angle measurements were replicated three times, and the average contact angles were calculated. Fig. 4.1 shows the mean contact angles obtained for each applied plasma power. The contact angle on untreated Kapton was 69°.The contact angle decreased after plasma treatment with powers between 5 and 15 W. While for the plasma treatment of 20 W, the contact angle did not decrease further. Fig. 4.2 shows the droplet images for the plasma powers applied.

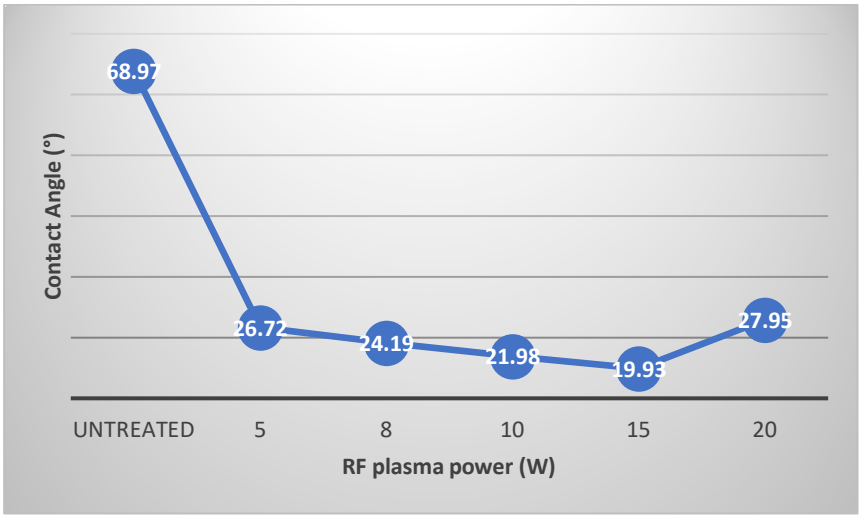


Fig. 4.1 Contact angles measured for different plasma powers.

The contact angle measurements proved that it is possible to control the size of the droplets jetted onto the substrate varying the power of oxygen plasma treatment. Due to the lack of a proper picoliter dispenser accessory for the optical tensiometer, it was not possible to measure the contact angle of the gold ink over plasma treated Kapton. Therefore, the adequate power for oxygen plasma treatment was obtained empirically by measuring the size of the droplets deposited by inkjet-printing over plasma treated Kapton at different powers. Moreover, an estimation of the contact angle for the gold ink can be done according to Keller and Stüwe [123]. Keller and Stüwe used a simple model to provide a theoretical prediction of drop diameters for different drop volumes and contact angles.

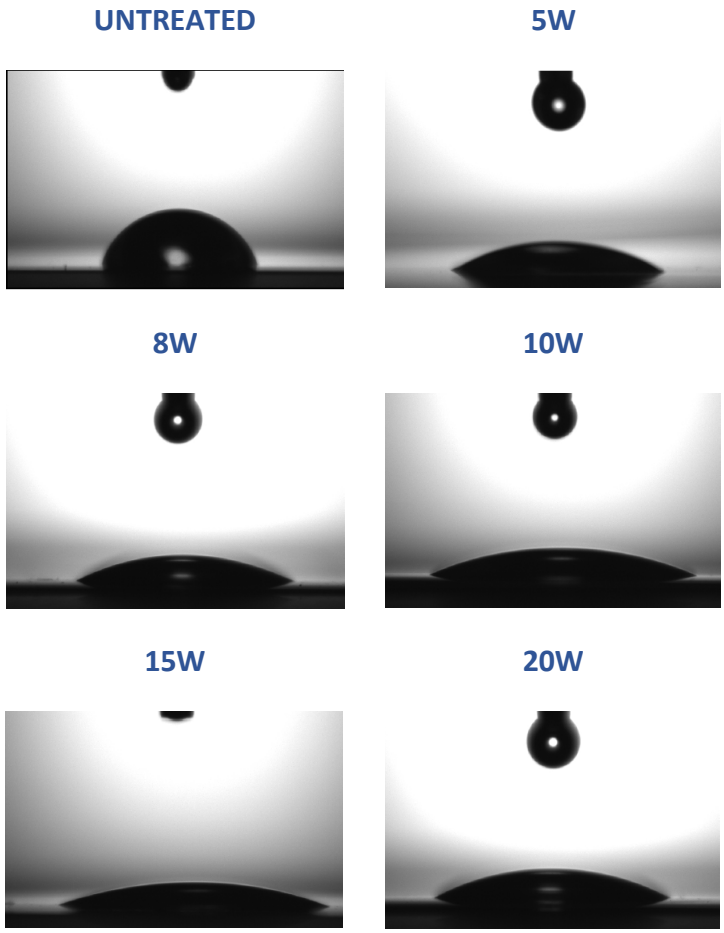


Fig. 4.2 Droplet images on Kapton for the plasma conditions tested.

The droplet size is affected by the plasma treatment of the Kapton surface. For instance, a droplet size of around 170-190 µm was obtained when a plasma treatment of 30 W was applied. For a plasma power of 20 W, the droplet size obtained was 190-200 µm. According to Keller's calculations, this droplet size coincides with a contact angle around 20°. As the droplet size showed less variation at a plasma power of 20 W, this plasma power was chosen to treat the Kapton. So, the oxygen plasma conditions for inkjet printing were 2 min at 20 W. Then, the printing conditions were adjusted accordingly.

**Adjusting Printing Parameters**

For the inkjet printing process, a drop-on-demand piezoelectric material printer Dimatix DMP-2850 was used (*Fujifilm Dimatix Inc., Santa Clara, CA, USA*), equipped with a cartridge of 10 pl drop volume (*DMC-11610*). The cartridge includes the piezo-driven jetting device, an ink reservoir, a heater, and 16 nozzles. The diameter of each nozzle is 21 µm. The cartridge is made of polypropylene and is chemically compatible with aliphatic hydrocarbons, aromatic hydrocarbons, aliphatic alcohols, ketones, ethers, acrylates, glycols, lactate esters, and cellusolves. Additionally, it is compatible with water-based fluids.

The ideal fluid characteristics that can be jetted, according to the manufacturer [124], are:

- Viscosity: 10 -12 cP at jetting temperature
- Surface Tension: 28-42 dynes·cm$^{-1}$ at jetting temperature
- Low Volatility: Boiling points higher than 100 °C are preferred.
- Density: Specific gravity greater than 1 is beneficial.
- Acidity or Alkalinity: A pH value between 4 and 9 is recommended.

Before filling a cartridge with the fluid, it is recommended to remove any large aggregates or particles by filtering. The particles in the fluid should be 1/100$^{th}$ the size of the nozzle. The substrate is placed over the platen, which has holes to hold the substrate by vacuum. Furthermore, it is possible to heat the platen to increase the temperature of the substrate, promoting the evaporation of the ink solvents.

The jetting process is controlled by pulses of voltage applied to the piezo-electric printhead. The shape of the voltage pulses and their duration is known as waveform. The typical jetting waveform is divided into segments. Each segment controls duration, level, and slew rate. Duration is the pulse duration time in µs. Level is the percentage of voltage applied. The voltage is related to the drop volume, furthermore, the drop velocity is a function of voltage. The velocity and rate of change of voltage directly affect the volume of the drop. That

is, faster changes in voltage change the drop volume faster, and bigger changes in voltage cause bigger drop volume changes. The voltage rate of change is expressed by the slew rate. Figure 4.3 shows a typical waveform.

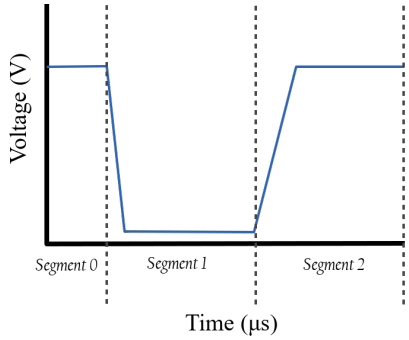


Fig. 4.3 Basic waveform divided into segments.

For the sake of clarity, it was added a segment 0 to the waveform. This segment is connected to the last segment of the waveform and its helpful to understand the cyclic conditions of the waveform. A voltage is applied to the piezo-electric printhead; thus, the piezo-element is deflected, and the fluid chamber is depressed.

In the segment 1, the voltage is decreased to zero and the piezo-element moves upward changing to a neutral straight position. The chamber reaches its maximum volume. Shortening the pulse width will decrease drop volume. Fluids with higher densities need longer pulses.

In the segment 2, the voltage is increased, and the piezo-element is deflected again. The chamber is compressed, and the drop formation is started. The slew rate in this segment controls the jetting velocity of the drops. Higher slew rates increase jetting velocity. Lowering the voltage will decrease the drop volume.

The adjustment of the waveform begins by increasing the voltage to apply until the drops are ejected. The duration of the pulse is the next parameter to adjust. If the jetting is sustainable and the drop is straight down for at least 60 seconds, the parameters have been adjusted correctly. Afterwards, the voltage applied to each nozzle is adjusted.

For fluids with higher viscosities, increasing the nozzle temperature can help to reduce their viscosity. Also, increasing the platen temperature helps to the droplet pinning.

An adequate adjustment of the printing parameters, such as the waveform, cartridge temperature, platen temperature, etc., will achieve an efficient jetting. The drop ejection should avoid the formation of secondary droplets, called satellites, that can be deposited around the main droplet.

In this work a commercially available gold nanoparticle ink was used (*NPG-J, Harima Chemicals Inc., Japan*). The ink has a dynamic viscosity of 9.3 cP, its metal content is 56.3 wt%, and it has a particle size of 7 nm. The vendor provided these parameters.

For inkjet printing with the gold ink, first, it was stirred in an ultrasonic bath for 5 min at room temperature, to achieve a good dispersion. Then, the cartridge was filled.

Given the high price of the gold ink and considering that the filtering step will consume ink, it was decided not to filter the ink before filling the cartridge, although the nozzles could clog. For the printing tasks, only one of the sixteen nozzles of the cartridge was used. In case of clogging, another nozzle could be chosen.

The printer parameters were adjusted for the ink using the Dimatix Drop Manager software. Table 4-1 gives the parameters selected for inkjet printing. Only one nozzle was selected to print. The parameters were carefully selected to avoid satellites during printing.

| Printing parameters for gold ink | |
|---|---|
| **Cartridge temperature** | 42 °C |
| **Firing Voltage** | 22.20 V |
| **Platen temperature** | 40 °C |
| **Meniscus Vacuum** | 4.0 in $H_2O$ |
| **Jetting Frequency** | 4 kHz |

Table 4-1 Cartridge parameters

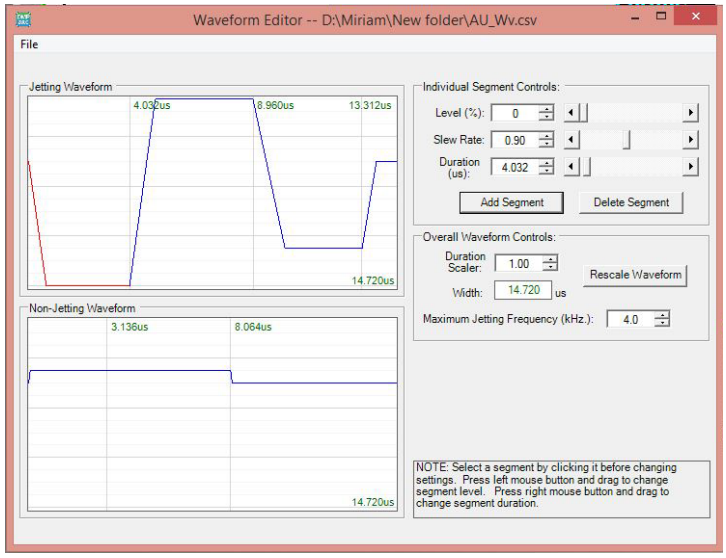


Fig. 4.4 Shape of the waveform used to print gold ink.

A short line was printed to measure the droplet size. For the parameters selected, droplets had a size of 200 µm. Once the drop size is known, the pattern can be tailored to obtain the desired dimensions.

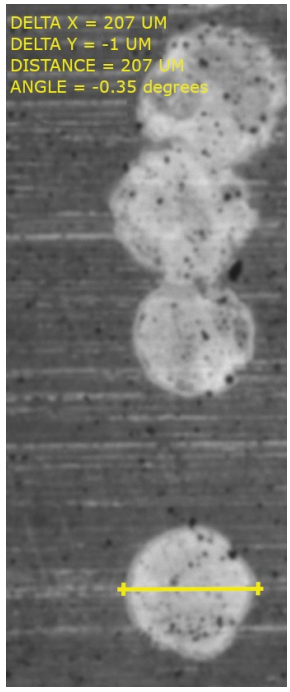


Fig. 4.5 Test line and drop size.

**Pattern Designing**

As in the earlier chapter, the chosen geometry for the electrodes included one heater and one coplanar electrode. In this work, the geometry was simplified, aiming to achieve high printing yield. Fig. 4.6 illustrates the design of the geometry. For pattern design, the inkjet printer Dimatix 2850 allows to use the proprietary pattern editor of Dimatix Drop Manager or to import monochrome bitmap images (**.BMP*). In this work, the patterns were imported to Dimatix Drop Manager software as monochrome bitmap images. The patterning of the geometry was done using open-source computer graphics software (*GIMP 2.8*). In the monochrome images created a black pixel is considered as a drop and a white pixel a non-printing space.

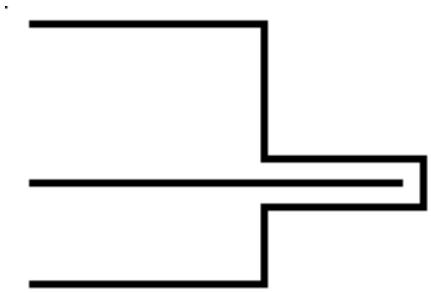

Fig. 4.6 Design of one electrode with a coplanar heater for inkjet printing.

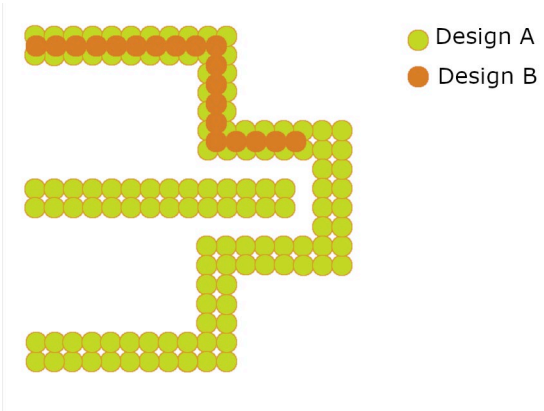


Fig. 4.7 Schematic representation of design B being printed over design A.

The initial design, Fig 4.6, was divided into two designs to increase the printed yield, and to ensure the conductivity of the tracks. Fig. 4.7 shows both designs. It is worth noting that the designs are in the orientation in which they were printed and have alignment marks in their four corners.

In design A, the design is formed by two lines of droplets that draw the transducer design. Both lines of pixels are separated by a white pixel. While design B is a single line in which the black pixels are separated by one white pixel. The followed approach was to print the design A with droplets overlapping and then print the design B to ensure good coverage of the ink, instead of just printing a certain number of layers the design A.

Fig. 4.8 depicts the result of print design A once. Through Dimatix Drop Manager software, it is possible to vary the distance between the center of the droplets in X and Y position, drop-spacing, producing a droplet overlapping and changing the width of the printed lines. The drops were overlapping 20 µm, and there were some holes in the middle part of the tracks. Also, Fig 4.8 shows droplets with varied sizes; this dissimilarity on the size could be attributed to defects in the surface substrate.

Fig. 4.9 shows the result of printing design B over design A. The design B was printed to the center of the design A, covering areas that were not covered with design A.

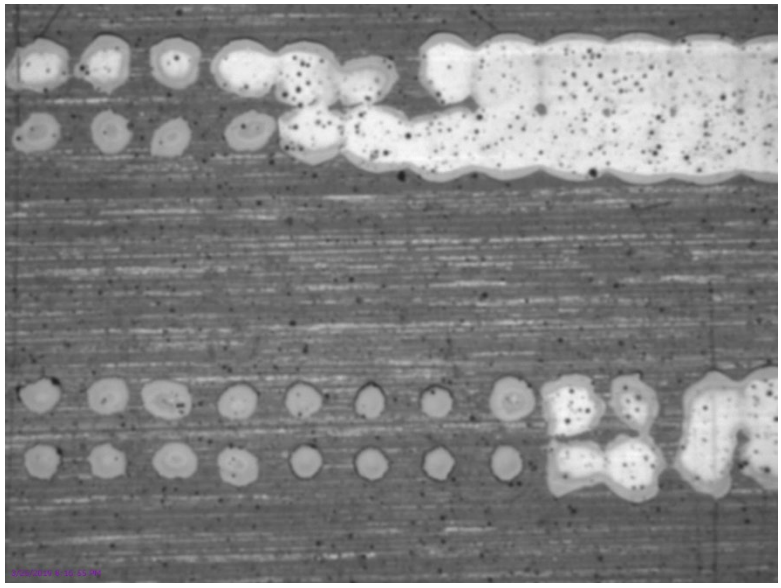

a) Surface defects causing variation in the droplet size

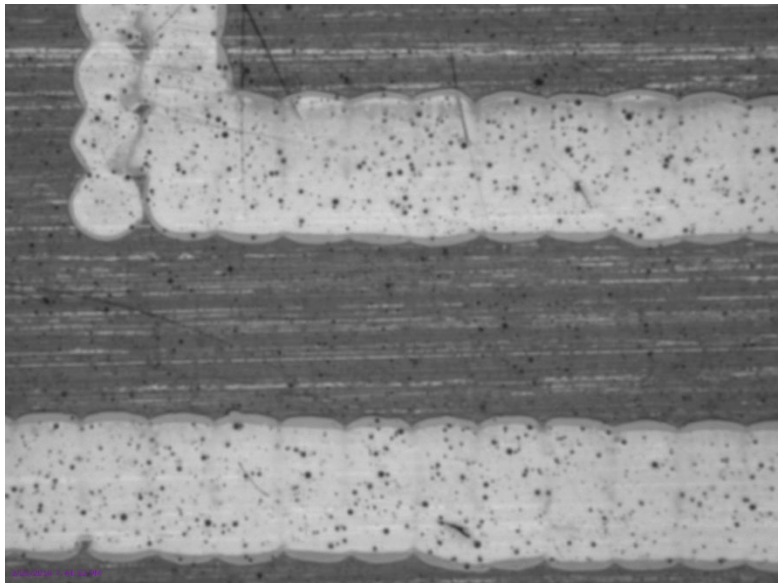

b) A layer of design A uniformly printed

Fig. 4.8 Design A printed once.

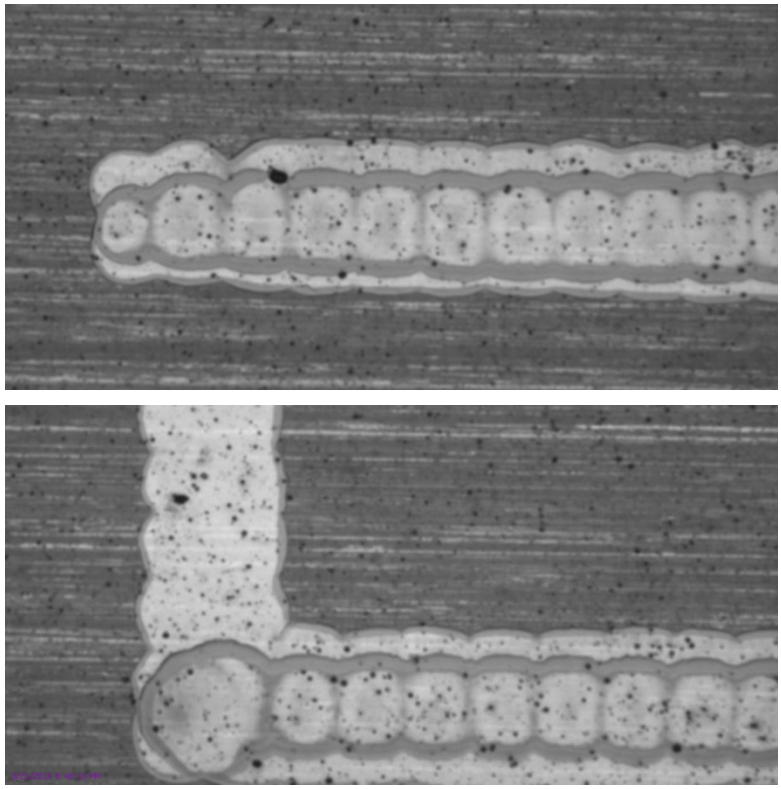

Fig. 4.9 Design B printed over Design A.

The alignment marks were an element of paramount importance to enable printing the next layers. By setting the alignment marks as the print start position, it is possible to align the substrate or previously printed layers to print a new layer.

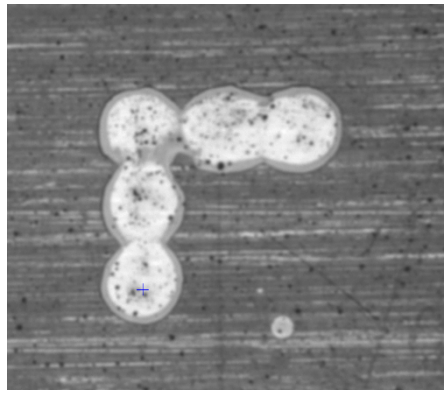

Fig. 4.10 An alignment mark.

The electrode design was printed with a drop-spacing of 80 µm. Two layers of each design were successively printed. The ink was sintered at 250 °C for 3 hr. The obtained inkjet-printed electrodes have a size of 18 mm x 15 mm. The track width is of 380 µm and the gap between electrodes is 320 µm. After the electrodes are sintered, they are ready, and an active layer can be deposited over them to fabricate a sensor.

## Metal Oxide Deposition

The gas sensitive material chosen was a functionalized metal oxide, $WO_3$ nanowires functionalized with palladium. A one-step deposition method was followed to functionalize $WO_3$ nanowires. The goals were to avoid subject the substrates to excessive thermal stress and reduce the number of fabrication steps.

A precursor solution was prepared, having 50 mg of tungsten hexacarbonyl (*$W(CO)_6$, Sigma-Aldrich*) and 1.5 mg of palladium (II) acetylacetonate (*$Pd(C_5H_7O_2)_2$, Sigma-Aldrich*) dissolved in acetone (15 ml) and methanol (5 ml).

The deposition process was carried out as described in the previous chapter. Although palladium can improve the sensing response of the sensor, it is still necessary to heat the active layer for gas detection.

Fig. 4.11 AA-CVD deposition steps.

## Heater Calibration

As mentioned above the heater was made of gold ink. The increase of the temperature on the heater can be calculated using Eq. 3-3. Thus, it was necessary to obtain the temperature coefficient of resistivity (TCR) of the gold tracks. The TCR was obtained empirically. For this purpose, a sample was placed inside an oven to measure the electrical resistance of the tracks for a temperature range between 25 and 200 °C. The electrical resistance was measured using the 4-wire mode of a digital multimeter (*HP34401A, Keysight Technologies*).

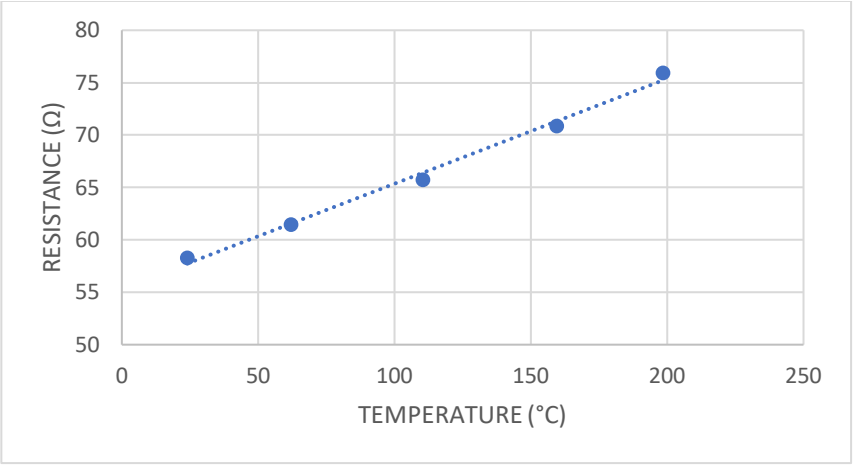


Fig. 4.12 Linear behavior of the resistance vs temperature relationship for the gold conductive tracks.

## Setup for Gas Sensing

The gas measurements were performed using the setup explained in the previous chapter. The application that controls the acquisition equipment and the power supply was modified to the gold ink parameters. The value for the TCR (α) obtained from the heater calibration was changed. The gas measured was hydrogen, and the concentrations were 100, 200, and 300 ppm. Gas measurements were carried out twice, before and after a bending test.

## Bending Test Setup

The bending test were performed using the setup explained in Chapter 3. The stroke was changed according to the size of the sensors to produce a comparable deformation concerning the work described in Chapter 3. The sensors fabricated using inkjet-printed electrodes were smaller than the sensors tested in the Chapter 3. Thus, the stroke was set at 1 mm, the velocity at 20 mm/min in tensile strain. Sensors were bent 50 cycles under these conditions. The electrical resistance of the sensors was acquired during the entire bending test.

## Results

The stages 1 and 3 of the experiment were carried out under the same parameters. The operating temperature was 100 °C. The sensor response was calculated $R=R_a/R_g$, where $R_a$ and $R_g$ are the resistance of the sensor in synthetic air and when the target gas is present, respectively.

The comparison of the sensor responses before and after the bending test showed that the sensor kept its gas sensing properties. The response behavior only suffered a positive shift after the bending process opposed to the results described in the Chapter 3.

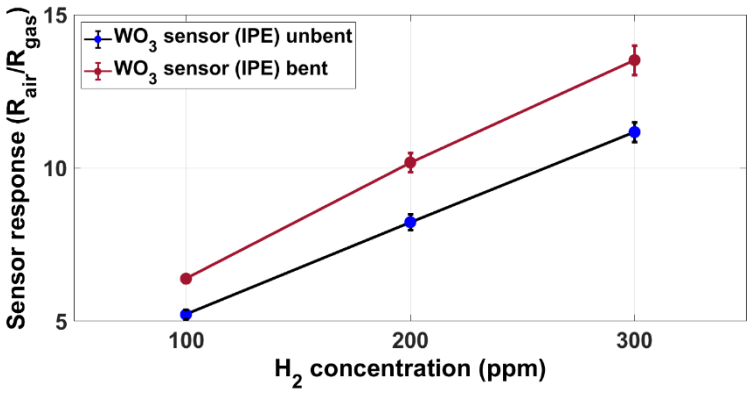


Fig. 4.13 Sensor responses before and after bending.

During the bending test, the behavior of the electrical resistance of the sensor showed positive increases. The electrical resistance reached a maximum value when the sensor was at its maximum deformation. When the sensor returned to the flat position the electrical resistance showed a positive increase with respect to $R_0$. During the test there were no observed detachments from the active layer or tracks. The sensor was bent 50 cycles. The maximum deflection (f) due to buckling was 1.47 mm, producing a radius of curvature of approximately 1.45 mm (angle of curvature around 90°). The electrical resistance of the sensor had a permanent increase of 10%. The resistance value was gradually increasing with the increase in the bending cycles, as can be seen in Fig. 4. 14.

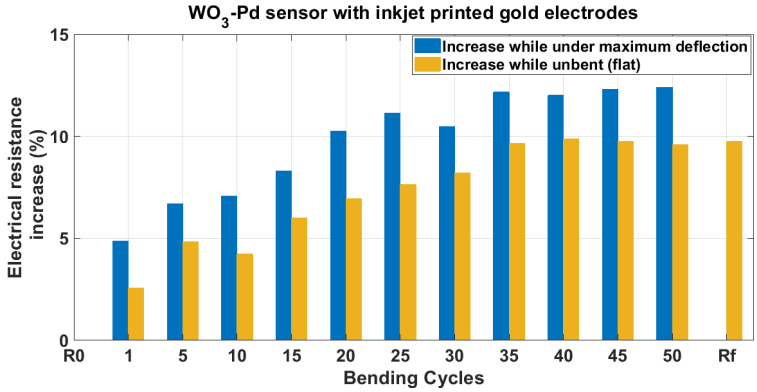


Fig. 4.14 Evolution of the sensor resistance during the bending test.

## Discussion

In this chapter, the obtention of electrodes over Kapton through inkjet printing was explained. Conductive tracks were made of conductive gold ink while the active layer was $WO_3$ nanowires functionalized with Pd. A bending test was performed to study the endurance of the fabricated sensor. During the bending test, the electrical resistance of the sensor was continuously measured in situ. Gas measurements were carried out before and after the bending test, to evaluate the bending effects on gas detection.

During the printing process, and despite the oxygen plasma applied to improve the surface conditions of the Kapton, it was possible to find defects on the substrate surface. For adjusting the printing parameters, and despite the low viscosity of the ink, it was necessary to heat the cartridge to obtain satisfactory results. Also, the platen temperature was raised to allow the pinning of the droplets to the substrate and promote partial drying. The platen temperature was the same as the cartridge temperature because, after long printing times, the cartridge gets heated by the platen, and the increase of temperature changes the viscosity of the ink, changing the overall printing conditions. Lower platen temperatures avoid the solvent evaporation, creating thicker layers of material that can swell during the sintering. The swelling gives place to crack formation.

Continuous monitoring of the sensor resistance during the bending test helps to describe the behavior of the nanowires layer during the bending test. When the sensor was in its maximum deflection, the resistance showed a value higher than when it was in flat position. This behavior was kept throughout the bending test. As the number of cycles increased, the value of the resistance in flat position also increased. At the last fifteen cycles of the bending test, the resistance changes from the maximum deflection to the flat position were the same. As if the resistance changes due to bending will reach a steady state. Once the bending test was finished, the resistance of the sensor in flat position did not change.

The gas measurements carried out before and after the bending test show that the shape of the sensing response curve was not changed. The sensing response increased after the bending test. This can be explained by the separation or relocation of the nanowires during the bending test. A separation between the nanowires explains the increase of the resistance of the active layer. The separation or relocation diminishes the contact areas between nanowires, in turn “releases” the surface to occur the gas adsorption. Thus, the increased surface contact between the gas molecules and the nanowires increases the sensing response.

# CHAPTER 5
# Flexible ZnO Sensors Fabricated by Screen Printing

# Flexible ZnO Sensors Fabricated by Screen Printing.

## Introduction

This chapter describes the fabrication of metal oxide gas sensors using the screen printing technique. The sensors were fabricated over a polymeric foil (Kapton™). The fabricated sensors comprise:

- A flexible substrate, Kapton® 50.8 µm thick.
- A heater made of conductive silver ink
- Interdigitated electrodes (IDE) made of conductive silver ink
- Active layer of zinc oxide

The whole work presented in this chapter was accomplished in the Smart Materials department of the Centre for Nanotechnology and Smart Materials (CeNTI) in Portugal. The technologies and materials available in the center delimited the sensor conception and testing.

## Sensors Fabrication

### Heater

For the fabrication of the sensors, screen printing frames already patterned were used. The available screen printing frames only had the IDE pattern whereby the heater should be deposited in a different step and using a different technique.

For the design of the sensor, two alternative locations were considered to place the heater. First, it was considered to place the heater on the reverse of the IDE but this would have produced damage on the deposited elements or defects on the next elements to deposit. Then, the possibility to place the heater coplanar to the IDE was studied to avoid intrinsic defects in the sensor elements. To deposit the heater at the end would imply to damage the previous elements. On the other hand, to deposit the heater first would not have posterior damages

to the other sensor elements. It was decided then to place the heater coplanar to the IDE and deposit it first to avoid damaging the other sensor components. This, despite the high-power consumption of using a coplanar heater to heat the active layer due to the low thermal conductivity of the Kapton.

The deposition of the heater pattern was done through a mask of vinyl (70 µm thick) which was the negative of the image to be printed. The heater was drawn using open-source computer graphics software (*InkScape 0.92*). Then, the design was cut using a vinyl cutter plotter (*CAMM-1 GS-24, Roland DG*). The Fig. 5.1 illustrates in blue color the areas corresponding to the design of the heater, which is surrounding the IDE.

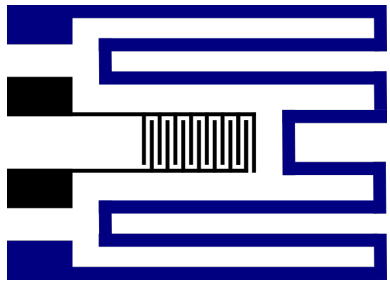

Fig. 5.1 Sketch of the heater surrounding the interdigitated electrodes.

Then the vinyl masks were transferred to the Kapton and the area corresponding to the heater was removed. The ink selected for the fabrication of the heater was DuPont™ 5025 silver conductor. For the deposition, the ink was spread through the mask using a printing squeegee. The ink was dried in a convection oven at 120 °C for 20 minutes. Finally, the mask of vinyl was removed. The ink 5025 silver conductor was chosen because the first attempts to fabricate heaters were done using ink KA801 (*DuPont™ Kapton™ KA801 Polyimide silver conductor*) and showed that the chemical composition of the ink began to deform the vinyl mask within the first 10 minutes after the deposition. Deformation caused narrowing of the tracks, and this would produce either hot spots when operating the heater or a fracture of the tracks.

## Electrodes

In screen printing deposition, inks are deposited through a patterned screen. The screen is a finely woven mesh of stainless steel mounted under tension on a metal frame. The inks have the materials to obtain the active layer or conductive tracks. Interdigitated electrodes were fabricated using a semi-automatic flatbed screen printing machine. The mesh used was a stainless-steel mesh 90-40Y. The ink used was a commercially available silver ink (*DuPont™ Kapton™ KA801*). The electrodes were 10-finger interdigitated with an area of 22 x 4 $mm^2$ as Fig. 5.1 illustrates. The width of the fingers and their gap are 300 µm. The IDE were deposited on Kapton substrate with the heater previously deposited. After printing, the samples were dried on an oven at 120 °C for 20 min.

## Active Layer

The metal oxide used for the active layer was zinc oxide (ZnO). ZnO is a n-type semiconductor with a wide bandgap (3.37 eV). It is widely used in various applications such as photodetectors, piezoelectric devices, solar cells, transistors, transparent electrodes, and gas sensors [125–128]. ZnO inks were formulated to deposit an active layer by screen printing. The principal ink characteristics required were:

- Viscosity of 0.1 to 10 Pa·s [1]**;**
- Slow drying;
- Good adhesion to the substrate after drying.

High viscosity and slow drying time are essential properties to screen printing inks. A less viscous ink will spread over the screen and substrate and, in the most extreme case, drip from the screen-mesh to the substrate. This will result in printing a distorted pattern. On the other hand, spreading a more viscous ink becomes more difficulty, obtaining a non-uniform layer. In this case, it is possible to see the mesh pattern on the deposited layer. Furthermore, it must be avoided that the ink deposited over the substrate returns to the screen by capillarity. This effect could produce holes or thickness differences on the layer. Moreover, the ink should conserve its properties during the printing

process under lab conditions. For this reason, inks or pastes for screen printing need solvents with high boiling points. If the ink dries over the screen, it can obstruct the mesh and produce a low-quality printing. Once the ink is properly screen-printed and dried, the ink must show good adhesion to the substrate. Good adhesion is needed because the layer deposited over the flexible substrate will be under mechanical stresses and must withstand them without showing detachments.

Finally, as it is intended to fabricate a chemoresistive gas sensor, the electrical resistance plays a key role in the working principle of it. ZnO shows an n-type behavior, which means that when it is exposed to oxidizing gases, its electrical resistance increases, on the other hand, when it is exposed to reducing gases, its electrical resistance decreases. During gas measurements, the value of the electrical resistance should change within a range of measurable values in many types of equipment, to facilitate future experiments or applications.

According to Cano-Raya et al. [129] the main components of solid metal-based inks are:

- The solid metal particles, MP (or their precursors) that will act as conductive fillers;
- The polymers as dispersing/capping agents that will ensure the binding of the printed ink to the substrate;
- The carrier solvents that will dissolve/swell up polymers; and
- Other additives to enhance or change the properties of the resultant ink

In our formulations the solid metal particles were zinc oxide particles in powder (*Zinc oxide nanopowder, <100 nm particle size*, *Sigma-Aldrich*). The chosen dispersing agent was ethyl cellulose (*EC, 48% ethoxyl, Sigma-Aldrich*). The ethyl cellulose is a polymer widely used in printing inks, has shown good folding-endurance, and it is permeable to certain gases. [130]. Therefore, it would not prevent the interaction between the target gas and the zinc oxide particles. The ethyl cellulose is soluble in ethanol, toluene, acetone, butanol, xylene, and in a mixture of the previous solvents. The chosen solvent for the dispersing agent should be compatible with the solvent used to dissolve the

metal particles. Then, various solutions were prepared with different pairs of solvents, zinc oxide particles, and ethyl cellulose. The solvents tested were selected considering their high boiling point, their viscosity, and their compatibility with the dispersing agent. From the previous solvents, ethanol and acetone are the safest, from which ethanol has a higher boiling point and viscosity.

To prepare the solutions, first, the dispersing agent was mixed in the selected solvent and stirred for 1 hour to hydrate the cellulose and avoid aggregates. After that, zinc oxide particles were mixed with the selected solvent and sonicated until elimination of the aggregates. Finally, the solution with the dispersing was added into the zinc oxide solution and stirred. The solutions prepared were overnighted to evaluate the miscibility of all the components and eliminate the air entrapped during the mixing steps. Finally, the solutions were deposited over PET and Kapton, using a film applicator gauge of 300 µm. The Kapton substrates employed had silver IDE that was deposited previously. PET was used to facilitate the evaluation of the layer homogeneity by visual inspection thanks to its transparency, looking for defects such as clusters of material, pits or craters, off-color, etc. The table 5-1 details the composition of the different solutions prepared and gives a summary of their characteristics.

| # | Solvent for dispersing agent | Dispersing agent solution ($mg/cm^3$) | Solvent for Zinc Oxide | ZnO per dispersing solution ($g/cm^3$) | Observations |
|---|---|---|---|---|---|
| **1** | Ethylene glycol | 75 | Terpineol | 0.05 | After overnighting, the dispersing solution separated from ZnO solution. |
| **2** | Ethanol | 75 | Terpineol | 0.05 | The obtained layer was homogeneous but the electrical resistance, measured from the contacts of IDE, was higher than 600 MΩ (OVLD) even when the sample was at 100 °C. |
| **3** | Ethanol | 75 | Ethanol | 0.05 | Dried fast and presented formation of aggregates. |
| **4** | Ethanol | 75 | Water | 0.05 | The final layer had poor adherence. Detachments occurred easily due to manipulation. |
| **5** | Ethanol | 75 | Terpineol | 0.1 | The layer was homogeneous. After drying, it had a resistance of 20 -30 MΩ when the layer was heated at 100 °C. |
| **6** | Ethanol | 75 | Terpineol | 0.2 | The layer was homogeneous. The obtained solution was too viscous for a screen-printing process. |
| **7** | Ethanol | 30 | Terpineol | 0.2 | After the layer dried, it presented aggregates |
| **8** | Ethanol | 30 | Terpineol | 0.1 | The layer was homogeneous. After drying, it had a resistance of 10 MΩ when the layer was at room temperature. |

Table 5-1 Zinc oxide inks composition.

Preliminarily, three compositions were tested to evaluate their performance during the screen printing deposition. The compositions tested were numbers 5, 6, and 8. Composition number 6 resulted too viscous for a screen printing deposition. It was possible to observe, in the deposited layer, the pattern of the screen mesh. Furthermore, during the test, the screen mesh got obstructed constantly by the ink.

On the other hand, the layers obtained from the other compositions, numbers 5 and 8, had a homogenous aspect. Composition number 5 had a viscosity of 18.24 Pa·s, while composition number 8 has a viscosity of 4.6 Pa·s. These compositions were chosen to be deposited by screen printing. For the sake of clarity and from now on, the mixture number 5 will be called ink A, and the number 8 ink B. The inks were deposited by screen printing under the same conditions used for the electrodes. After printing, the ink was dried at 110 °C for 30 min. Subsequently, the samples were annealed at 150 °C for 30 min.

The active layer was observed using an Environmental Scanning Electron Microscope (E-SEM). In the case of ink A, the E-SEM images revealed a layer with protruding clusters of material. These clusters could arise due to the coalescence effect of the metal nanoparticles during the annealing step.

While for ink B, the presence of clusters in the layer is lower, but it has pits distributed over the entire layer area. The presence of pits can be explained by the orange peel defect that appears on painted surfaces. The orange peel effect arises when the ink or paint does not flow-out properly across the surface. However, more factors contribute to the orange peel effect, such as paint formulation, solvent blend, solvent content, application parameters, cure conditions, etc. [131–133]. Ink B was less viscous than ink A, it could flow-out easily over the surface, discarding the viscosity as the cause. The application parameters and cure conditions were the same for both inks. Hence, the orange peel effect is attributed to the high solvent content of composition and its fast evaporation during the print and dry steps.

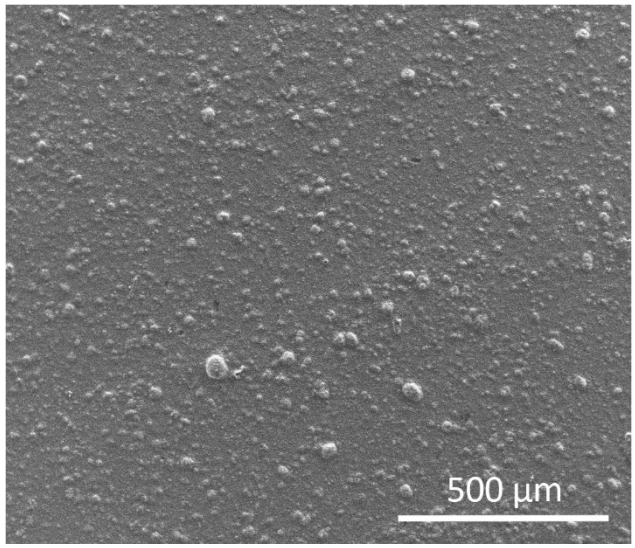


Ink A

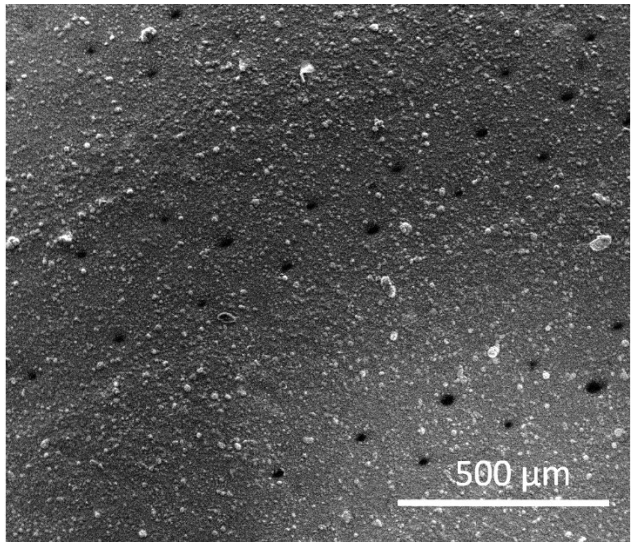


Ink B

Fig. 5.2 E-SEM images of the zinc oxide active layer deposited by screen printing.

Before the gas sensing test, it was necessary to characterize the heater to relate its voltage and current values with the temperature of the active layer.

## Heater Calibration

Owing to the coplanar configuration of the heater with respect to the active layer, the heater characterization was focused into estimating the heater conditions needed to rise the temperature of the active layer.

As a first step, the temperature coefficient of resistivity (TCR) of the silver tracks was obtained experimentally. The heater was placed inside an oven and was heated at temperatures between 50 and 150 °C. The electrical resistance of the heater for each temperature was measured and used to calculate the TCR. The values obtained showed the linear increase of the heater resistance as function of the temperature as the Fig. 5.3 illustrates.

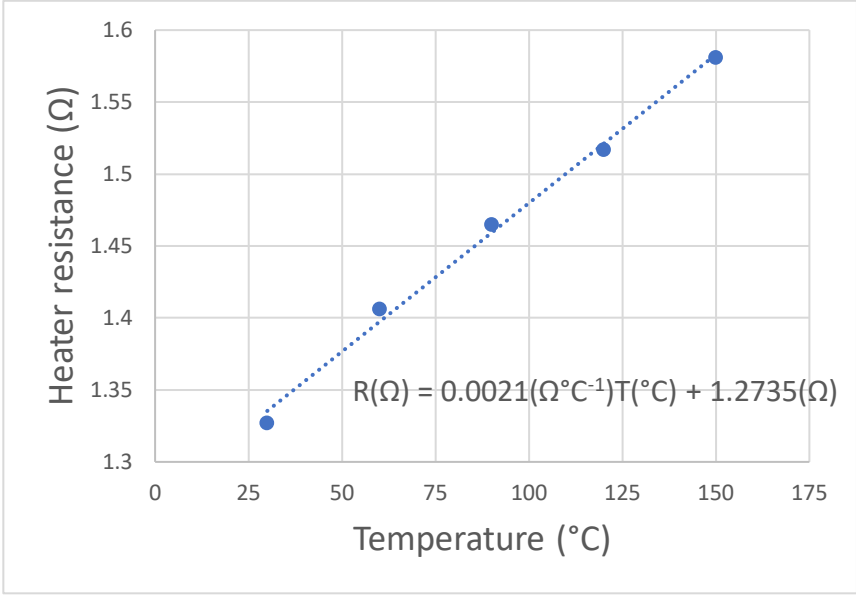


Fig. 5.3 Resistance vs temperature relationship.

Subsequently, constant voltage values were applied to the heater to increase its temperature while infrared (IR) images were taken to measure the temperature of both, heater and active layer. The IR images were taken using a FLIR T420 Thermal Imaging Camera with a resolution of 320 x 240 pixels. The measurements were carried out in ambient laboratory conditions. Three heaters were tested, and the mean values were plotted in Fig. 5.4. Due to the low resolution of the camera and the small size of the sensor, the emissivity of both,

the ZnO layer and the silver tracks could not be accurately calculated. The values of the voltage and current applied were used to estimate the temperature of the heaters using the Eq. 3-3. The temperature values obtained from the estimation correspond with the values obtained from the IR images. The obtained data allowed setting the active layer temperature according to the voltage applied to the heater.

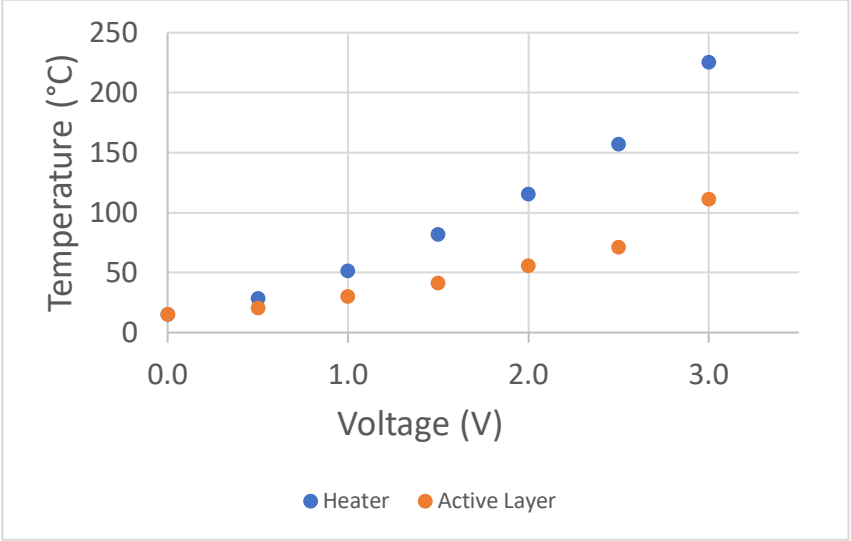


Fig. 5.4 Comparison between the mean temperature variation of the heater and the active layer as a function of the voltage applied to the heater.

The IR images revealed how the heat propagates over the entire sensor surface. It is seen that the temperature of the active layer is not homogeneous, due to the extremely low thermal conduction properties of the polymeric foil.

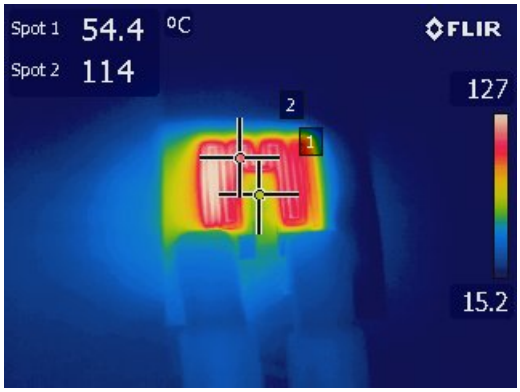


a)


b)

Fig. 5.5 IR images of one sensor when a)1.5 V and b) 3 V are applied to the heater. Spot 1 shows the active layer temperature while the spot 2 shows, the heater temperature.

The values obtained from the heater calibration were used to set up the working temperature conditions for the gas sensing test.

## Gas Sensing Test

The sensors were tested towards oxygen exposition under nitrogen ambient. The results were compared with the response of a commercial sensor (*40XV CiTiceL Oxygen ($O_2$) Gas Sensor, AAY80-390, City Technology Ltd., Portsmouth, Hampshire, U.K.*). [134] A fabricated sensor using ink A was tested, being its active layer at 100 °C according to the heater calibration done. The sensor resistance was compared with the response, percentage of oxygen

present, of the commercial sensor. In Fig. 5.6, it is possible to appreciate that the response behavior is similar for both type of sensors.

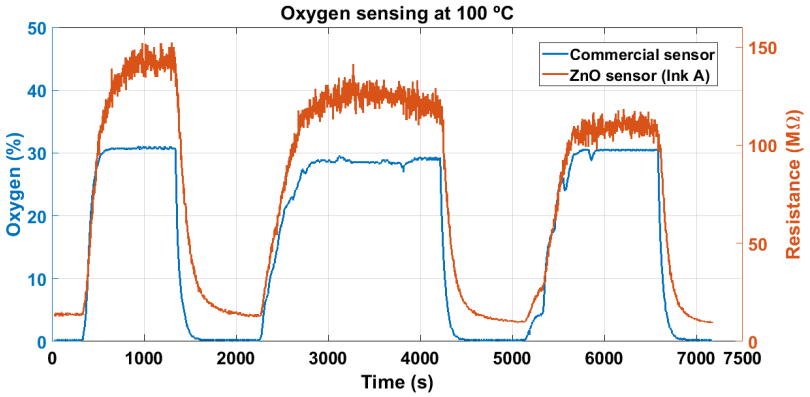


Fig. 5.6 Dynamic response of the sensor fabricated with ink A, active layer at 100 °C, compared to the response of a commercial sensor.

From the Fig. 5.7, it is possible to see there is no delay between the responses of both sensors to an oxygen pulse, but there is a difference between recovery times. The recovery times (*t10%*) of the ZnO sensor are 5 times slower compared with the recovery times of the commercial sensor. The response time was calculated as the time interval to rise the 90% of the total sensor response. The recovery time was calculated as the time interval to the total response decays to 10%.

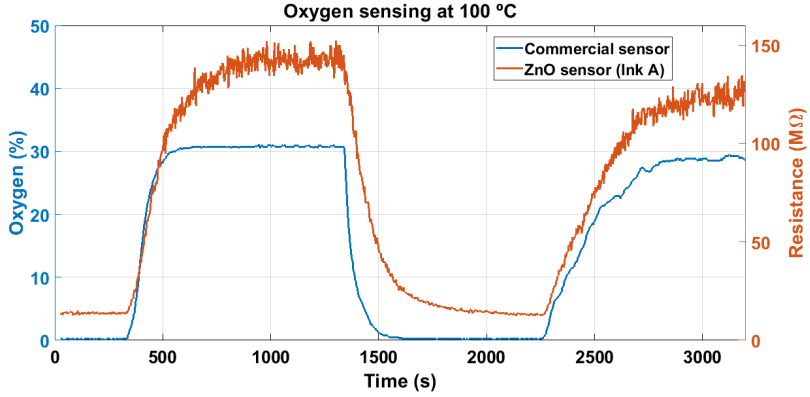


Fig. 5.7 Detail of one oxygen pulse for a ZnO sensor using the ink A (100 °C).

Sensors fabricated using ink B were tested at 50 °C and 100 °C. At 50 °C, the resistance of the sensors did not stabilize, and the sensor response was small, as Figure 5.8 illustrates. The increase of the operating temperature accelerated the adsorption and desorption rates resulting in an increase of the sensitivity. The response and recovery were faster at 100 °C than at 50 °C. At 100 °C, the response (*t90%*) and recovery times (*t10%*) are 2.5-fold slower than the corresponding times of the commercial sensor.

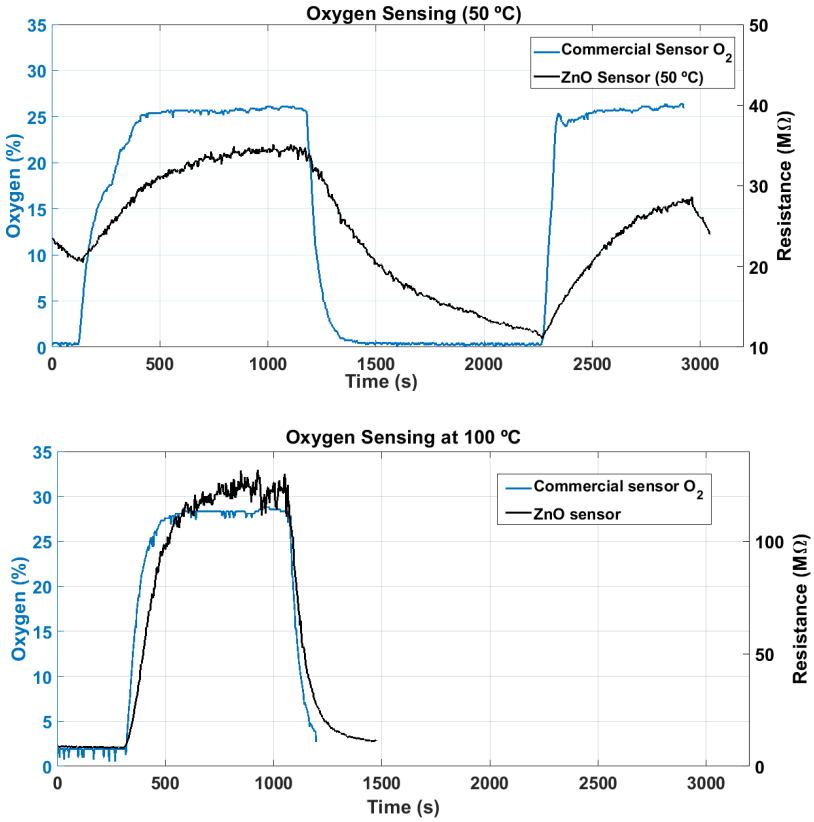


Fig. 5.8 Dynamic response of the sensor, fabricated with ink B, compared to the response of a commercial sensor. Gas sensing performed at 50 and 100 °C.

# Discussion

Both types of fabricated sensors, either using ink A or B, showed the same response behavior that the commercial sensor. The sensor using ink B showed better performance; it was faster and had higher responses. The improvement of the sensor performance can be explained by the reduction in the content of the dispersing agent. During the annealing, the coalescence of the zinc oxide nanoparticles increases the contact between them. This reduces the resistance of the layer and the response time. Additionally, the layer defects could contribute to increasing the contact surface, which improves the sensor response.

Using the screen printing technique, it is possible to obtain a flexible gas sensor with two fabrication steps. To clarify, the sensor fabrication described in this chapter needed three deposition steps due to the screen printing frame was already designed. The screen printing frame only had the IDE pattern whereby the fabrication steps were increased to deposit a heater.

Although it is indeed possible to reduce the number of deposition steps to two. The following approaches can be adopted to manufacture sensors in two-steps: use sensitive material that works at room temperature, design a screen printing frame with electrodes and a coplanar heater, or use the one electrode geometry described in chapters 3 and 4.

Furthermore, screen printing is one of the most employed techniques for printing electronic components. It allows high volume production, which makes it cost-effective and a right choice to produce flexible gas sensors. Moreover, the screen printing process can be scaled up to roll to roll process which has a higher volume production. With higher volume production techniques, the cost of the sensors diminishes and broadens the number of applications for the devices.

UNIVERSITAT ROVIRA I VIRGILI
DEVELOPMENT OF FLEXIBLE GAS SENSORS BASED ON ADDITIVE FABRICATION PROCESSES
Miriam Alvarado Pérez

# CHAPTER 6
# Conclusions and Perspectives

# Conclusions and Perspectives

## Conclusions

The aim of this thesis was to fabricate gas sensors over flexible substrates by means of printing techniques. Four different gas sensors, based on metal oxides, were designed, fabricated and characterized.

All the sensors were fabricated using a polymeric foil as a substrate (polyimide Kapton and polyimide Kapton tape). Among the flexible substrates commercially available, Kapton was preferred because it resists elevated temperatures (400 °C). Furthermore, Kapton has good chemical resistance, thermal stability, and folding endurance.

The techniques employed to obtain electrodes and heaters were: Stencil, Screen Printing, and Inkjet Printing. In most of the sensors fabricated, the electrodes and heaters were made with silver inks. Silver inks were chosen due to their commercial availability and high performance to cost ratio. The main drawback of Ag inks is silver reactivity. Silver tracks can oxidize easily. Furthermore, silver atoms tend to diffuse over the materials in which silver is in contact with, producing short-circuits or doping the adjacent material. On the other hand, gold-based inks can produce high conductive and stable tracks, but at a much higher cost.

The sensitive materials used to detect gases were: $In_2O_3$, ZnO, and $WO_3$. All of them are n-type semiconductors. Each semiconductor material employed was synthesized by a different route, which influenced the choice of its deposition technique. In the case of $In_2O_3$ and ZnO, the particles in powder, previously synthesized, were mixed with solvents and deposited. For $WO_3$, the particles were directly grown over the substrate and electrodes.

| **Sensing material** | **Conductive tracks** | | |
|---|---|---|---|
| | **Stencil** | **Screen-Printing** | **Inkjet Printing** |
| **Drop coating** | **$In_2O_3$** | | |
| **AA-CVD** | **$WO_3$** | | **$WO_3$** |
| **Screen-Printing** | | **ZnO** | |

Table 6-1 Deposition techniques employed for sensors fabrication.

The $In_2O_3$ sensors were compared with sensors of the same sensing material and geometry, but with Pt interdigitates over a rigid substrate. The fabricated sensors had the same behavior than their rigid counterparts but showed lower responses. The difference can be attributed to the interaction of the sensitive material with the electrode material. Owing to each metal-semiconductor pair presents different potential barrier as the result of the difference between their work functions, its activation energy and its conductivity changes accordingly. The $In_2O_3$ sensors demonstrated the feasibility of replacing rigid substrates with flexible ones.

The $WO_3$ sensors were obtained by direct growth of the nanowires over the flexible substrate. Two types of electrodes were used for the deposition of $WO_3$: stenciled silver electrodes, and inkjet-printed gold electrodes. A bending test proved the flexibility of the sensors. Both types of sensors were bent under controlled conditions. Gas sensing measurements were performed previously and after to the bending test. After bending, the sensor performance remained but suffered a drift.

The screen-printed ZnO sensor fabrication proved it is possible to fabricate flexible gas sensors with at least four basic steps: deposition and drying of the conductive tracks; deposition and drying of the active layer. Moreover, different sensitive materials can be deposited by previously incorporating them into a solution compatible with the screen printing process. Furthermore, it shows that it is possible to scale up the manufacturing of flexible gas sensors based on metal oxides to an industrial level.

The results demonstrate that the chosen materials, the transducer dimensions and fabrication parameters influence the performance and reliability of the flexible gas sensors. The chosen polymeric substrate showed good strength and stability throughout the manufacturing process, thus becoming a good substrate choice. Silver conductive tracks were an affordable choice to develop the transducers for the flexible sensors despite the drawbacks of silver. Silver transducers contribute to obtain lower sensor responses, but this detriment can be overcome by tailoring the electrode parameters, such as width and gap, to the target gas-sensitive material.

The performed cyclic bending tests proved that:

- The chosen materials withstand the fabrication process, which required to work on the upper limit of the substrate working temperature.
- With an adequate adjustment of the process parameters it is possible to obtain flexible sensors.
- After bending, the sensors are still functional. The sensor response showed a drift that can be adjusted.
- The transducer and the active layer had good adhesion to the substrate. This attribute is of paramount importance for the reliability of flexible sensors.

The presented results and methods could be used as a guideline to improve and extend the fabrication of flexible chemoresistive gas sensors. In general, the fabricated sensors prove the feasibility of replacing the rigid substrates for flexible ones. The substrate replacement brings a reduction in the cost of the gas sensors owing to the affordable prices of plastic substrates. Additionally, printing technologies, such as screen printing or inkjet printing, are low waste deposition methods, which helps to reduce the production cost of the sensors and thus the environmental impact.

The use of flexible substrates, such as plastic or paper, in conjunction with printing techniques makes the sensor fabrication an attainable technology. It is a simpler, more affordable technology that needs less initial investment and maintenance.

The fabrication methods followed in this thesis are simpler, more efficient, and affordable, compared with the traditional microfabrication methods, which require a series of processes to obtain a device. It proves that flexible gas sensors can be mass-produced employing printing electronics techniques. Printed electronics is a burgeoning field thanks to innovative technologies such as flexible wearable electronics and the Internet of Things. Printed electronics will allow to incorporate flexible gas sensors into a wide variety of devices.

# Future work

The market trend is to develop composite inks to lower the cost production of the electronics [135]. Composite inks incorporate metal particles, mostly silver, and conductor polymers. The interaction of the components of the ink with the sensitive materials must be studied to shed light on their stability and reliability for the implementation in chemoresistive sensor devices.

Also, graphene inks can be used for the fabrication of transducers thanks to their low-cost, ease of processability, high conductance, and flexibility. [136]. Furthermore, the electrical and mechanical properties of graphene can help to know the degree of deformation to which a flexible gas sensor is subjected, allowing to adjust the sensor responses according to the degree of deformation of the sensor.

The variety of metal oxides employed satisfactorily for sensor fabrication points out the possibility of using sensitive materials that work at room temperature and can increase the reliability of the silver conductive tracks and reduce the power consumption of the sensors.

The exploitation of low-temperature sintering methods such as photonic, laser, and intense pulsed light sintering can broaden the range of materials used for all the components of a flexible gas sensor. These sintering methods can reduce the time-consuming fabrication steps to minutes or seconds, which could involve a cost reduction. The resistivity of laser or photonic sintered metals is lower than the resistivity of thermally sintered metals. This can provide a higher printing or deposition yield of the materials. For example, less layers of metal ink would be needed to obtain conductive tracks. Moreover, sintered particles may present different morphologies that will change the sensor performance. Another advantage is that non-thermal sintering would contribute to reduce the mismatching issue of the coefficients of thermal expansion. Therefore, the effects of these sintering methods on the figures of merits of the sensor should be studied.

UNIVERSITAT ROVIRA I VIRGILI
DEVELOPMENT OF FLEXIBLE GAS SENSORS BASED ON ADDITIVE FABRICATION PROCESSES
Miriam Alvarado Pérez

# References

[1] M. Prudenziati, J. Hormadaly, 1 - Technologies for printed films, in: M. Prudenziati, Hormadaly Jacob (Eds.), Print. Film. Mater. Sci. Appl. Sensors, Electron. Photonics, Woodhead Publishing Limited, 2012: pp. 3–29. doi:10.1533/9780857096210.1.3.

[2] Printed, Organic and Flexible Electronics 2020-2030: Forecasts, Technologies, Markets: IDTechEx, (n.d.). https://www.idtechex.com/de/research-report/printed-organic-and-flexible-electronics-2020-2030-forecasts-technologies-markets/687 (accessed October 19, 2019).

[3] Printed and Flexible Sensors 2017-2027: Technologies, Players, Forecasts: IDTechEx, (n.d.). https://www.idtechex.com/de/research-report/printed-and-flexible-sensors-2017-2027-technologies-players-forecasts/504 (accessed October 19, 2019).

[4] G. Korotcenkov, Metal oxides for solid-state gas sensors: What determines our choice?, Mater. Sci. Eng. B. 139 (2007) 1–23. doi:10.1016/j.mseb.2007.01.044.

[5] P. Yu, M. Cardona, Fundamentals of Semiconductors, 4th ed., Springer-Verlag Berlin Heidelberg, 2010. doi:10.1017/CBO9781107415324.004.

[6] G. Korotcenkov, Handbook of Gas Sensor Materials Properties, Advantages and Shortcomings for Applications Volume 1: Conventional Approaches, 1st ed., Springer-Verlag New York, 2013. doi:10.1007/978-1-4614-7165-3.

[7] M.M. Arafat, B. Dinan, S.A. Akbar, A.S.M.A. Haseeb, Gas Sensors Based on One Dimensional Nanostructured Metal-Oxides: A review, Sensors. 12 (2012) 7207–7258. doi:10.3390/s120607207.

[8] C.-D. Kohl, T. Wagner, Gas Sensing Fundamentals, 1st ed., Springer-Verlag Berlin Heidelberg, 2014. doi:10.1007/978-3-642-54519-1.

[9] M.J. Toohey, Electrodes for nanodot-based gas sensors, Sensors Actuators B Chem. 105 (2005) 232–250. doi:10.1016/S0925-

4005(04)00431-9.

[10] S.P. Lee, Electrodes for Semiconductor Gas Sensors, Sensors. 17 (2017) 683. doi:10.3390/s17040683.

[11] A. Dziedzic, L.J. Golonka, B.W. Licznerski, G. Hielscher, Heaters for gas sensors from thick conductive or resistive films, Sensors Actuators B, Chem. 19 (1994) 535–539. doi:10.1016/0925-4005(93)01078-I.

[12] V. Zardetto, T.M. Brown, A. Reale, A. Di Carlo, A. Di Carlo, Substrates for Flexible Electronics: A Practical Investigation on the Electrical, Film Flexibility, Optical, Temperature, and Solvent Resistance Rroperties, J. Polym. Sci. Part B Polym. Phys. 49 (2011) 638–648. doi:10.1002/polb.22227.

[13] S. Khan, L. Lorenzelli, R.S. Dahiya, Technologies for Printing Sensors and Electronics Over Large Flexible Substrates: A Review, IEEE Sens. J. 15 (2015) 3164–3185. doi:10.119/JSEN.2014.2375203.

[14] D. Tobjörk, R. Österbacka, Paper electronics, Adv. Mater. 23 (2011) 1935–1961. doi:10.1002/adma.201004692.

[15] D. De Rossi, A logical step, Nat. Mater. 6 (2007) 328–329. doi:10.1038/nmat1892.

[16] B.E. Obi, Polymer Chemistry and Synthesis, in: Polym. Foam. Struct., William Andrew, 2017: pp. 17–40. doi:https://doi.org/10.1016/B978-1-4557-7755-6.00002-1.

[17] I. Jones, Laser welding of plastics, in: S. Katayama (Ed.), Handb. Laser Weld. Technol., Woodhead Publishing Limited, 2013: pp. 280–300. doi:10.1533/9780857098771.2.280.

[18] W.A. MacDonald, Engineered films for display technologies, J. Mater. Chem. 14 (2004) 4–10. doi:10.1039/b310846p.

[19] W.A. Macdonald, Latest advances in substrates for flexible electronics, in: M. Caironi, Y.-Y. Noh (Eds.), Large Area Flex. Electron., Wiley-VCH Verlag GmbH & Co., 2015: pp. 291–313. doi:10.1002/9783527679973.ch10.

[20] W.S. Wong, A. Salleo, Flexible Electronics: Materials and Applications, Springer US, 2009. doi:10.1007/978-0-387-74363-9.

[21] H. Ito, W. Oka, H. Goto, H. Umeda, Plastic substrates for flexible displays, Japanese J. Appl. Physics, Part 1 Regul. Pap. Short Notes Rev. Pap. 45 (2006) 4325–4329. doi:10.1143/JJAP.45.4325.

[22] S. Choopun, N. Hongsith, E. Wongat, Metal-Oxide Nanowires for Gas Sensors, in: P. Xihong (Ed.), Nanowires - Recent Adv., IntechOpen, 2012. doi:10.5772/54385.

[23] S. Sharma, M. Madou, Review article: A new approach to gas sensing with nanotechnology, Philos. Trans. R. Soc. A Math. Phys. Eng. Sci. 370 (2012) 2448–2473. doi:10.1098/rsta.2011.0506.

[24] N. Bârsan, M. Huebner, U. Weimar, 2 - Conduction mechanism in semiconducting metal oxide sensing films: impact on transduction, in: R. Jaaniso, O.K.B.T.-S.G.S. Tan (Eds.), Semicond. Gas Sensors, Woodhead Publishing Series in Electronic and Optical Materials, 2013: pp. 35–63. doi:10.1533/9780857098665.1.35.

[25] C. Xu, J. Tamaki, N. Miura, N. Yamazoe, Grain size effects on gas sensitivity of porous $SnO_2$ -based elements, Sensors Actuators B. Chem. 3 (1991) 147–155. doi:10.1016/0925-4005(91)80207-Z.

[26] N. Barsan, D. Koziej, U. Weimar, Metal oxide-based gas sensor research: How to?, Sensors Actuators, B Chem. 121 (2007) 18–35. doi:10.1016/j.snb.2006.09.047.

[27] Standards - Air Quality - Environment - European Commission, (2019). https://ec.europa.eu/environment/air/quality/standards.htm (accessed December 22, 2019).

[28] NAAQS Table | Criteria Air Pollutants | US EPA, (n.d.). https://www.epa.gov/criteria-air-pollutants/naaqs-table (accessed December 22, 2019).

[29] W. Göpel, T.A. Jones, M. Kleitz, I. Lundström, T. Seiyama, Sensors, vol. 3, Chemical and Biochemical Sensors Part II, VCH Verlagsgesellschaft mBH, 1991. doi:10.1017/CBO9781107415324.004.

[30] Emergency and Continuous Exposure Guidance Levels for Selected Submarine Contaminants, National Academies Press, 2008. doi:10.17226/12032.

[31] T. Hübert, L. Boon-Brett, G. Black, U. Banach, Hydrogen sensors - A review, Sensors Actuators, B Chem. 157 (2011) 329–352. doi:10.1016/j.snb.2011.04.070.

[32] S. Chou, J.M. Ogden, H.R. Phol, F. Scinicariello, L. Ingerman, L. Barber, M. Citra, Toxicological Profile for Hydrogen Sulfide and Carbonyl Sulfide, Agency Toxic Subst. Dis. Regist. Rep. (2016). https://www.atsdr.cdc.gov/toxprofiles/tp114.pdf.

[33] EUR-Lex - 32009L0161 - EN - EUR-Lex, (n.d.). https://eur-lex.europa.eu/legal-content/EN/TXT/?uri=CELEX:32009L0161 (accessed December 22, 2019).

[34] B. Timmer, W. Olthuis, A. Van Den Berg, Ammonia sensors and their applications - A review, Sensors Actuators, B Chem. 107 (2005) 666–677. doi:10.1016/j.snb.2004.11.054.

[35] CDC - Immediately Dangerous to Life or Health Concentrations (IDLH): Ethyl alcohol - NIOSH Publications and Products, (n.d.). https://www.cdc.gov/niosh/idlh/64175.html (accessed December 22, 2019).

[36] K. Weman, 2 - Gas welding, in: K.B.T.-W.P.H. (Second E. Weman (Ed.), Woodhead Publ. Ser. Weld. Other Join. Technol., Woodhead Publishing, 2012: pp. 13–18. doi:https://doi.org/10.1533/9780857095183.13.

[37] K.L. Choy, Chapter 12 - Vapor processing of nanostructured materials, in: H.S.B.T.-H. of N.M. and N. Nalwa (Ed.), Handb. Nanostructured Mater. Nanotechnol., Academic Press, Burlington, 2000: pp. 533–577. doi:https://doi.org/10.1016/B978-012513760-7/50015-0.

[38] J.O. Carlsson, P.M. Martin, Chemical Vapor Deposition, in: P.M. Martin (Ed.), Handb. Depos. Technol. Film. Coatings, Third Edit, Elsevier Ltd., 2010: pp. 314–363. doi:10.1016/B978-0-8155-2031-3.00007-7.

[39] E. Comini, G. Faglia, G. Sberveglieri, Electrical-Based Gas Sensing, in: E.

Comini, G. Faglia, G. Sberveglieri (Eds.), Solid State Gas Sens., Springer, Boston, MA, 2009. doi:10.1007/978-0-387-09665-0.

[40] J. Pan, G.L. Tonkay, A. Quintero, Screen printing process design of experiments for fine line printing of thick film ceramic substrates, J. Electron. Manuf. 9 (1999) 203–213. doi:10.1142/S096031319900012X.

[41] A. Blayo, B. Pineaux, Printing Processes and Their Potential for RFID Printing, in: Proc. 2005 Jt. Conf. Smart Objects Ambient Intell. Innov. Context. Serv. Usages Technol., Association for Computing Machinery, New York, NY, USA, 2005: pp. 27–30. doi:10.1145/1107548.1107559.

[42] S. Shinde, C.-Y. Jiang, C.-X. Zheng, Y.-Z. Wang, K.-M. Lin, P.M. Koinkar, Room-temperature and flexible PEDOT:PSS–WO3 gas sensor for nitrogen dioxide detection, Mod. Phys. Lett. B. 33 (2019) 6. doi:10.1142/S021798491940013X.

[43] S.J. Choi, H.J. Choi, W.T. Koo, D. Huh, H. Lee, I.D. Kim, Metal-Organic Framework-Templated PdO-Co3O4 Nanocubes Functionalized by SWCNTs: Improved NO2 Reaction Kinetics on Flexible Heating Film, ACS Appl. Mater. Interfaces. 9 (2017) 40593–40603. doi:10.1021/acsami.7b11317.

[44] U. Yaqoob, A.S.M.I. Uddin, G.S. Chung, A high-performance flexible NO2 sensor based on WO3 NPs decorated on MWCNTs and RGO hybrids on PI/PET substrates, Sensors Actuators, B Chem. 224 (2016) 738–746. doi:10.1016/j.snb.2015.10.088.

[45] U. Yaqoob, D.T. Phan, A.S.M.I. Uddin, G.S. Chung, Highly flexible room temperature NO2 sensor based on MWCNTs-WO3 nanoparticles hybrid on a PET substrate, Sensors Actuators B Chem. 221 (2015) 760–768. doi:10.1016/j.snb.2015.06.137.

[46] Z.Q. Zheng, J.D. Yao, B. Wang, G.W. Yang, Light-controlling, flexible and transparent ethanol gas sensor based on ZnO nanoparticles for wearable devices, Sci. Rep. 5 (2015) 1–8. doi:10.1038/srep11070.

[47] S.Y. Kim, J. Kim, W.H. Cheong, I.J. Lee, H. Lee, H.G. Im, H. Kong, B.S. Bae, J.U. Park, Alcohol gas sensors capable of wireless detection using

In2O3/Pt nanoparticles and Ag nanowires, Sensors Actuators, B Chem. 259 (2018) 825–832. doi:10.1016/j.snb.2017.12.139.

[48] C. Kuru, D. Choi, A. Kargar, C.H. Liu, S. Yavuz, C. Choi, S. Jin, P.R. Bandaru, High-performance flexible hydrogen sensor made of WS2 nanosheet – Pd nanoparticle composite film, Nanotechnology. 27 (2016) 7. doi:10.1088/0957-4484/27/19/195501.

[49] S. Bai, Y. Tian, M. Cui, J. Sun, Y. Tian, R. Luo, A. Chen, D. Li, Polyaniline@SnO2 heterojunction loading on flexible PET thin film for detection of NH3 at room temperature, Sensors Actuators, B Chem. 226 (2016) 540–547. doi:10.1016/j.snb.2015.12.007.

[50] J.S. Jang, Y.W. Lim, D.H. Kim, D. Lee, W.T. Koo, H. Lee, B.S. Bae, I.D. Kim, Glass-Fabric Reinforced Ag Nanowire/Siloxane Composite Heater Substrate: Sub-10 nm Metal@Metal Oxide Nanosheet for Sensitive Flexible Sensing Platform, Small. 14 (2018) 1–10. doi:10.1002/smll.201802260.

[51] P.M. Perillo, D.F. Rodriguez, Low temperature trimethylamine flexible gas sensor based on TiO2 membrane nanotubes, J. Alloys Compd. 657 (2016) 765–769. doi:10.1016/j.jallcom.2015.10.167.

[52] D.K. Kwon, Y. Porte, K.Y. Ko, H. Kim, J.M. Myoung, High-Performance Flexible ZnO Nanorod UV/Gas Dual Sensors Using Ag Nanoparticle Templates, ACS Appl. Mater. Interfaces. 10 (2018) 31505–31514. doi:10.1021/acsami.8b13046.

[53] S. Li, Y. Diao, Z. Yang, J. He, J. Wang, C. Liu, F. Liu, H. Lu, X. Yan, P. Sun, G. Lu, Enhanced room temperature gas sensor based on Au-loaded mesoporous In2O3 nanospheres@polyaniline core-shell nanohybrid assembled on flexible PET substrate for NH3 detection, Sensors Actuators, B Chem. 276 (2018) 526–533. doi:10.1016/j.snb.2018.08.120.

[54] S. Li, P. Lin, L. Zhao, C. Wang, D. Liu, F.F. Liu, P. Sun, X. Liang, F.F. Liu, X. Yan, Y. Gao, G. Lu, The room temperature gas sensor based on Polyaniline@flower-like WO 3 nanocomposites and flexible PET substrate for NH 3 detection, Sensors Actuators, B Chem. 259 (2018) 505–513. doi:10.1016/j.snb.2017.11.081.

[55] D. Yang, I. Cho, D. Kim, M.A. Lim, Z. Li, J.G. Ok, M. Lee, I. Park, SI _Gas Sensor by Direct Growth and Functionalization of Metal Oxide/Metal Sulfide Core-Shell Nanowires on Flexible Substrates, ACS Appl. Mater. Interfaces. (2019) 1–12. doi:10.1021/acsami.9b06951.

[56] S.M. Mohammad, Z. Hassan, R.A. Talib, N.M. Ahmed, M.A. Al-Azawi, N.M. Abd-Alghafour, C.W. Chin, N.H. Al-Hardan, Fabrication of a highly flexible low-cost H2 gas sensor using ZnO nanorods grown on an ultra-thin nylon substrate, J. Mater. Sci. Mater. Electron. 27 (2016) 9461–9469. doi:10.1007/s10854-016-4993-4.

[57] K. Hassan, A.S.M.I. Uddin, F. Ullah, Y.S. Kim, G.S. Chung, Platinum/palladium bimetallic ultra-thin film decorated on a one-dimensional ZnO nanorods array for use as fast response flexible hydrogen sensor, Mater. Lett. 176 (2016) 232–236. doi:10.1016/j.matlet.2016.04.138.

[58] J.L. Ramírez, F.E. Annanouch, E. Llobet, D. Briand, Architecture for the efficient manufacturing by printing of heated, planar, resistive transducers on polymeric foil for gas sensing, Sensors Actuators, B Chem. 258 (2018) 952–960. doi:10.1016/j.snb.2017.11.108.

[59] A.S.M. Iftekhar Uddin, G.S. Chung, Effects of Ag nanoparticles decorated on ZnO nanorods under visible light illumination on flexible acetylene gas sensing properties, J. Electroceramics. 40 (2018) 42–49. doi:10.1007/s10832-017-0096-8.

[60] A.S.M.I. Uddin, U. Yaqoob, D.T. Phan, G.S. Chung, A novel flexible acetylene gas sensor based on PI/PTFE-supported Ag-loaded vertical ZnO nanorods array, Sensors Actuators, B Chem. 222 (2016) 536–543. doi:10.1016/j.snb.2015.08.106.

[61] D.K. Subbiah, G.K. Mani, K.J. Babu, A. Das, J.B. Balaguru Rayappan, Nanostructured ZnO on cotton fabrics – A novel flexible gas sensor & UV filter, J. Clean. Prod. 194 (2018) 372–382. doi:10.1016/j.jclepro.2018.05.110.

[62] K. Hassan, A.S.M.I. Uddin, G.S. Chung, Mesh of ultrasmall Pd/Mg bimetallic nanowires as fast response wearable hydrogen sensors formed

on filtration membrane, Sensors Actuators, B Chem. 252 (2017) 1035–1044. doi:10.1016/j.snb.2017.06.109.

[63] Y. Kumaresan, R. Lee, N. Lim, Y. Pak, H. Kim, W. Kim, G.Y. Jung, Extremely Flexible Indium-Gallium-Zinc Oxide (IGZO) Based Electronic Devices Placed on an Ultrathin Poly(Methyl Methacrylate) (PMMA) Substrate, Adv. Electron. Mater. 4 (2018) 1–9. doi:10.1002/aelm.201800167.

[64] L. Hao, H. Liu, H. Xu, S. Dong, Y. Du, Y. Wu, H. Zeng, J. Zhu, Y. Liu, Flexible Pd-WS2/Si heterojunction sensors for highly sensitive detection of hydrogen at room temperature, Sensors Actuators B Chem. 283 (2018) 740–748. doi:10.1016/j.snb.2018.12.062.

[65] O. Krško, T. Plecenik, T. Roch, B. Grančič, L. Satrapinskyy, M. Truchlý, P. Ďurina, M. Gregor, P. Kúš, A. Plecenik, Flexible highly sensitive hydrogen gas sensor based on a TiO2 thin film on polyimide foil, Sensors Actuators, B Chem. 240 (2017) 1058–1065. doi:10.1016/j.snb.2016.09.036.

[66] J.W. Kim, Y. Porte, K.Y. Ko, H. Kim, J.M. Myoung, Micropatternable Double-Faced ZnO Nanoflowers for Flexible Gas Sensor, ACS Appl. Mater. Interfaces. 9 (2017) 32876–32886. doi:10.1021/acsami.7b09251.

[67] V. Annapureddy, Y. Kim, G.T. Hwang, H.W. Jang, S.D. Kim, J.J. Choi, B. Cho, J. Ryu, Room-Temperature Solid-State Grown WO3−δ Film on Plastic Substrate for Extremely Sensitive Flexible NO2 Gas Sensors, Adv. Mater. Interfaces. 5 (2018) 1–8. doi:10.1002/admi.201700811.

[68] X. Geng, C. Zhang, Y. Luo, M. Debliquy, Flexible NO2 gas sensors based on sheet-like hierarchical ZnO1−x coatings deposited on polypropylene papers by suspension flame spraying, J. Taiwan Inst. Chem. Eng. 75 (2017) 280–286. doi:10.1016/j.jtice.2017.03.021.

[69] M.H. Seo, S. Park, J.Y. Yoo, S. Lim, M.S. Jo, K.W. Choi, J.S. Lee, S.B. Kim, J.B. Yoon, Material-independent nanowire-transfer method based on mechanical interlocking for high performance flexible devices, Proc. IEEE Int. Conf. Micro Electro Mech. Syst. 2018-Janua (2018) 33–36. doi:10.1109/MEMSYS.2018.8346474.

[70] B. Sakthivel, L. Manjakkal, G. Nammalvar, High Performance CuO

Nanorectangles-Based Room Temperature Flexible NH3 Sensor, IEEE Sens. J. 17 (2017) 6529–6536. doi:10.1109/JSEN.2017.2749334.

[71] G. Dubourg, M. Radović, Multifunctional Screen-Printed TiO2 Nanoparticles Tuned by Laser Irradiation for a Flexible and Scalable UV Detector and Room-Temperature Ethanol Sensor, ACS Appl. Mater. Interfaces. 11 (2019) 6257–6266. doi:10.1021/acsami.8b19976.

[72] M. Rieu, M. Camara, G. Tournier, J.P. Viricelle, C. Pijolat, N.F. de Rooij, D. Briand, Fully inkjet printed SnO2 gas sensor on plastic substrate, Sensors Actuators, B Chem. 236 (2016) 1091–1097. doi:10.1016/j.snb.2016.06.042.

[73] Z. Zheng, J. Yao, B. Wang, G. Yang, A flexible, transparent and high-performance gas sensor based on layer-materials for wearable technology, Nanotechnology. 28 (2017). doi:10.1088/1361-6528/aa8317.

[74] R. George, L.A. Kumar, M. Alagappan, Synthesis of nanotubular NiO-CNT composite and its application in temperature independent CO2 gas sensors fabricated using interdigitated silver electrode, Dig. J. Nanomater. Biostructures. 14 (2019) 213–224.

[75] A. Abdelhalim, A. Falco, F. Loghin, P. Lugli, J.F. Salmeron, A. Rivadeneyra, Flexible NH3 sensor based on spray deposition and inkjet printing, in: Proc. IEEE Sensors, 2016: pp. 1–3. doi:10.1109/ICSENS.2016.7808437.

[76] S.Y. Guo, P.X. Hou, H.X. Wang, C. Shi, H.T. Fang, C. Liu, Transparent and flexible hydrogen sensor based on semiconducting single-wall carbon nanotube networks, Carbon N. Y. 151 (2019) 156–159. doi:10.1016/j.carbon.2019.05.045.

[77] Q. Zhang, C. An, S. Fan, S. Shi, R. Zhang, J. Zhang, Q. Li, D. Zhang, X. Hu, J. Liu, Flexible gas sensor based on graphene/ethyl cellulose nanocomposite with ultra-low strain response for volatile organic compounds rapid detection, Nanotechnology. 29 (2018). doi:10.1088/1361-6528/aabf2f.

[78] A. Vásquez Quintero, F. Molina-Lopez, E.C.P. Smits, E. Danesh, J. Van Den Brand, K. Persaud, A. Oprea, N. Barsan, U. Weimar, N.F. De Rooij, D. Briand, Smart RFID label with a printed multisensor platform for

environmental monitoring, Flex. Print. Electron. 1 (2016). doi:10.1088/2058-8585/1/2/025003.

[79] S. Li, S. Chen, B. Zhuo, Q. Li, W. Liu, X. Guo, Flexible ammonia sensor based on PEDOT:PSS/silver nanowire composite film for meat freshness monitoring, IEEE Electron Device Lett. 38 (2017) 975–978. doi:10.1109/LED.2017.2701879.

[80] D. Lv, W. Chen, W. Shen, M. Peng, X. Zhang, R. Wang, L. Xu, W. Xu, W. Song, R. Tan, Enhanced flexible room temperature ammonia sensor based on PEDOT: PSS thin film with FeCl3 additives prepared by inkjet printing, Sensors Actuators, B Chem. 298 (2019) 126890. doi:10.1016/j.snb.2019.126890.

[81] Q. Nie, Z. Pang, D. Li, H. Zhou, F. Huang, Y. Cai, Q. Wei, Facile fabrication of flexible SiO2/PANI nanofibers for ammonia gas sensing at room temperature, Colloids Surfaces A Physicochem. Eng. Asp. 537 (2018) 532–539. doi:10.1016/j.colsurfa.2017.10.065.

[82] 1-mil Polyimide Tape Silicone Adhesive Single-Sided | PIT1S-Series, (n.d.). https://www.caplinq.com/1-mil-polyimide-tape-silicone-adhesive-single-sided-pit1s-series.html?PTF (accessed October 22, 2019).

[83] S.Z. Karazhanov, P. Ravindran, P. Vajeeston, A. Ulyashin, T.G. Finstad, H. Fjellvåg, Phase stability, electronic structure, and optical properties of indium oxide polytypes, Phys. Rev. B - Condens. Matter Mater. Phys. 76 (2007) 1–13. doi:10.1103/PhysRevB.76.075129.

[84] O. Bierwagen, Indium oxide - A transparent, wide-band gap semiconductor for (opto)electronic applications, Semicond. Sci. Technol. 30 (2015) 24001. doi:10.1088/0268-1242/30/2/024001.

[85] N.M.A. Hadia, H.A. Mohamed, Synthesis, structure and optical properties of single-crystalline In 2O3 nanowires, J. Alloys Compd. 547 (2013) 63–67. doi:10.1016/j.jallcom.2012.08.116.

[86] S. Roso, C. Bittencourt, P. Umek, O. González, F. Güell, A. Urakawa, E. Llobet, Synthesis of single crystalline In2O3 octahedra for the selective detection of NO2 and H2 at trace levels, J. Mater. Chem. C. 4 (2016) 9418–

9427. doi:10.1039/c6tc03218d.

[87] X. Xu, H. Zhang, C. He, C. Pu, Y. Leng, G. Li, S. Hou, Y. Zhu, L. Fu, G. Lu, Synthesis and NO2 sensing properties of indium oxide nanorod clusters via a simple solvothermal route, RSC Adv. 6 (2016) 47083–47088. doi:10.1039/C6RA01958G.

[88] S. Roso, C. Bittencourt, P. Umek, O. González, F. Güell, A. Urakawa, E. Llobet, Synthesis of single crystalline In2O3 octahedra for the selective detection of NO2 and H2 at trace levels, J. Mater. Chem. C. 4 (2016) 9418–9427. doi:10.1039/c6tc03218d.

[89] J. Hu, Y. Liang, Y. Sun, Z. Zhao, M. Zhang, P. Li, W. Zhang, Y. Chen, S. Zhuiykov, Highly sensitive NO2 detection on ppb level by devices based on Pd-loaded In2O3 hierarchical microstructures, Sensors Actuators, B Chem. 252 (2017) 116–126. doi:10.1016/j.snb.2017.05.113.

[90] X. Xu, P. Zhao, D. Wang, P. Sun, L. You, Y. Sun, X. Liang, F. Liu, H. Chen, G. Lu, Preparation and gas sensing properties of hierarchical flower-like In 2O3 microspheres, Sensors Actuators, B Chem. 176 (2013) 405–412. doi:10.1016/j.snb.2012.10.091.

[91] C.S. Rout, K. Ganesh, A. Govindaraj, C.N.R. Rao, Sensors for the nitrogen oxides, NO2, NO and N2O, based on In2O3 and WO3 nanowires, Appl. Phys. A Mater. Sci. Process. 85 (2006) 241–246. doi:10.1007/s00339-006-3707-9.

[92] K.K. Pawar, J.S. Shaikh, S.S. Mali, Y.H. Navale, V.B. Patil, C.K. Hong, P.S. Patil, Hollow In2O3 microcubes for sensitive and selective detection of NO2 gas, J. Alloys Compd. 806 (2019) 726–736. doi:10.1016/j.jallcom.2019.07.248.

[93] S. Capone, P. Siciliano, F. Quaranta, R.E. Rella, L. M. Vasanelli, Moisture influence and geometry effect of Au and Pt electrodes on CO sensing response of SnO2 microsensors based on sol-gel thin film, Sensors Actuators, B Chem. 77 (2001) 503–511. doi:10.1016/S0925-4005(01)00754-7.

[94] S.M.A. Durrani, The influence of electrode metals and its configuration on

the response of tin oxide thin film CO sensor, Talanta. 68 (2006) 1732–1735. doi:10.1016/j.talanta.2005.08.015.

[95] H. Gourari, M. Lumbreras, R. Van Landschoot, J. Schoonman, Electrode nature effects on stannic oxide type layers prepared by electrostatic spray deposition, Sensors Actuators, B Chem. 58 (1999) 365–369. doi:10.1016/S0925-4005(99)00150-1.

[96] H.M. Lin, S.J. Tzeng, P.J. Hsiau, W.L. Tsai, Electrode effects on gas sensing properties of nanocrystalline zinc oxide, Nanostructured Mater. 10 (1998) 465–477. doi:10.1016/S0965-9773(98)00087-7.

[97] S. Saukko, V. Lantto, Influence of electrode material on properties of SnO2-based gas sensor, Thin Solid Films. 436 (2003) 137–140. doi:10.1016/S0040-6090(03)00509-1.

[98] A. Ylinampa, V. Lantto, S. Leppävuori, Some differences between Au and Pt electrodes in SnO2 thick-film gas sensors, Sensors Actuators B. Chem. 14 (1993) 602–604. doi:10.1016/0925-4005(93)85110-V.

[99] P. Dutronc, B. Carbonne, F. Menil, C. Lucat, Influence of the nature of the screen-printed electrode metal on the transport and detection properties of thick-film semiconductor gas sensors, Sensors Actuators B. Chem. 6 (1992) 279–284. doi:10.1016/0925-4005(92)80070-E.

[100] V.N. Mishra, R.P. Agarwal, Effect of electrode material on sensor response, Sensors Actuators B. Chem. 22 (1994) 121–125. doi:10.1016/0925-4005(94)87010-1.

[101] S.P. Lee, Electrode materials and electrode-oxide interfaces in semiconductor gas sensors, in: R. Jaaniso, O.K. Tan (Eds.), Semicond. Gas Sensors, Woodhead Publishing Limited, 2013: pp. 64–113. doi:10.1533/9780857098665.1.64.

[102] R.F. Minibaev, A.A. Bagatur'yants, D.I. Bazhanov, A.A. Knizhnik, M. V. Alfimov, First-principles investigation of the electron work function for the (001) surface of indium oxide In 2 O 3 and indium tin oxide (ITO) as a function of the surface oxidation level, Nanotechnologies Russ. 5 (2010) 185–190. doi:10.1134/S1995078010030055.

[103] C.A. Pan, T.P. Ma, Work function of In2O3 film as determined from internal photoemission, Appl. Phys. Lett. 37 (1980) 714–716. doi:10.1063/1.92055.

[104] N. Ramgir, N. Datta, M. Kaur, S. Kailasaganapathi, A.K. Debnath, D.K. Aswal, S.K. Gupta, Metal oxide nanowires for chemiresistive gas sensors: Issues, challenges and prospects, Colloids Surfaces A Physicochem. Eng. Asp. 439 (2013) 101–116. doi:10.1016/j.colsurfa.2013.02.029.

[105] E. Comini, Integration of metal oxide nanowires in flexible gas sensing devices, Sensors (Switzerland). 13 (2013) 10659–10673. doi:10.3390/s130810659.

[106] S. Vallejos, T. Stoycheva, P. Umek, C. Navio, R. Snyders, C. Bittencourt, E. Llobet, C. Blackman, S. Moniz, X. Correig, Au nanoparticle-functionalised WO3nanoneedles and their application in high sensitivity gas sensor devices, Chem. Commun. 47 (2011) 565–567. doi:10.1039/c0cc02398a.

[107] T. Stoycheva, F.E. Annanouch, I. Gràcia, E. Llobet, C. Blackman, X. Correig, S. Vallejos, Micromachined gas sensors based on tungsten oxide nanoneedles directly integrated via aerosol assisted CVD, Sensors Actuators, B Chem. 198 (2014) 210–218. doi:10.1016/j.snb.2014.03.040.

[108] N. Yamazoe, K. Shimanoe, Fundamentals of semiconductor gas sensors, in: R. Jaaniso, O. Kiang Tan (Eds.), Semicond. Gas Sensors, Woodhead Publishing Limited, 2013: pp. 3–34. doi:10.1533/9780857098665.1.3.

[109] Y.F. Sun, S.B. Liu, F.L. Meng, J.Y. Liu, Z. Jin, L.T. Kong, J.H. Liu, Metal oxide nanostructures and their gas sensing properties: A review, Sensors. 12 (2012) 2610–2631. doi:10.3390/s120302610.

[110] N. Yamazoe, G. Sakai, K. Shimanoe, Oxide semiconductor gas sensors, Catal. Surv. from Asia. 7 (2003) 63–75. doi:10.1023/A:1023436725457.

[111] F.C. Chen, T. Da Chen, B.R. Zeng, Y.W. Chung, Influence of mechanical strain on the electrical properties of flexible organic thin-film transistors, Semicond. Sci. Technol. 26 (2011). doi:10.1088/0268-1242/26/3/034005.

[112] F. Molina-Lopez, T. Kinkeldei, D. Briand, G. Tröster, N.F. De Rooij, Theoretical and experimental study of the bending influence on the

capacitance of interdigitated micro-electrodes patterned on flexible substrates, J. Appl. Phys. 114 (2013) 1–8. doi:10.1063/1.4829023.

[113] P. Lukacs, A. Pietrikova, P. Cabuk, Dependence of electrical resistivity on sintering conditions of silver layers printed by InkJet printing technology, Circuit World. 43 (2017) 80–87. doi:10.1108/CW-02-2017-0008.

[114] J. Perelaer, A.W.M. De Laat, C.E. Hendriks, U.S. Schubert, Inkjet-printed silver tracks: Low temperature curing and thermal stability investigation, J. Mater. Chem. 18 (2008) 3209–3215. doi:10.1039/b720032c.

[115] F.E. Annanouch, Z. Haddi, M. Ling, F. Di Maggio, S. Vallejos, T. Vilic, Y. Zhu, T. Shujah, P. Umek, C. Bittencourt, C. Blackman, E. Llobet, Aerosol-Assisted CVD-Grown PdO Nanoparticle-Decorated Tungsten Oxide Nanoneedles Extremely Sensitive and Selective to Hydrogen, ACS Appl. Mater. Interfaces. 8 (2016) 10413–10421. doi:10.1021/acsami.6b00773.

[116] G. Korotcenkov, One-Electrode Semiconductor Gas Sensors, in: D.K. Aswal, S.K. Gupta (Eds.), Sci. Technol. Chemiresistor Gas Sensors, Nova Science Publisher, New York, 2007: pp. 95–146. doi:10.13140/2.1.2940.9922.

[117] K.S. Siow, Are sintered silver joints ready for use as interconnect material in microelectronic packaging?, J. Electron. Mater. 43 (2014) 947–961. doi:10.1007/s11664-013-2967-3.

[118] E. Sevkat, J. Li, B. Liaw, F. Delale, A statistical model of electrical resistance of carbon fiber reinforced composites under tensile loading, Compos. Sci. Technol. 68 (2008) 2214–2219. doi:10.1016/j.compscitech.2008.04.011.

[119] S. Merilampi, T. Laine-Ma, P. Ruuskanen, The characterization of electrically conductive silver ink patterns on flexible substrates, Microelectron. Reliab. 49 (2009) 782–790. doi:10.1016/j.microrel.2009.04.004.

[120] R. Alrammouz, J. Podlecki, P. Abboud, B. Sorli, R. Habchi, A review on flexible gas sensors: From materials to devices, Sensors Actuators, A Phys. 284 (2018) 209–231. doi:10.1016/j.sna.2018.10.036.

[121] A.B. Meddeb, Z. Ounaies, M. Lanagan, Enhancement of electrical

properties of polyimide films by plasma treatment, Chem. Phys. Lett. 649 (2016) 111–114. doi:10.1016/j.cplett.2016.02.037.

[122] A. Pietrikova, P. Lukacs, D. Jakubeczyova, B. Ballokova, J. Potencki, G. Tomaszewski, J. Pekarek, K. Prikrylova, M. Fides, Surface analysis of polymeric substrates used for inkjet printing technology, Circuit World. 42 (2016) 9–16. doi:10.1108/CW-10-2015-0047.

[123] K. Keller, D. Stüwe, Inkjet Platforms for Functional Material Applications: Modular Integration of Industrial Production Processes, in: W. Zapka (Ed.), Handb. Ind. Inkjet Print. A Full Syst. Approach, First Edit, Wiley-VCH Verlag GmbH & Co., 2018: pp. 489–506. doi:10.1002/9783527687169.ch28.

[124] FUJIFILM Dimatix Materials Printer DMP-2850, (2016) 168.

[125] E. Fortunato, P. Barquinha, A. Pimentel, A. Gonçalves, A. Marques, L. Pereira, R. Martins, Recent advances in ZnO transparent thin film transistors, Thin Solid Films. 487 (2005) 205–211. doi:10.1016/j.tsf.2005.01.066.

[126] K. Nomura, H. Ohta, A. Takagi, T. Kamiya, M. Hirano, H. Hosono, Room-temperature fabrication of transparent flexible thin-film transistors using amorphous oxide semiconductors, Nature. 432 (2004) 488.

[127] Ü. Özgür, Y.I. Alivov, C. Liu, A. Teke, M.A. Reshchikov, S. Doğan, V. Avrutin, S.J. Cho, H. Morkǫ, A comprehensive review of ZnO materials and devices, J. Appl. Phys. 98 (2005) 1–103. doi:10.1063/1.1992666.

[128] D. Zhang, X. Wu, N. Han, Y. Chen, Chemical vapor deposition preparation of nanostructured ZnO particles and their gas-sensing properties, J. Nanoparticle Res. 15 (2013) 1–10. doi:10.1007/s11051-013-1580-y.

[129] C. Cano-Raya, Z.Z. Denchev, S.F. Cruz, J.C. Viana, Chemistry of solid metal-based inks and pastes for printed electronics – A review, Appl. Mater. Today. 15 (2019) 416–430. doi:10.1016/j.apmt.2019.02.012.

[130] L.W. McKeen, 14 - Renewable Resource and Biodegradable Polymers, in: L.W. McKeen (Ed.), Film Prop. Plast. Elastomers, Third Edit, William Andrew Publishing, 2012: pp. 353–378. doi:10.1016/B978-0-12-813292-

0.00014-9.

[131] J.H. Lai, An investigation of spin coating of electron resists, Polym. Eng. Sci. 19 (1979) 1117–1121. doi:10.1002/pen.760191509.

[132] A. Abbasian, S.R. Ghaffarian, N. Mohammadi, M.R. Khosroshahi, M. Fathollahi, Study on different planforms of paint's solvents and the effect of surfactants (on them), Prog. Org. Coatings. 49 (2004) 229–235. doi:10.1016/j.porgcoat.2003.09.020.

[133] J. V. Koleske, Paint and Coating Testing Manual, 15th ed., 1995. doi:10.1002/col.5080200415.

[134] Citytech, Product Datasheet 40XV Oxygen CiTiceL, 2016. www.citytech.com (accessed October 19, 2019).

[135] J. Stejskal, Conducting polymer-silver composites, Chem. Pap. 67 (2013) 814–848. doi:10.2478/s11696-012-0304-6.

[136] T.S. Tran, N.K. Dutta, N.R. Choudhury, Graphene inks for printed flexible electronics: Graphene dispersions, ink formulations, printing techniques and applications, Adv. Colloid Interface Sci. 261 (2018) 41–61. doi:10.1016/j.cis.2018.09.003.

# ANNEX I

Table 1. Flexible gas sensors fabricated using coating techniques for the deposition of the active layer.

| *Active Layer* | *Deposition Technique* | *Electrode Material and Fabrication Technique* | | *Substrate* | *Gas* | *Operating Temperature (°C)* | *Response / ppm (%)* | *Ref.* |
|---|---|---|---|---|---|---|---|---|
| PEDOT:PSS-$WO_3$ | Coating | Ag | Sputtering | PET | $NO_2$ | RT | 1.22 @ 4 ppm | [42] |
| PdO-$Co_3O_4$ functionalized by SWCNTs | Drop Coating | Cr/Au | E-Beam Evaporation | Colorless PI | $NO_2$ | 100 | 3.09 | [43] |
| $WO_3$-MWCNTs-RGO | Drop Coating | Au | Photolithography Sputtering | PI | $NO_2$ | RT (20) | 8.5 | [44] |
| MWCNTs-$WO_3$ | Gel-casting | Au | Sputtering | PET | $NO_2$ | RT | 8.5 | [45] |
| $In_2O_3$-Pt NP | Spin Coating Spray Coating | Ag NWs | Spin Coating Photolithography | PI | EtOH | RT | 9502.25 (a | [47] |
| ZnO | Casting | ITO | Laser Ablation | PET-ITO | EtOH | RT Bias voltage 8.7 V /370 nm light | 0.15 | [46] |
| $WS_2$-Pd | Coating | Ti/Au | Sputtering | PI | $H_2$ | RT | 10 @ 10 ppm | [48] |
| PANI@$SnO_2$ | Coating -Chemical Oxidation Polymerization | | | PET | $NH_3$ | RT | 212.8 @ 1.8 ppm | [49] |
| Pt-$SnO_2$ | Drop Coating | Au | E-Beam Evaporation | Glass-fabric reinforced vinyl siloxane | $C_2H_6S$ (DMS) | 160 | 348 | [50] |
| $TiO_2$ | Coating | Au | Sputtering | PI | $C_3H_9N$ (TMA) | 60 Bias voltage 2 V | 3649.44 | [51] |

a) Values calculated from the changes in the sensor current.

Table 2. Flexible gas sensors fabricated using aqueous direct growth techniques for the deposition of the active layer.

| *Active Layer* | *Deposition Technique* | *Electrode Material and Fabrication Technique* | | *Substrate* | *Gas* | *Operating Temperature (°C)* | *Response / ppm (%)* | *Ref.* |
|---|---|---|---|---|---|---|---|---|
| ZnO NRs | E-Beam Evaporation<br>Hydrothermal | Ni | Sputtering | PI | $NO_2$ | 270<br>Bias voltage 1 V | **~6100** | [52] |
| Au loaded mesoporous $In_2O_3$ | Chemical oxidation polymerization | w/o | | PET | $NH_3$ | 20 ± 2 | **300** | [53] |
| PANI flower $WO_3$ | Chemical oxidation polymerization | Au | E-Beam Evaporation | PET | $NH_3$ | RT | **150** | [54] |
| Pd-ZnO/ZnS core-shell NW | Local Hydrothermal Synthesis | Cr/Au | Photolithography<br>E-beam Evaporation<br>Lift-Off | PI | $H_2S$ | 200<br>Bias voltage 0.1 V | **103 (a** | [55] |
| ZnO NRs | Sputtering<br>Hydrothermal | Pt | Sputtering | Thermo nylon | $H_2$ | 180 | **~10 (b** | [56] |
| Pt/Pd-ZnO NRs | Hydrothermal<br>Pulse Laser Deposition | Au | Sputtering | PI/PET | $H_2$ | 100 | **~28** | [57] |
| $WO_3$-Pt | AA-CVD | Au | Inkjet-printing | PI | $H_2$ | 220 | **~500 @ 40 ppm (b** | [58] |

| | | | | | | | | |
|---|---|---|---|---|---|---|---|---|
| Ag-ZnO NRs | Sputtering<br>Hydrothermal<br>Sputtering | Au | Sputtering | PI/PET | Acetylene ($C_2H_2$) | 120<br>Bias voltage 1 V<br>530 nm light | **~150** | [59] |
| Ag-ZnO | Sputtering<br>Hydrothermal<br>Sputtering | Au | Sputtering | PI/PTFE | Acetylene ($C_2H_2$) | 200 | **~100** | [60] |
| ZnO | Sol-Gel<br>Sputtering | | | Cotton fabric | Acetaldehyde | RT (27) | **3200 @ 100 ppm** | [61] |

a) Calculated using the sensor conductance changes.
b) Calculated using the sensor current changes.

Table 3. Flexible gas sensors fabricated by direct deposition of the sensitive material.

| *Active Layer* | *Deposition Technique* | *Electrode Material and Fabrication Technique* | | *Substrate* | *Gas* | *Operating Temperature (°C)* | *Response / ppm(%)* | *Ref* |
|---|---|---|---|---|---|---|---|---|
| Pd/Mg NW mesh | Sputtering | Au | Sputtering | Anodisc membrane | $H_2$ | RT<br>Bias voltage 1 V | **~0.7 @ 10 ppm** | [62] |
| IGZO-Pd | Sputtering | Au/Ti | E-beam evaporation | PMMA | $H_2$ | RT | **2.3 x $10^6$ @ 50 000 ppm** | [63] |
| $WS_2$ | Sputtering | Al | Sputtering | Si (10 µm) | $H_2$ | RT | **~70** | [64] |
| $TiO_2$ | Sputtering | Pt | Sputtering<br>Photolithography | PI | $H_2$ | RT (24) | **9900 @ 300 ppm** | [65] |
| ZnO NFs | Transfer<br>Aqueous solution | SWCNTs | Spray Coating | PI | $NO_2$ | 270<br>Bias voltage 1 V | **~740** | [66] |
| $WO_{3-\lambda}$ | Granule Spray in vacuum | Au/Cr | Sputtering | PI | $NO_2$ | RT | **~4005 @ 2.25 ppm** | [67] |
| ZnO | Flame Torch | Au | Screen-Printing | Polypropylene paper | $NO_2$ | RT<br>0.15 W/cm2 light | **260** | [68] |
| $Cu_2O$ | Transfer Printing | Au | Conventional MEMS process | Polyurethane acrylate (PUA) | $NO_2$ | 110 | **Not clearly stated** | [69] |

Table 4. Flexible gas sensors fabricated using printing techniques for the obtention of the active layer.

| ***Active Layer*** | ***Deposition Technique*** | ***Electrode Material and Fabrication Technique*** | | ***Substrate*** | ***Gas*** | ***Operating Temperature (°C)*** | ***Response / ppm (%)*** | ***Ref*** |
|---|---|---|---|---|---|---|---|---|
| CuO | Screen Printing | Ag | Screen Printing | PET | $NH_3$ | 27<br>Bias voltage 3V | **18 @ 5 ppm** | [70] |
| $TiO_2$ | Screen Printing | Ag | Screen Printing | PET | EtOH | 25 | **~ 4700 @ 100 ppm** | [71] |
| $SnO_2$ | Inkjet printing | Au | Inkjet printing | PI | $NO_2$ | 200 | **~ 4200** | [72] |

# ANNEX II

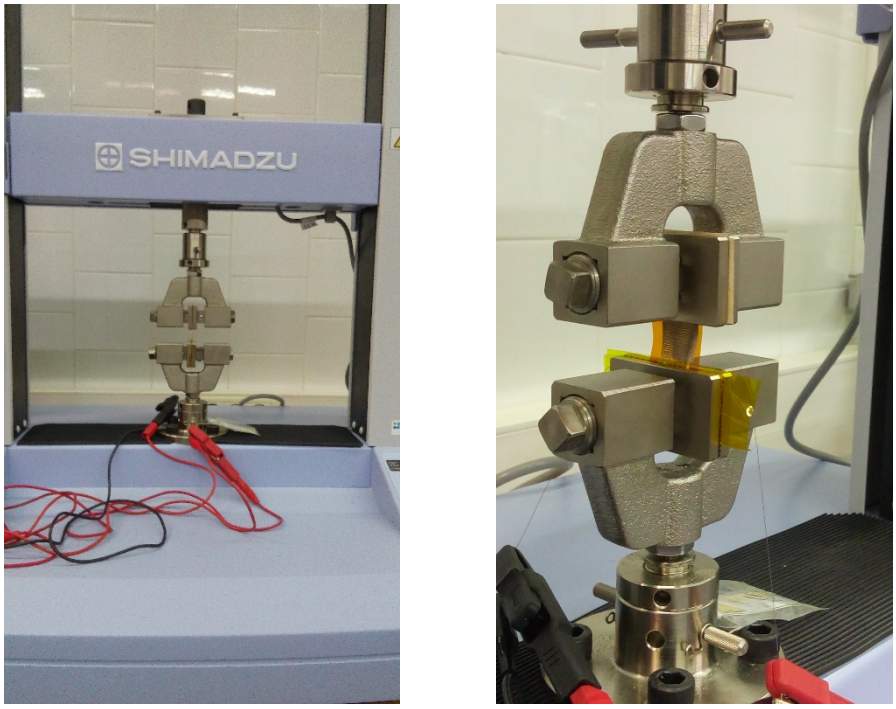


a) b)

*Digital image of a) the Universal Testing Machine for the bending test and b) a close up of the grips holding a sensor.*

# Publications in International Journals

- "Flexible Gas Sensors Employing Octahedral Indium Oxide Films"

  Miriam Alvarado, Éric Navarrete, Alfonso Romero, José Luis Ramírez and Eduard Llobet.

  Sensors **2018**, 18(4), 999

- "Performance of Flexible Chemoresistive Gas Sensors after Having Undergone Automated Bending Test"

  Miriam Alvarado, Silvia De La Flor, Eduard Llobet, Alfonso Romero and José Luis Ramírez.

  Sensors **2019**, 19(23), 5190

# Contributions in Conferences and Seminars

- **8ème Franco-Spanish Workshop IBERNAM-CMC2 (13-14 October 2016), Toulouse, France.**
  - Poster presentation: *"Fast Low-Cost Transducer Prototyping Technique".*

    M. Alvarado, J.L. Ramírez, A.J. Romero

- **IEEE SENSORS 2017 (29 Oct-1 Nov 2017), Glasgow, UK.**
  - Poster presentation: *"Comparing performance of flexible and rigid substrates for $In_2O_3$ based gas sensors".*

    Miriam Alvarado, E. Navarrete, E. Llobet, J.L. Ramírez and A. Romero

- **IEEE SENSORS 2018 (28-31 Oct 2018), New Delhi, India.**
  - Oral Contribution: *"Single-Crystalline Metal Oxide, Resistive Gas Sensors Advances and Perspectives".*

    E. Llobet, E. Navarrete, F.E. Annanouch, M. Alvarado, E. Gonzalez, J.L. Ramírez, A. Romero, X. Vilanova, M. Domínguez-Pumar, S. Vallejos, I. Grácia.

- **8th GOSPEL Workshop. Gas Sensors Based on Semiconducting Metal Oxides: Basic Understanding & Applications Fields, 2019, 20-21 June, Ferrara, Italy**
  - Oral Contribution: *"Testing the Reliability of Flexible MOX Gas Sensors under Strain".*

    M. Alvarado, A. Romero, J.L. Ramírez, S. De La Flor and E. Llobet.